



저작자표시-비영리-변경금지 2.0 대한민국

이용자는 아래의 조건을 따르는 경우에 한하여 자유롭게

- 이 저작물을 복제, 배포, 전송, 전시, 공연 및 방송할 수 있습니다.

다음과 같은 조건을 따라야 합니다:



저작자표시. 귀하는 원저작자를 표시하여야 합니다.



비영리. 귀하는 이 저작물을 영리 목적으로 이용할 수 없습니다.



변경금지. 귀하는 이 저작물을 개작, 변형 또는 가공할 수 없습니다.

- 귀하는, 이 저작물의 재이용이나 배포의 경우, 이 저작물에 적용된 이용허락조건을 명확하게 나타내어야 합니다.
- 저작권자로부터 별도의 허가를 받으면 이러한 조건들은 적용되지 않습니다.

저작권법에 따른 이용자의 권리는 위의 내용에 의하여 영향을 받지 않습니다.

이것은 [이용허락규약\(Legal Code\)](#)을 이해하기 쉽게 요약한 것입니다.

[Disclaimer](#)

Abstract

Bio-inspired design and fabrication for high sensitive recognition system

Daeshik Kang
School of Mechanical and Aerospace Engineering
The Graduate School
Seoul National University

In this thesis, we describe the high sensitive recognition systems motivated by several sensory organ in the nature. Firstly we present a high sensitive micro lens system, which can resolve about 150 nm, from the light focusing principle of brittle-star's micro bump and Secondly we present a high sensitive crack sensor, which can detect about 10 nm vibration, from spider's slit organ. Especially this spider-inspired crack sensor shows over 2000 gauge factor (GF) under 2 % strain area that is world record level so far. Further, based on this result, we develop , we developed a highly sensitive, flexible, and multiplex strain gauge sensor demonstrate several precise mechanical and medical engineering applications like an anti-noise speech recognition system, heart beat diagnosis system etc.

Key Words : Bio-inspire, Microlens Array, Micro Contact Printing, Diffraction Limit, Slit Organ, Strain Gauge, Nano Crack, Speech Recognition

Student Number: 2009-20647

Table of Contents

Chapter 1. Introduction	1
Chapter 2. Brittlestar-inspired Microlens Array	
2-1. Objective	4
2-2. Direct transfer method for micro-scale lens array	6
2-3. Shape controllability of the microlens array	12
2-4. Transferring on arbitrary surfaces	16
2-5. Overcoming the diffraction limit	21
2-6. Summary	32
Chapter 3. Spider-inspired Nanoscale Crack Sensor	
3-1. Objective	34
3-2. Fabrication method of nanoscale crack sensor	37
3-3. Results and theoretical analysis	46
3-4. Multi-pixel array of the crack sensor	59
3-5. Versatile applications of the crack sensor	68
3-6. Summary	84
References	119

국문초록
감사의 글

Chapter 1. Introduction

Nature has remarkably versatile and sensitive sensory systems. For photosynthesis, many plant organs contain photo-sensitive compounds, such as phototropins, cryptochromes and phytochromes, each of which reacts to light within a very specific range of wavelength. And for survival, many insects have mechano-sensitive organs (antennae, lyriform slit organ, hair sensilla) detecting very light touch. Some of these sensory organs show ultra-high sensitive and surprising performance beyond artificial sensors. So many sensor technologists are looking to nature for inspiration, and recently the significant technical advances in nanotechnology have made it possible to develop sensors which mimic many of the functions or structures found in nature. However, there still remain many unresolved problems, for example, the diffraction limit (which means a fundamental maximum resolution of an optical system, set by diffraction) and the cock-tail party problem (which means the phenomenon of being able to focus one's auditory attention on a particular stimulus while filtering out a range of other stimuli, much the same way that a partygoer can focus on a single conversation in a noisy room). To solve these problems, firstly, we found certain organ overcoming these phenomena in nature and studied the principle more deeply. Secondly, we developed the bio-inspired sensory systems by using several nano-fabrication methods and materials. As fabrication methods, we used 'micro contact printing', 'partially curing method', 'spin coating', and 'nano sphere lithography'. And we used UV-curable polymer (PUA, PEG, NOA etc.) and heat-curable polymer (PDMS)

as materials.

In Chapter 2, we report a simple method for fabricating a shape-controllable lens array by directly transferring photo-curable polymer droplets onto a target substrate. By transferring various sizes of lenses (diameter: 481 nm – 15.5 μm) on solid substrates, the ability to tailor the final shape of the transferred lens array was confirmed. We found that the shrinkage was negligible during the photo-curing step. Also, the PUA or PEG lenses with different convex configurations (contact angle: 9.8° – 90.9°) were transferred onto various substrates having different curvature, step, or topography. Nanoscale features as small as 130nm gap distance was visualized under an optical microscopy using the 3- μm diameter lens array with the CA of 90.9° .

In *chapter 3*, we mimicked the highly sensitive and complicated slit organ of a spider's strain detector to design a novel, simplified, and ultra-mechanosensitive nanoscale crack-based sensor. We demonstrated that our spider-inspired sensor exhibits the highest gauge factor of a sensor achieved to date and can be applied as a multifunctional sensor for highly selective speech pattern recognition, human physiology monitoring and external force and vibration detection. We studied the underlying physical mechanism and observed the intriguing disconnection/reconnection processes of the crack junctions, which enabled the

ultra-high sensitivity of the device. We developed a theory describing electrical conductance through crack junctions when strain is applied, which is consistent with the experiments. Moreover, the reproducibility, flexibility and large area coverage with multiplexing permit the integration of the device on curvilinear human skin with more advanced tools.

Chapter 2. Brittlestar-inspired Microlens Array

2-1. Objective

Optical lens [1-6] cannot resolve features smaller than ca. half of a wavelength due to the Abbe diffraction limit [7]. Several efforts to this date have been pursued to overcome diffraction limit using various approaches including lensing effects driven by surface-plasmon excitation [8-11] and fluorescence microscopy with molecular excitation [12,13]. However, the widespread use of these methods has been limited in part due to complex fabrication or pretreatment steps. Alternatively, it has been recently demonstrated that a spherical micro-lens shows remarkable short focal length, leading to sub-diffraction limit optical imaging property without complex fabrication or additional process. [14-18] In these works, a thin individual sub-micrometer lens formed by chemical growth [14,15] or reflow [16,17] or a spherical polymer bead [18] was placed on a target substrate, thereby resolving features beyond the diffraction limit. These microscale lens magnification systems enable facile approaches to high-resolution optical imaging at very low intensities as well as new applications to bio-imaging, near-field lithography, optical memory storage, light harvesting, and optical nano-sensing. [14]

Although microlens demonstrated potential for overcoming the diffraction limit, current fabrication methods for the microscale lens have several shortcomings, in that the preparation process is relatively complex due to multiple steps, and there is a lack of controllability over the shape and array formation of lens. Furthermore, transferring and positioning of microlens on a specific target had been challenging. Even though conventional inkjet printing method is widely used for forming an array of liquid droplets, which could be a form of liquid lens, it is impossible to make micro- to nanoscale lens due to evaporation. [19] Herein, we report a new strategy to produce an array of microlens with various dimensions (diameter: 481 nm – 15.5 μ m) and configurations (contact angle: 9.8° – 90.9°) using an optically transparent UV-curable polymer. Specifically, we formed the microlens array directly by transferring polymer droplets to a target substrate via the modulation of surface energy. By using our transferring method, nanoscale gaps as small as 130 nm were resolved under an optical microscope, demonstrating imaging resolution beyond the diffraction limit.

2-2. Direct transfer method for micro-scale lens array

A schematic diagram for the fabrication of shape-controllable microlens arrays is shown in Figure 2-1(a). The fabrication was performed with three consecutive steps: i) an elastomeric polydimethyl siloxane (PDMS) mold with protruding pillars was inked by a viscous thin polymer layer (step 1 in Figure 2-1(a)), ii) the inked droplets on pillars were transferred onto a target substrate with a slight pressure (~ 10 Pa) (step 2, 3 in Figure 2-1(a)), and iii) the transferred droplets were left undisturbed to reach an equilibrium shape as time passes by (step 4 in Figure 2-1(a)). Finally, after reaching an equilibrium shape the transferred droplets were solidified via UV exposure.

In the first step, we need to control the amount of pre-polymer in such a way that the entire pillars are not wetted by the pre-polymer, but only the protruding pillar heads are wetted. In order to transfer a small amount of pre-polymer to the pillar heads, a thin UV-curable polyurethane acrylate (PUA) film (thickness: $20\ \mu\text{m}$) was crosslinked in the presence of ambient oxygen. It is known to oxygen inhibits free radical polymerization by reacting with initiator radicals, resulting in the formation of a thin partially-cured viscous layer on top of the fully cured layer. [20-25] The thickness of such a partially cured layer can be controlled by adjusting UV curing time and intensity, typically ranging from $1 \sim 5\ \mu\text{m}$.

Next, a patterned PDMS mold with pillars sticking out was brought in

conformal contact with the partially cured layer, and gently separated after a period of time (5 sec), leaving behind a portion of viscous layer on top of the pillars. This transfer step was confirmed by Scanning Electron Microscope (SEM) measurements before and after the contact, as shown in Figure 2-1(b). Here, the white dotted line indicates a polymer droplet transferred to the pillar tip. Subsequently, the PDMS mold was directly in contact with a target substrate (i.e. Teflon-coated silicon, PDMS, or glass) and carefully detached. Then, a certain portion of the droplet ($\approx 13\%$ on Teflon coated silicon, $\approx 50\%$ on PDMS) was transferred to the target substrate due to breakup at the liquid-liquid interface. [26,27] Once transferred, the droplet was retracted slowly to reach the equilibrium contact angle (Figure 2-1(c), Figure 2-5(a)); The PUA droplet on the PDMS substrate was stabilized at equilibrium diameter (d_E) approximately within 5 hrs and unchanged thereafter (Figure 2-5(a)). Interestingly, on the Teflon-coated silicon substrate, the PUA droplet was stabilized within 10 min. After the transfer, the array of polymer microlens was fully cured in an UV chamber and metallic nanoscale features were observed under an optical microscope (Figure 2-1(d)).

It should be noted that the droplet shape was almost unchanged after the curing since the bulk shrinkage of PUA is as small as 0.7%. [28] To verify this, side-view SEM images of the PUA lens were compared at the equilibrium and cured conditions, respectively (Figure 2-5(b)). As shown, the ratio of the final lens height to diameter ($h_F/d_F = 0.271$) was nearly the same with the equilibrium ratio (h_E/d_E

= 0.28). Furthermore, the resulting polymer droplet showed a perfectly smooth plano-convex lens due to its high surface tension (~ 25 dyne/cm), [29] as determined by the three-dimensional Atomic Force Microscope (AFM) image of the transferred PUA lens array (Figure 2-6). As can be seen in the figure, the lens curvature was almost overlapped with the perfect sphere, suggesting that the surface be smooth and uniformly curved.

PDMS molds were prepared by replica molding from silicon masters prepared by photolithography. A mixture of base and curing agent (10:1 w/w) of Sylgard 184 PDMS elastomer was poured onto the patterned masters and cured at 70°C for 2 h. The cured PDMS molds were peeled off from the masters and cut prior to use. Three types of PDMS molds were used: i) $d = 24\ \mu\text{m}$, $h = 4\ \mu\text{m}$, ii) $d = 8\ \mu\text{m}$, $h = 4\ \mu\text{m}$, and iii) $d = 800\ \text{nm}$, $h = 300\ \text{nm}$. A small amount of droplets ($100 \sim 200\ \mu\text{l}$) of three different UV-curable prepolymers such as PUA (PUA MINS 311 RM purchased from the Minuta Tech, South Korea), NOA (NOA 65 purchased from iNexus inc. 4science, South Korea), PEG (PEG-DA Mw 550 purchased from Sigma-Aldrich, USA) was dispensed onto a flexible PET film ($50\ \mu\text{m}$), which was used as a supporting backplane. Then, the droplets were covered with a thin PDMS blanket ($\sim 2\ \text{mm}$) under a slightly pressure ($\sim 10\ \text{Pa}$). The thickness of the UV-curable polymer was approximately $20\ \mu\text{m}$. The samples were exposed by UV light for a short period of time, i.e., 20 sec for PUA, 0.5 sec NOA, and 60 sec PEG, respectively, since an over-curing led to a failure of the subsequent microlens

transfer. A PDMS mold with protruding pillars was carefully brought in contact under a slight pressure (~ 10 Pa), remained undisturbed for 5 sec, and removed, leaving behind a fraction of the partially-cured layer on top of the pillars. The layer was subsequently transferred to various substrates such as Teflon-coated silicon, PDMS, glass, lenticular lens, and cicada wing.

Magnified optical images through an array of microlens were seen using an optical microscope (Olympus IX70, Japan). SEM images were taken using FESEM (Hitachi S-48000, Japan) with a Pt coating of 5 nm to prevent electron charging. Static contact angles of polymer droplets were measured by a contact angle analyzer (KRUSS DSA 100, Germany).

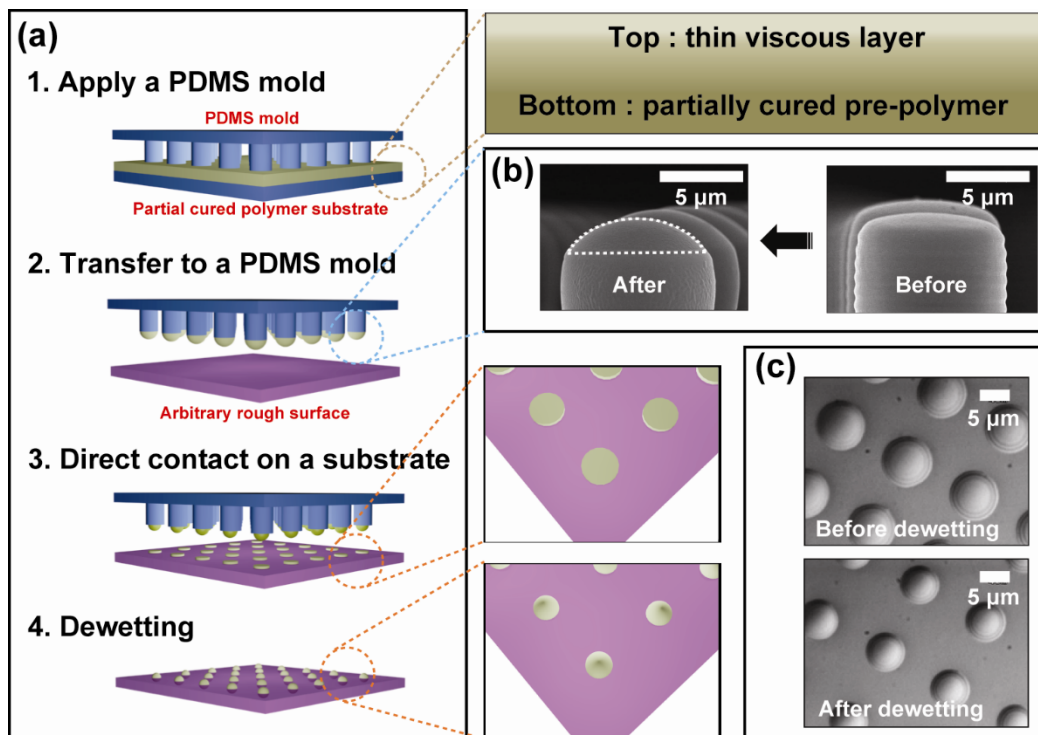


Figure 2-1. (a) Schematic diagram for the fabrication of shape-controllable polymer microlens array. (b) SEM images of PDMS pillar before and after the contact. Here, the white dotted line shows a transferred PUA droplet to the top of the PDMS pillar. (c) Optical images of the polymer droplet on PDMS substrate immediately after the contact and after reaching the equilibrium shape.

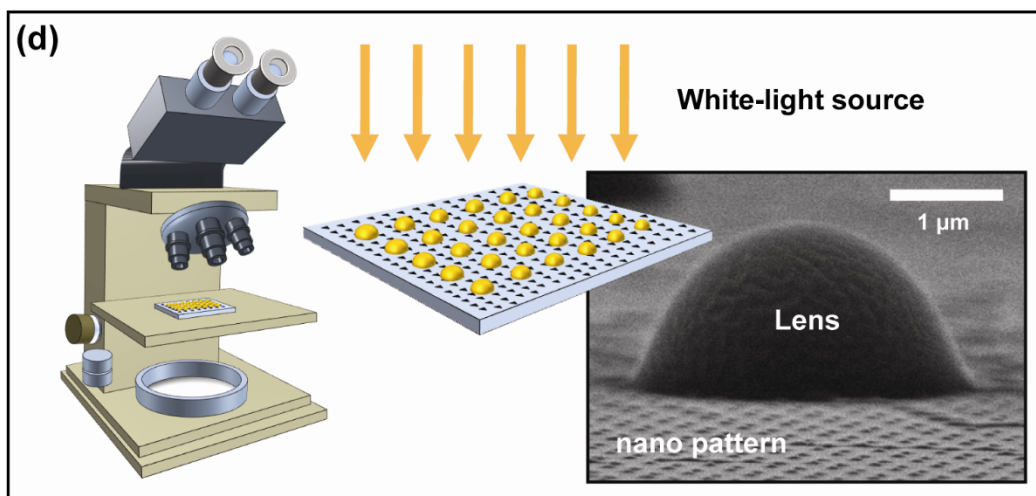


Figure 2-1. (d) Schematic for the visualization using the transferred microlens array. Inset: SEM image of PEG microlens on a silver nanopattern. The wrinkles are formed by a Pt layer deposited for SEM measurement.

2-3. Shape controllability of the microlens array

To investigate the capability of controlling the size of microlens, we used PUA as a photo-curable polymer and a PDMS mold with pillars of three different diameters (d) (Figure 2-2 (a)): $d = 24 \mu\text{m}$, $8 \mu\text{m}$, and 800 nm . As shown, the degree of retraction (dewetting) after reaching the equilibrium shape was similar among the three different PUA droplets. For example, when we define α as the ratio of the final lens diameter to mold diameter, ($\alpha = dF/d$), we get $\alpha = 64$, 62 , and 63% for $d = 24 \mu\text{m}$, $8 \mu\text{m}$, and 800 nm , respectively. Furthermore, the aspect ratio of each microlens after photocrosslinking-induced shrinkage was similar among the three different PUA droplets regardless of their size, as measured by SEM and AFM in Figure 2-2(b): (i) $hF/dF = 0.276$ ($dF = 15.54 \mu\text{m}$, $hF = 4.30 \mu\text{m}$), (ii) $hF/dF = 0.273$ ($dF = 4.98 \mu\text{m}$, $hF = 1.36 \mu\text{m}$), (iii) $hF/dF = 0.281$ ($dF = 481 \text{ nm}$, $hF = 135 \text{ nm}$). We discovered that the transferred plano-convex PUA lens is fixed to the surface and undergoes slight volume shrinkage (0.7%) in the course of photocrosslinking. Moreover, the size variation within a single array was less than 2% for all the microlens arrays mentioned above. These results strongly indicate shape-controllability of the current method in determining the final shape of the transferred microlens array.

Next, we tested the tunability of the contact angle of the lens. Figure 2-2(c) shows measurements of static contact angles (CAs) of three UV-curable polymers

(PUA, PEG, NOA) on hydrophilic glass and hydrophobic Teflon substrates. As shown, the CAs range from 9.8° (PUA on glass) to 90.9° (PEG on Teflon) depending on the polymer's affinity to the substrate. Such a tunable three-dimensional convex configuration has significant effects on the remarkable short focal length, such that a higher CA gives rise to a higher focusing effect as described shortly.

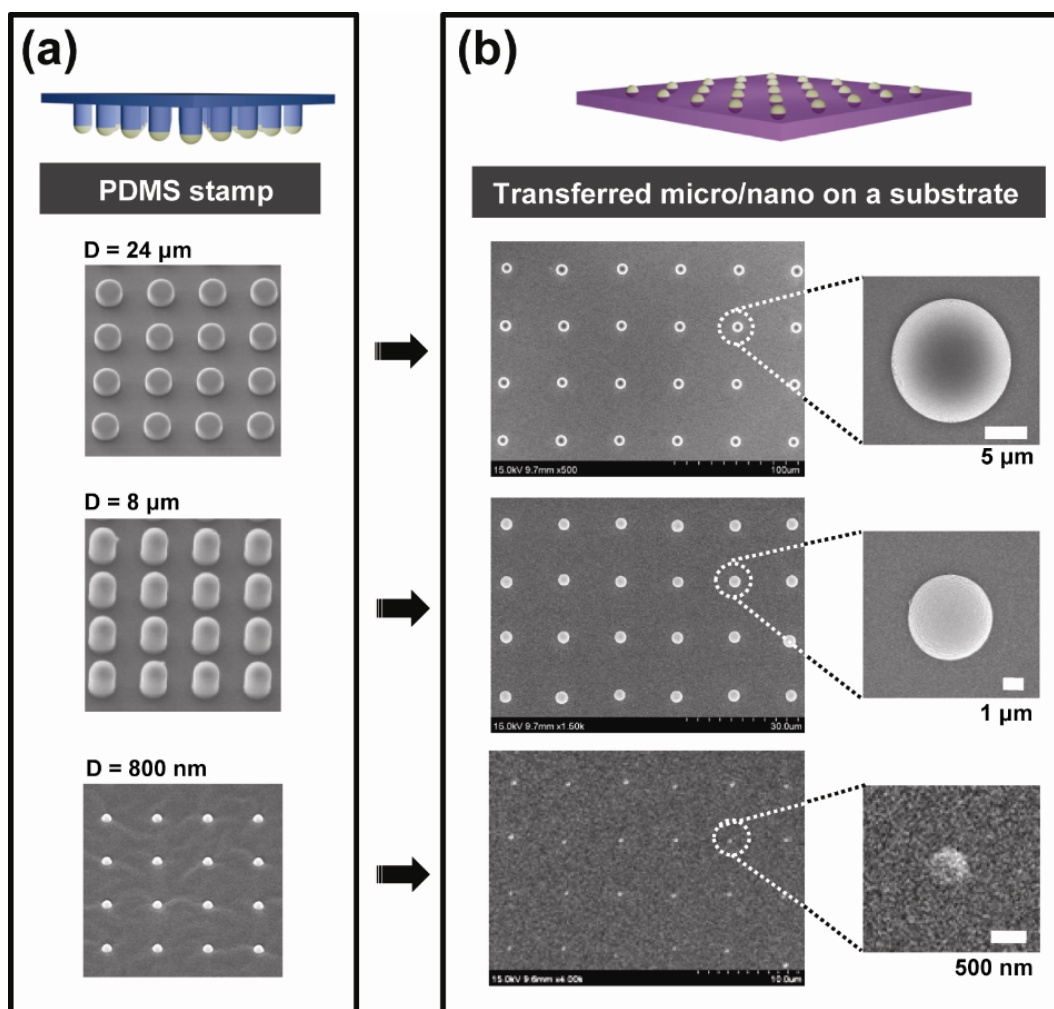


Figure 2-2. (a) SEM images showing various dimensions of PDMS pillars. (b) SEM images of the corresponding PUA droplets transferred to the PDMS substrate. As shown, the degree of shrinking was similar for the three different PUA droplets: $\alpha = 64$, 62 , and 63% for $d = 24 \mu\text{m}$, $8 \mu\text{m}$, and 800 nm , respectively ($\alpha = \text{lens diameter} / \text{mold diameter}$).

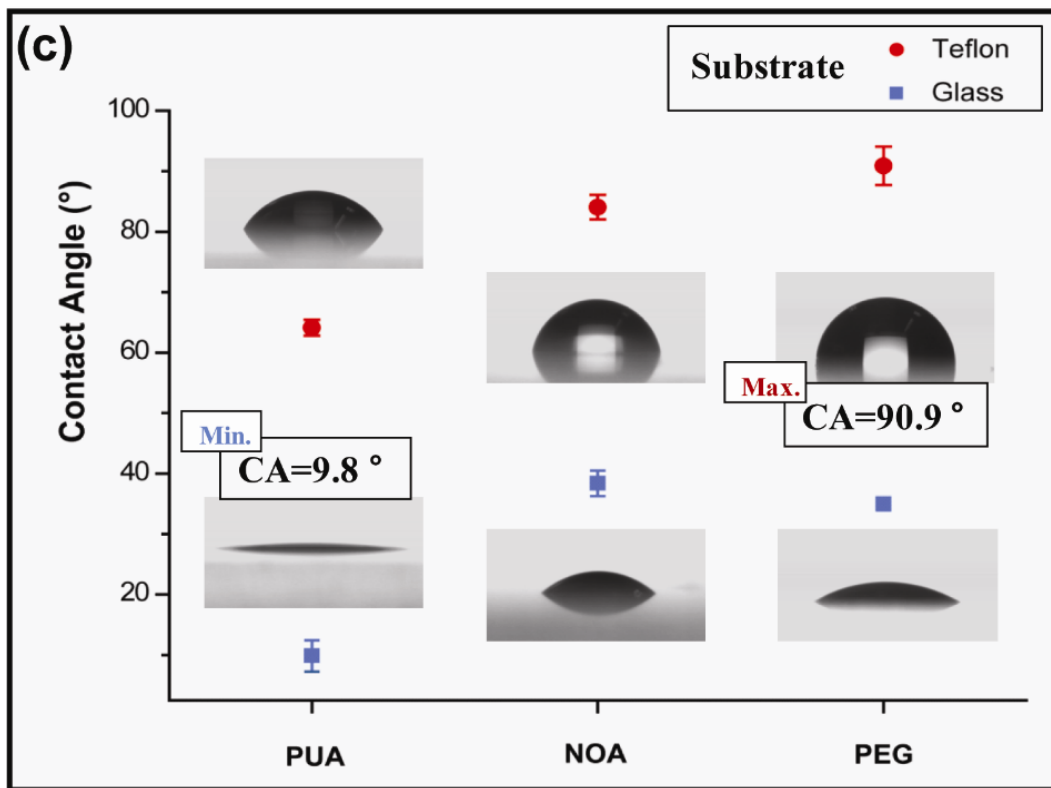


Figure 2-2. (c) Static CAs of three UV-curable polymers (PUA, NOA, PEG) on hydrophilic glass and hydrophobic Teflon-coated substrates.

2-4. Transferring on arbitrary surfaces

In addition to the controllability of the lens shape, our method exhibits another advantage to form an array of microlens on various solid substrates. Figure 2-3 shows the array of transferred microlens on (a) flat, (b) curved (lenticular lens, period of 630 μm), and (c) stepped (pattern height of 2 μm) substrates as well as on (d) a cicada wing where a dense micropillar array is seen from the underlying surface. Here, all the substrates were Teflon-coated to increase CAs. This transfer capability is attributed to high compliance of the PDMS mold so that individual pillars can make intimate contact with a topographically patterned surface even in the presence of moderate roughness.

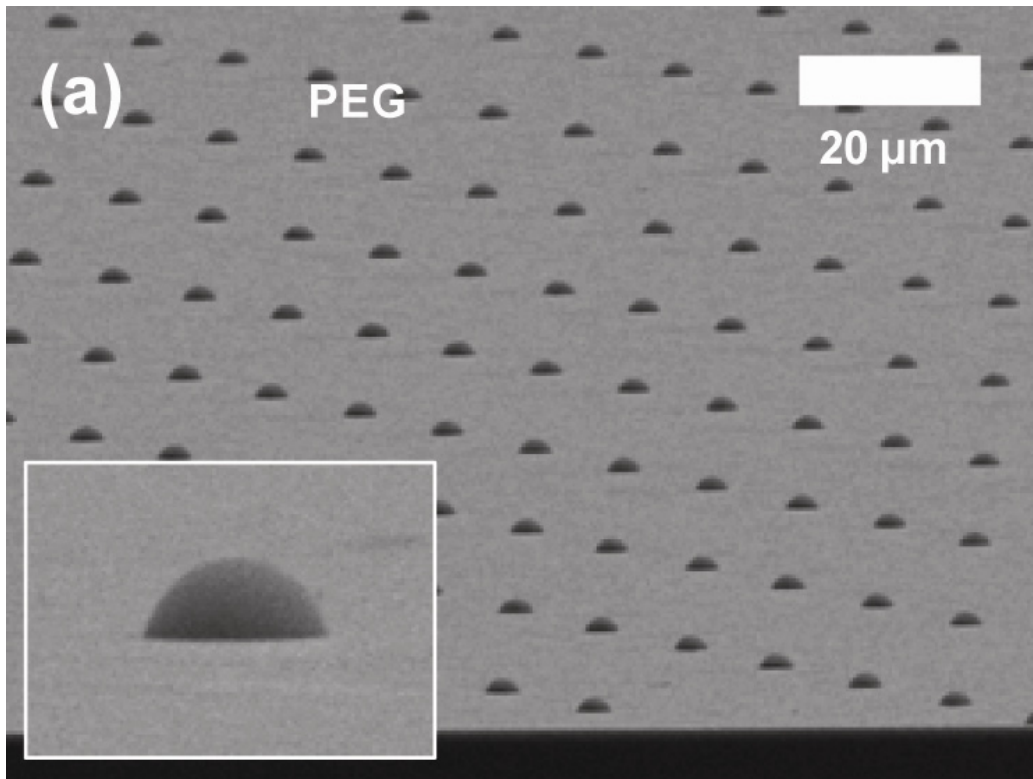


Figure 2-3. Transferring ability of plano-convex lenses on a range of substrates.

(a) PEG lens array on Teflon-coated silicon wafer.

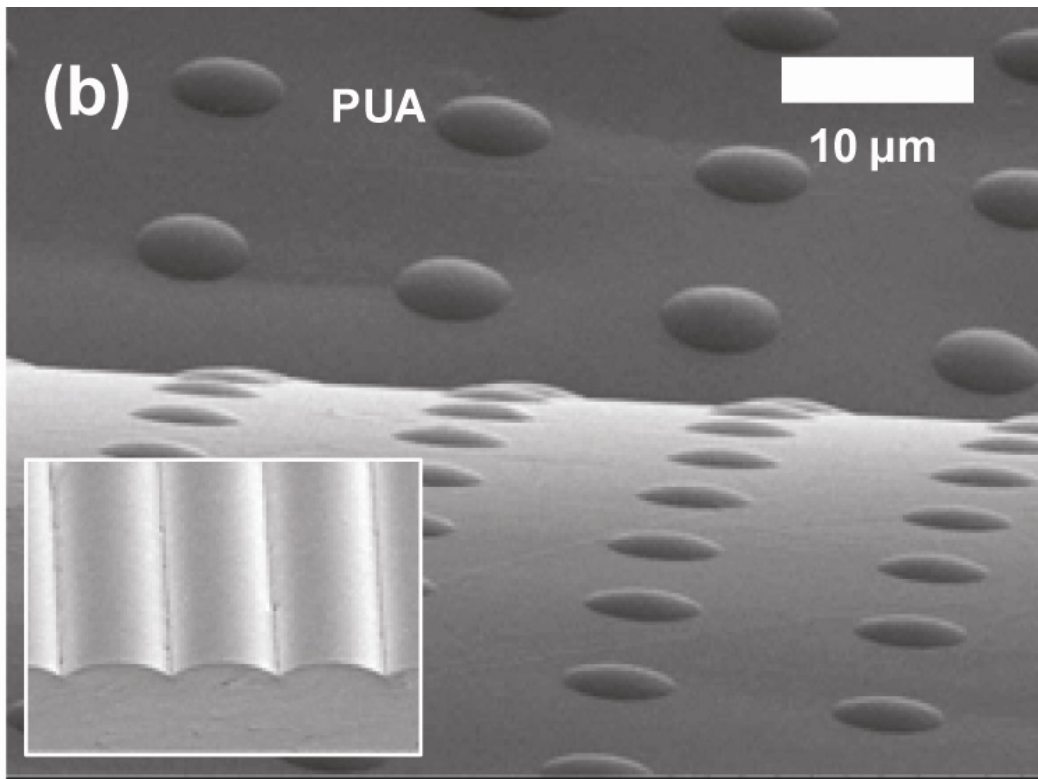


Figure 2-3. (b) PUA lens array on Teflon-coated lenticular lens.

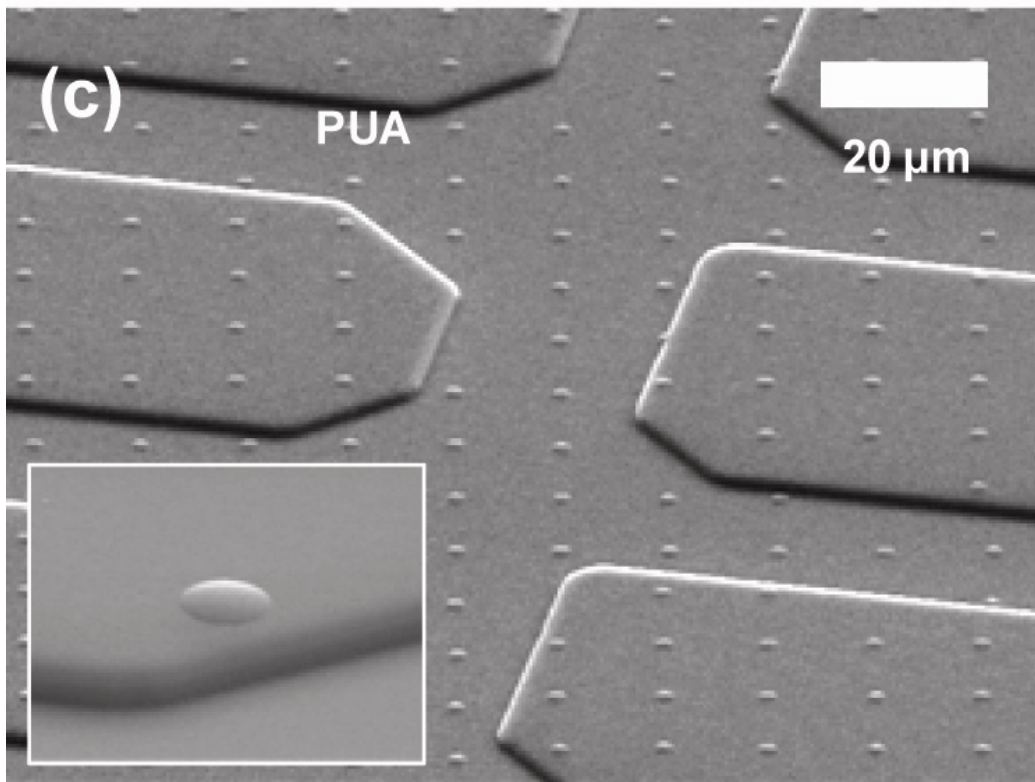


Figure 2-3. (c) PUA lens array on Teflon-coated PDMS pattern.

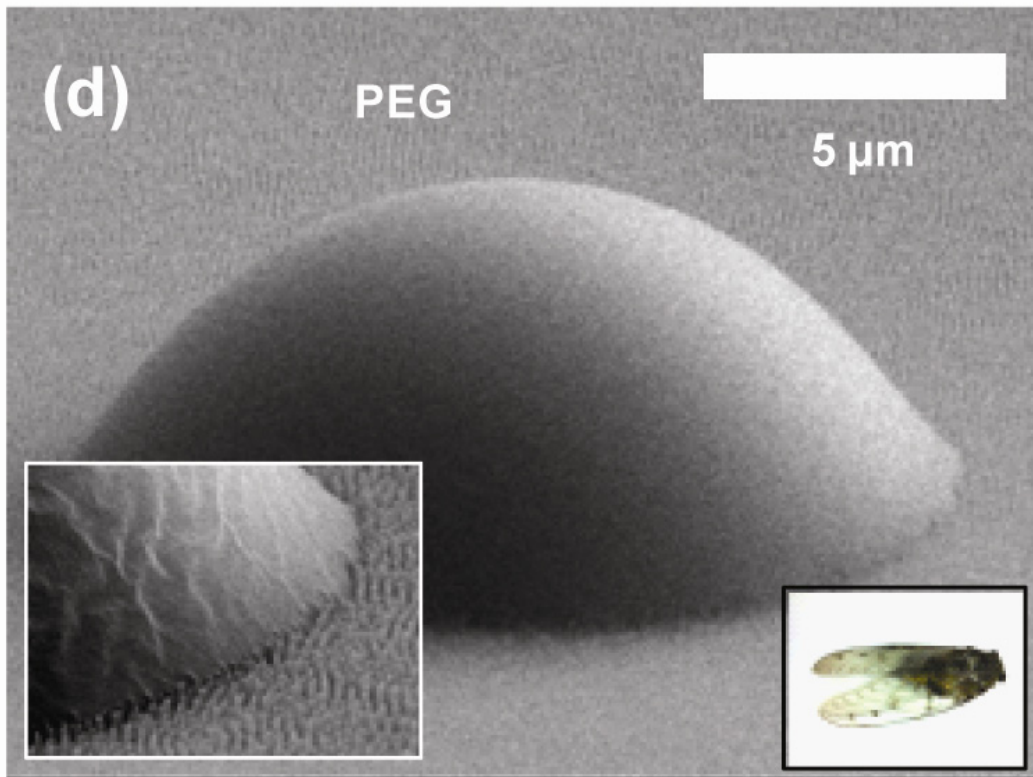


Figure 2-3. (d) PEG lens on Teflon-coated cicada wing.

2-5. Overcoming the diffraction limit

The shape-controllable microlens presented here would be useful to resolve sub-wavelength resolution beyond the Abbe's diffraction limit. To evaluate this potential, we measured nanoscale patterns under an optical microscope. These patterns were prepared by nano-sphere lithography with highly monodisperse 500-nm polystyrene beads (Sigma Aldrich, USA) and subsequent deposition of 50-nm silver layer and lift-off of the beads. [30-32] The resulting patterns were honeycomb-like regular arrays of 500 nm period (Figure 2-4 (f)). The minimal gap was 130 nm for the deposition conditions used in our experiment. Then, a thin liquid of Teflon was coated to the thickness of ~ 5 nm and dried at 70°C in an oven for 5 min so as to give a higher CA of microlens. Finally, by using the procedure shown in Figure 2-1 two polymer droplets (PUA and PEG) were formed on the Teflon-coated substrate. As shown in Figure 2-4(e), the optical images outside of the lens did not resolve the underlying patterns, since the closest gap (130 nm) of triangle nanopattern was narrower than the stringent resolution limit (~ 200 nm). [14]

Figure 2-4(a-d) shows the resulting optical images for 10- μm and 3- μm PUA lenses, and 10- μm and 3- μm PEG lens, respectively. Since PUA and PEG have similar refractive index (PUA = 1.473 and PEG = 1.467), we are able to compare the magnification effect in accordance with the size and curvature of the lens independently. The images were obtained with a $150\times$ objective lens with a

numerical aperture (NA) of 0.9. To determine the focal plane, images were taken from several different focal planes. According to the Rayleigh criterion for point objects ($r = 0.61 \lambda/\text{NA}$, $\lambda = 400 \text{ nm}$), the resolution limit is approximately 270 nm, which is higher than the more stringent Sparrow resolution limit ($r = 0.475 \lambda/\text{NA} = 211 \text{ nm}$). [14] The pattern was imaged within the field of microlens with different light magnification and resolution. For the 10- μm PUA lens, the honeycomb pattern was vaguely seen with a peak-to-peak distance of 600 nm (full width at half maximum, FWHM = 340 nm), suggesting that the magnification was 120%. For the smaller 3- μm PUA lens, the peak-to-peak distance did not change but the contrast was further enhanced as evidenced by a reduced FWHM of 295 nm. However in neither case, we were not able to observe the smallest gap of 130 nm.

For the 10- μm PEG lens, the peak-to-peak distance was increased to 750 nm, indicating that the magnification be further enhanced to 150% (FWHM = 341 nm), because the CA of PEG lens was elevated from 64.1° to 90.9° (Figure 2-2(c)). The smallest gap still portrays an obscure image at this magnification, however. For the 3- μm PEG lens, one can see a clear honeycomb pattern with a distinguishable gap (FWHM = 296 nm) between the hexagonal patterns. The gap distance in the optical image was $\sim 250 \text{ nm}$, larger than the expected value of 195 nm. As compared with four microlens types in Figure 2-4, the 400-nm polymer lens array was not suitable for the visualization as they gave a very narrow field of view, in agreement with an earlier report. [14] Therefore, the 3- μm PEG lens of $\text{CA} = 90.9^\circ$ yielded the

maximum focusing effects among the various lens shapes used in the experiment. In view of our observations, an optimal lens size can be determined to meet high resolution imaging as well as large field of view.

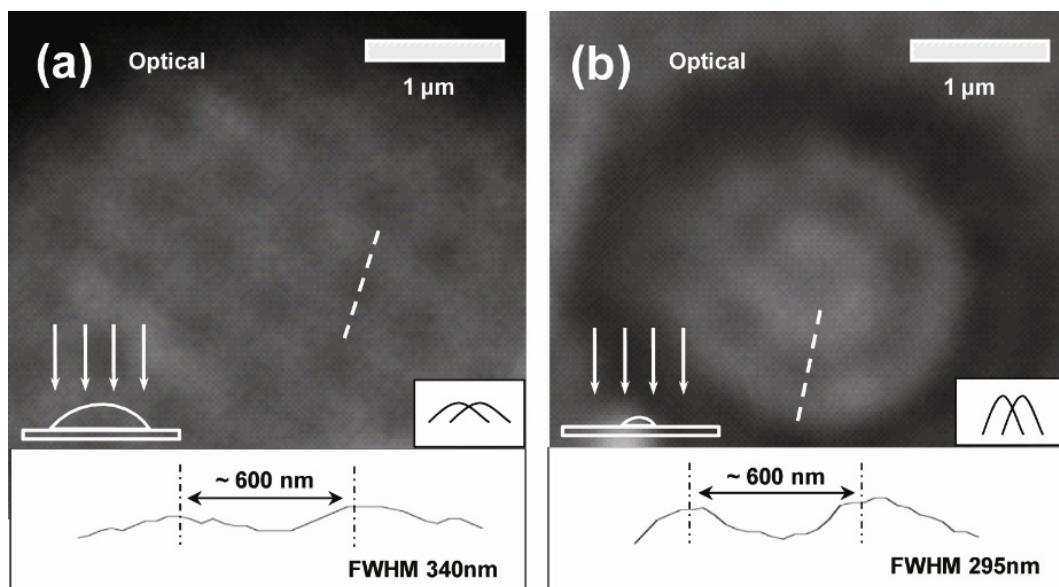


Figure 2-4. Visualization of nanoscale features using plano-convex lenses. (a-b) Optical images of nano pattern through 10-μm (a) and 3-μm (b) PUA lenses along with their cross-sectional profiles.

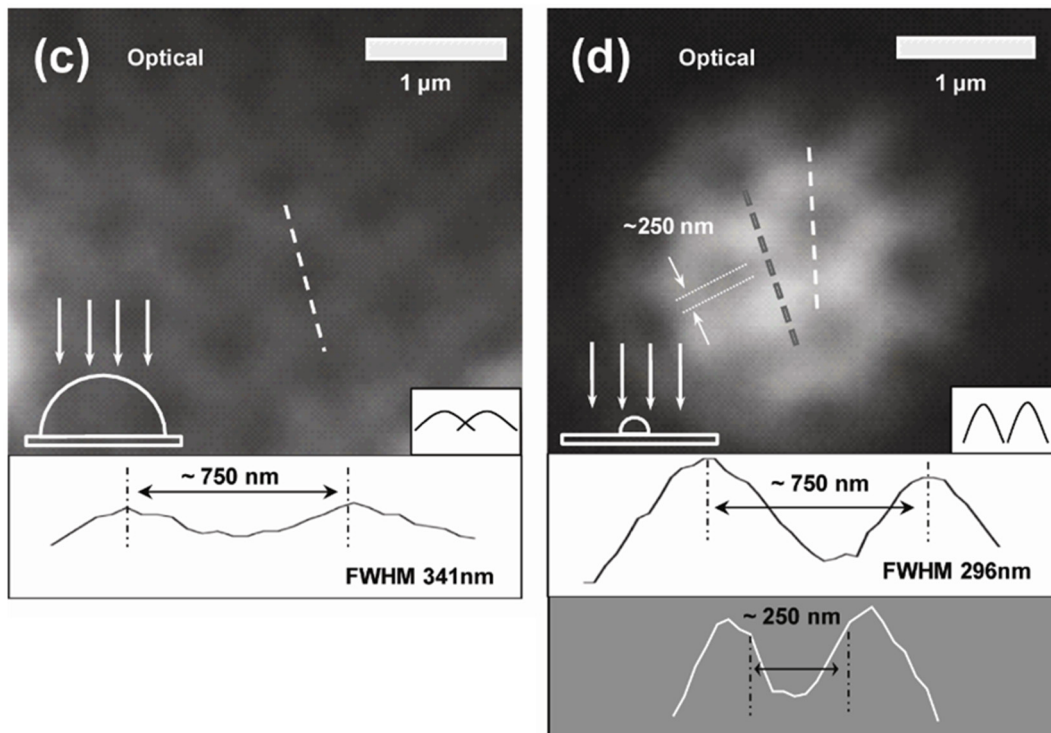


Figure 2-4. (c-d) Optical images of nano pattern through 10- μm (c) and 3- μm (d) PEG lenses along with their cross-sectional profiles.

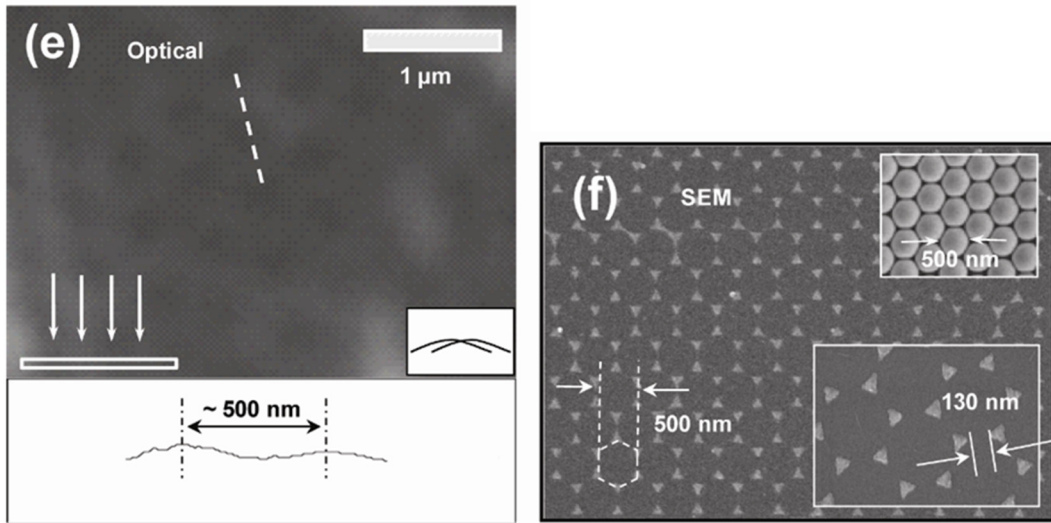


Figure 2-4. (e) Optical image and cross-sectional profile of nano pattern without lens. (f) SEM image of silver nano pattern made by nano-sphere lithography. (Inset): SEM images of close-packed polystyrene nano beads (upper) and resulting silver nano pattern after lift-off (bottom).

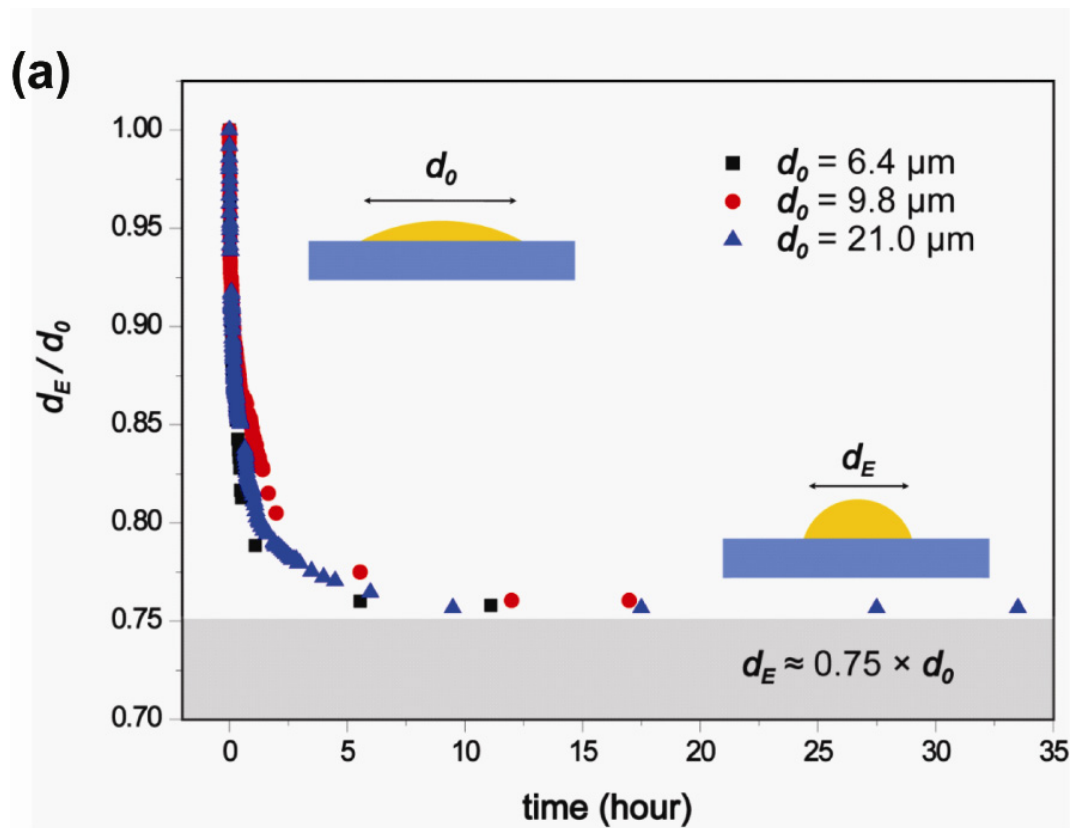


Figure 2-5. (a) Temporal evolution of the contact diameter of plano-convex lenses using UV-curable PUA polymer on PDMS substrate.

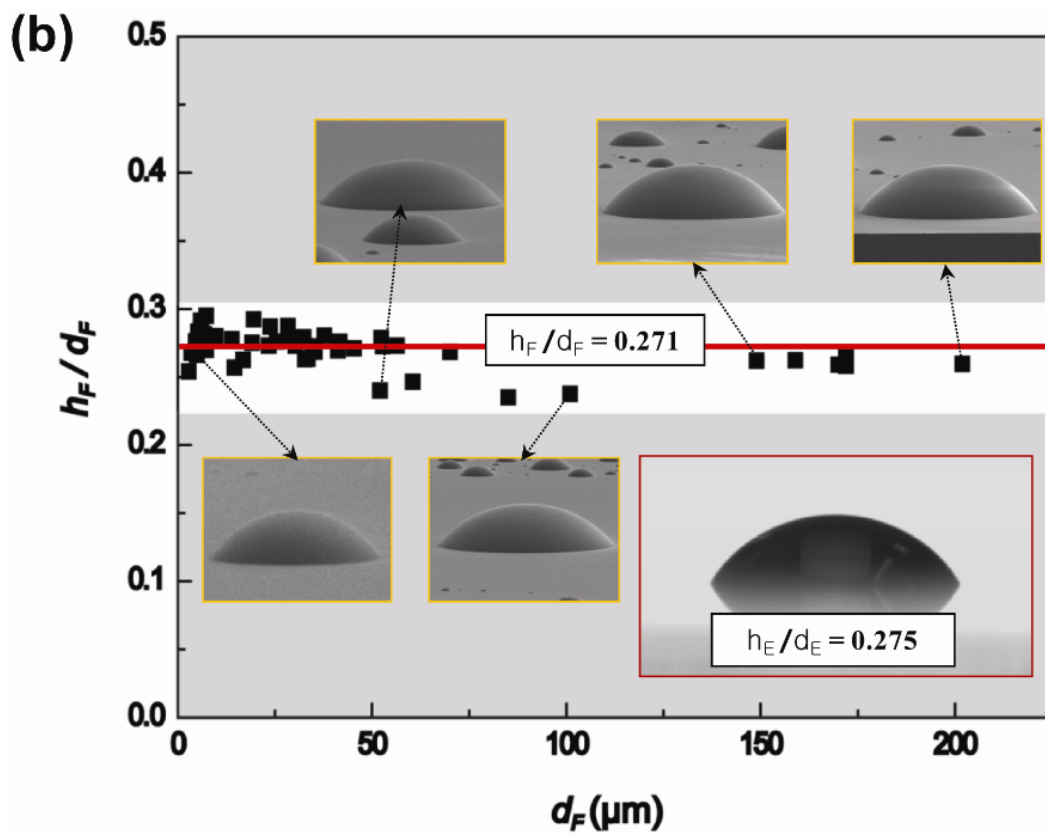


Figure 2-5. (b) Plot of the ratio of equilibrium lens height to diameter as a function of lens diameter (yellow box: SEM image. red box: optical image)

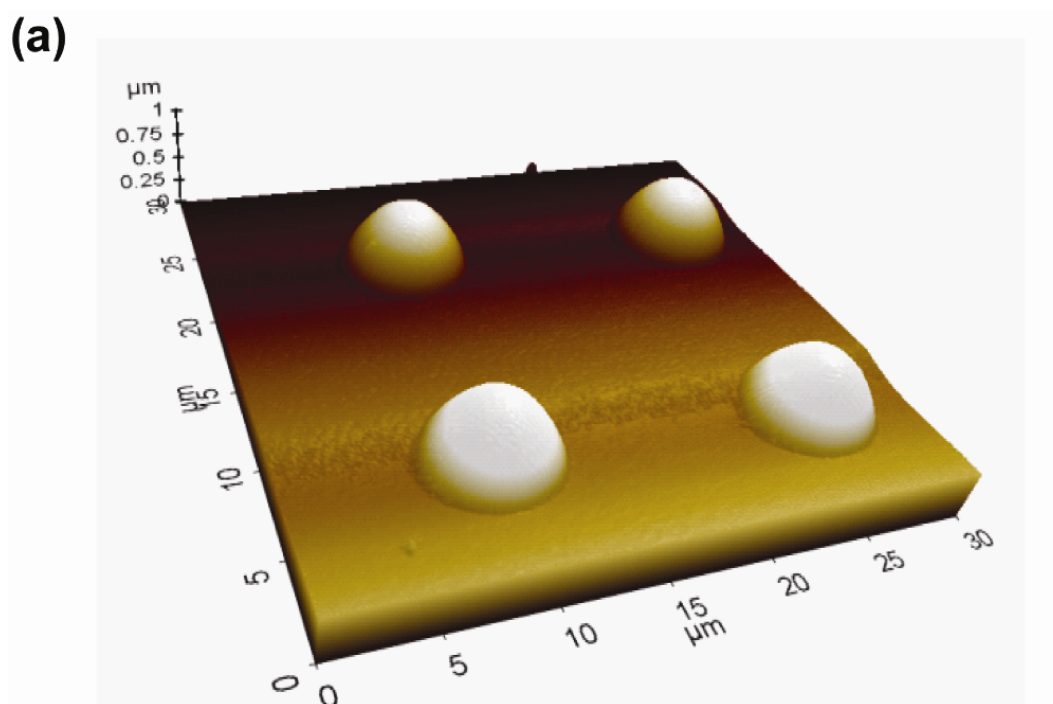


Figure 2-6. (a) Three-dimensional AFM image of an array of PUA lenses with an equilibrium diameter (d_e) of $\sim 6.2 \mu\text{m}$

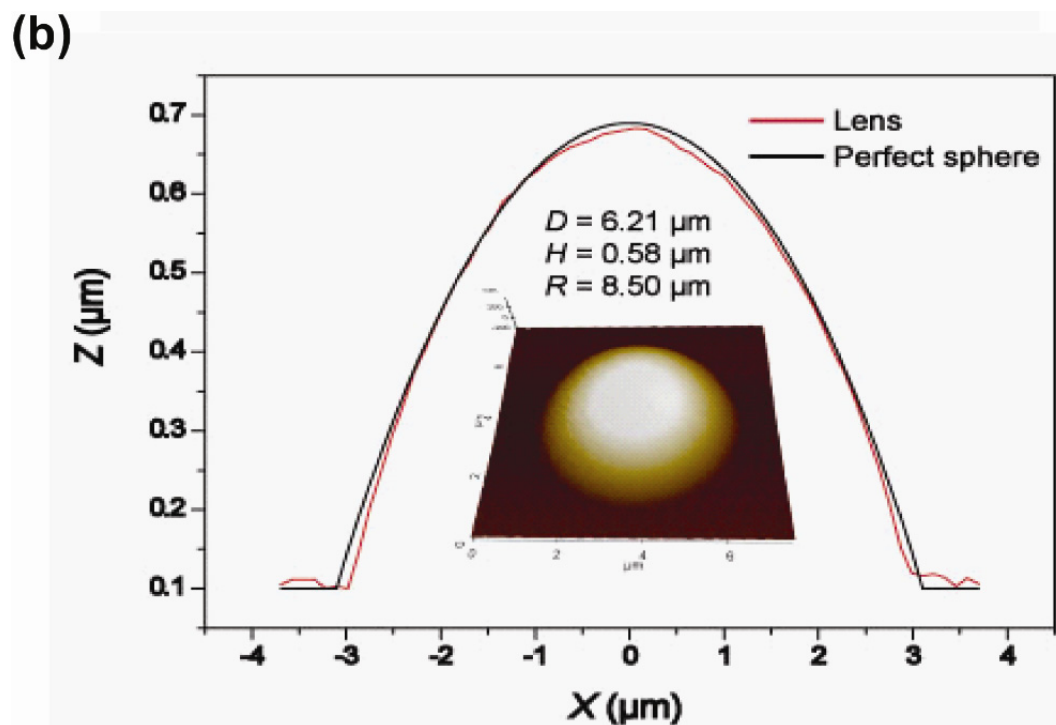


Figure 2-6. (b) Cross-sectional view of one microlens overlapped with the profile of a perfect sphere.

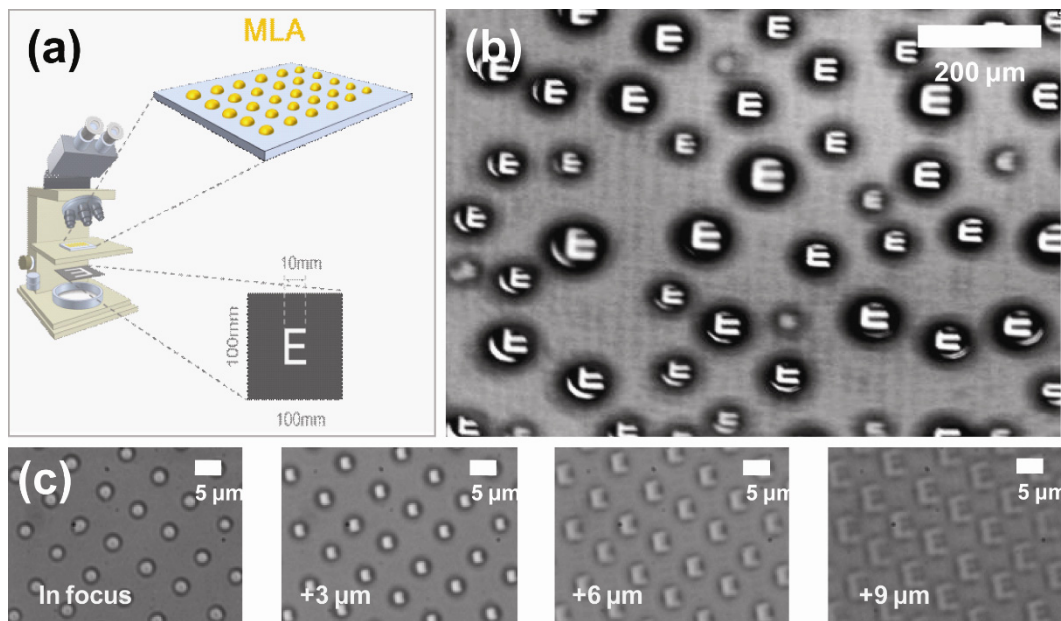


Figure 2-7. (a) Experimental setup of the projection experiment. The black polymer sheet with a transparent letter ‘E’ at its center was prepared by a laser printer. (b) Optical micrograph of the projected images through the randomly placed PUA lens array (c) Optical microscope images projected through the PUA lenses ($d = 3 \mu\text{m}$, $h = 300 \text{ nm}$) on vertical image planes at varying distances z . The number in each slice denotes the value of z . ‘In focus’ denotes the image focused on the plane of the PUA lens.

2-6. Summary

There are a number of distinct advantages with the current method. First, one can readily control the dimension and curvature of the lens shape by adjusting the geometry of PDMS mold and interfacial tensions (Figure 2-2). Second, such a geometry-controllable lens can be transferred virtually to any solid substrate with a moderate surface roughness (Figure 2-3). Third, a dense array of microlens can be formed with the identical dimension, allowing for a high-density optical sensing or lithography. There is also a potential weakness of our method that the pattern to be imaged needs to be coated with Teflon in order to achieve a high contact angle. To address this issue, we are currently working on an improved method to transfer the microlens array onto a thin membrane, which is then moved to a target substrate and used for high resolution imaging. With further optimization, the method presented here would be useful in a variety of applications involving remarkably short focal length and high-resolution optical imaging at low intensities.

In conclusion, we have presented a simple method for fabricating shape-controllable lens array by utilizing direct transfer of photo-curable polymer droplets onto a target substrate. The ability to tailor the final shape of the transferred lens array was evaluated by transferring various sizes of lenses (diameter: 481 nm – 15.5 μm) on solid substrates. We observed that the shrinkage was negligible during the photo-curing step. Also, PUA or PEG lenses of different convex configurations

(contact angle: $9.8^\circ - 90.9^\circ$) were transferred onto various substrates having different curvature, step, or topography. Using the microlens array, nanoscale features as small as 130-nm gap distance was visualized under an optical microscopy using 3- μm diameter lens array with the CA of 90.9° .

Chapter 3. Spider-inspired Nanoscale Crack Sensor

3-1. Objective

Arachnids are among the most sensitive creatures on Earth. [33] In particular, their mechanosensory system, which is embedded in a crack-shaped slit organ made of a stiff exoskeleton over a cuticular pad near the leg joints, senses extremely small variations in mechanical stress, thereby serving as an ultra-sensitive vibration sensor. Here, we demonstrate that spider-inspired sensors based on nanoscale crack junctions can attain ultrahigh sensitivity and can serve as multifunctional sensors. The results obtained in this work represent the highest sensitivity in strain (gauge factor of approximately 2,000 at 2% strain) and vibration (approximately 10 nm amplitude detection capability) achieved by a multifunctional sensor to date. The device is reversible, reproducible, durable and mechanically flexible, and thus, it can be easily mounted on human skin as skin electronics with multi-pixel arrays. The ultrahigh mechanosensitivity is attributed to the disconnection/reconnection process of the zipper-like nanoscale crack junctions. The proposed theoretical model is consistent with the experimental data. We also demonstrate that the sensory system is applicable for highly selective speech pattern recognition and the detection of physiological signals from humans. The spider-inspired sensory system

would provide versatile novel applications requiring ultra-high displacement sensitivity.

Biomimicry often offers attractive technological opportunities that can solve complex problems in current technologies. Examples such as compound-eye-like cameras [34,35], spider-web-like water collection [36], Gecko-like directional adhesion [37] and the interlocker system from a beetle's wing [38] have unique geometries and artificially produced functions. In particular, *arachnids* have several ultra-sensitive sensory systems to monitor the surrounding in which they live. For example, *arachnids* have thin hairs on their legs that are capable of hearing localized sound origin and a crack-shaped slit organ to read vibrations from their surroundings [33]. Therefore, their sensing mechanism and the geometry of their sensory system have been studied extensively [39], and it is beneficial to mimic this system with a simplified form to design novel ultra-mechanosensitive sensors for practical applications.

Several mechanosensitive sensor works using semiconductor and carbon materials have been presented in recent years. Sensor devices based on ultrathin inorganic silicon [40-42], organic semiconductors [43-45], carbon nanotubes (CNTs) [46], graphene [47], pressure-sensitive rubber [48] and self-powered sensors [49,50] on flexible substrates have exhibited high sensitivity and compatibility with human skin. However, these devices could not compete with the spider's ultrahigh mechanosensitivity resulting from its crack-shaped slit sensory

organ (see Figure. 3-5). However, cracks are typically considered as a defect to be avoided [51,52]. Recent works demonstrated that crack formation could be controlled rather well using notches and confined surface stress [52-54]. Here, we present a spider-inspired ultra-mechanosensitive multifunctional sensor based on nanoscale crack junctions and demonstrate its ultra-high sensitivity for detecting physiological signals in the human body (i.e., speech pattern recognition and heart rate) and external forces (i.e., pressure, strain, and vibration). We elucidated the underlying mechanism concerning how ultra-high sensitivity is obtained through controlled crack junctions made in thin metallic films on top of soft polymer substrates. The intriguing disconnection/reconnection process of crack junctions is attributed to the ultrahigh sensitivity of our crack-based sensor. The nanoscale crack-based sensor satisfies the most desired properties, such as reproducibility with high sensitivity, mechanically flexible geometry, localized sensing, and bending robustness and durability. Furthermore, our nanoscale crack-based sensor can be made as a multi-pixel array to independently detect vibration frequency at multiple locations. To our knowledge, the results obtained here represent the highest sensitivity achieved by a multifunctional sensor to date (see Figure. 3-5). The sensor has a gauge factor of over 2,000 ($= (R/R_0)/\varepsilon$) at 2% strain and can detect amplitude vibrations of less than 10 nm (the spider's slit organ is known to have an amplitude vibration detection ability of 1-10 nm) [33]. The sensor is reversible, reproducible and durable. Moreover, the developed theoretical model of conductance through

crack-junctions corresponds well with the experimental data.

3-2. Fabrication method of nanoscale crack sensor

An illustration of the spider's slit sensory organ is presented in Figure 3-1. The spider in Figures 3-1A and B, *Cupiennius salei*, has strain detectors located in the vicinity of the leg joint between the *metatarsus* and *tarsus* [33]. The detectors are composed of a visco-elastic pad (Young's modulus of 15 MPa) with the slit organ consisting of approximately parallel sensory lyriforms (a scanning electron microscope (SEM) image is shown in the inset of Figure. 3-1B) embedded in the mechanically stiff (150 GPa) exoskeleton shown in Figure 3-1C. The slits are directly connected to the nerve system to collect and recognize external vibrations. In this work, we mimic their slit organ to design novel ultra-sensitive sensors. Mimicking the exoskeleton and viscoelastic layers of spiders, our sensor has a stiff metallic layer (168 GPa, approximately 20 nm platinum (Pt)) on top of a viscoelastic UV curable polymer (19.8 MPa, polyurethane acrylate (PUA) (301RM, Minuta Tech Inc., Osan-Si, Gyeonggi-do, South Korea)) [55,56]. Analogous to crack-shaped slit organs, we generate controllable cracks in the Pt film, through which electrical conductance is measured. The electrical conduction measurement through Pt crack junctions resembles the strain sensing of lyriform located within

the crack-shaped slit of the exoskeleton. The PUA layer is fabricated by dripping urethane acrylate precursors on a flexible polyethylene terephthalate film (50 μm thick, SH40 SKC Inc.) and then covering the film with a flat silicon wafer followed by 350 nm ultraviolet (UV) flood exposure (approximately 360 mJ/cm^2). A patterned 20- to 100-nm-thick metal layer is formed by a shadow mask using sputtering (Muhan Vacuum Inc.) (see Figure. 3-6). This metallic film on PUA is mechanically bent by applying various radii of curvature (1, 2, 3 mm), and the cracks are formed in a highly controllable manner in terms of crack density and direction, which in turn yields reproducible electrical signals (which will be discussed later). As observed in Figure 3-7, the crack spacing (or density) can be controlled by bending the sample with different curvatures. For example, the average spacing between cracks is approximately 10 μm when the sample is bent with a curvature of 1 mm. The sensor performance is affected by the crack density, as will be discussed later. The cracked Pt on PUA shown in Figure 3-1D has lateral dimensions of $5 \times 10 \text{ mm}^2$ on 10- μm -thick PUA. Figure 3-1E illustrates that cracks are formed in the transverse direction to the extension force applied with a bending curvature of 1 mm. The atomic force microscopy (AFM) images in Figure 3-8 clearly illustrate that the crack penetrates beyond the Pt film thickness (20 nm) into the PUA substrate (crack depth of approximately 40-50 nm) [55,57]. The crack gap increases with increasing strain, as shown in the AFM images of Figure 3-8 and the SEM images of Figure 3-1G. Even at 0% strain, a small gap exists between

mating cracks (approximately 5 nm), indicating that not all of the mating cracks are contacted. A simplified schematic of our nanoscale crack-based sensor is illustrated in Figure 3-1F. Figure 3-1H illustrates the widening of the 50-nm-deep crack gap with stretching by FEM simulations.

Similar to a spider, whose neurons detect the local stress in the crack dells (Figure. 3-1C), our sensor detects the resistance of the Pt bridges through the crack gap made by the asperity of the crack lips. The resistance of a metal strip with a straight transverse cut may experience a sudden jump from a finite value, when the lips of the cut are contacting, to infinity, when they disconnect instantly, similar to the Morse “yes/no” telegraph signal, which could theoretically bring the gauge factor to infinity. For cracks in the Pt film, the phenomenal strain sensitivity originates from the rare but large crack gap-bridging steps on opposite matching lips of a zigzag crack.

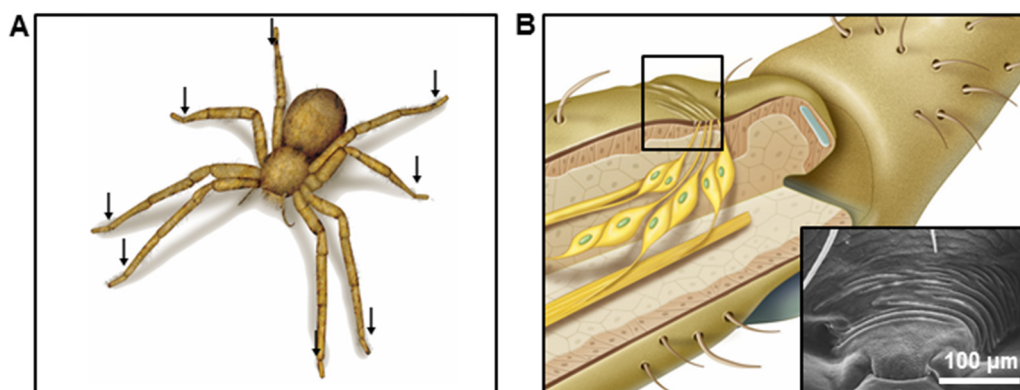


Figure 3-1. Schematic illustrations and images of ultra-mechanosensitive nanoscale crack-based sensor inspired by the spider sensory system. (A) Illustrations of the *Cupiennius salei* spider. The spider has highly sensitive organs located on its leg joints (black arrows) for the detection of external forces and vibrations. **(B)** Enlarged images of the sensory slit organs in the vicinity of the leg joint between the *metatarsus* and *tarsus*. The inset shows an SEM image of the slit organ.

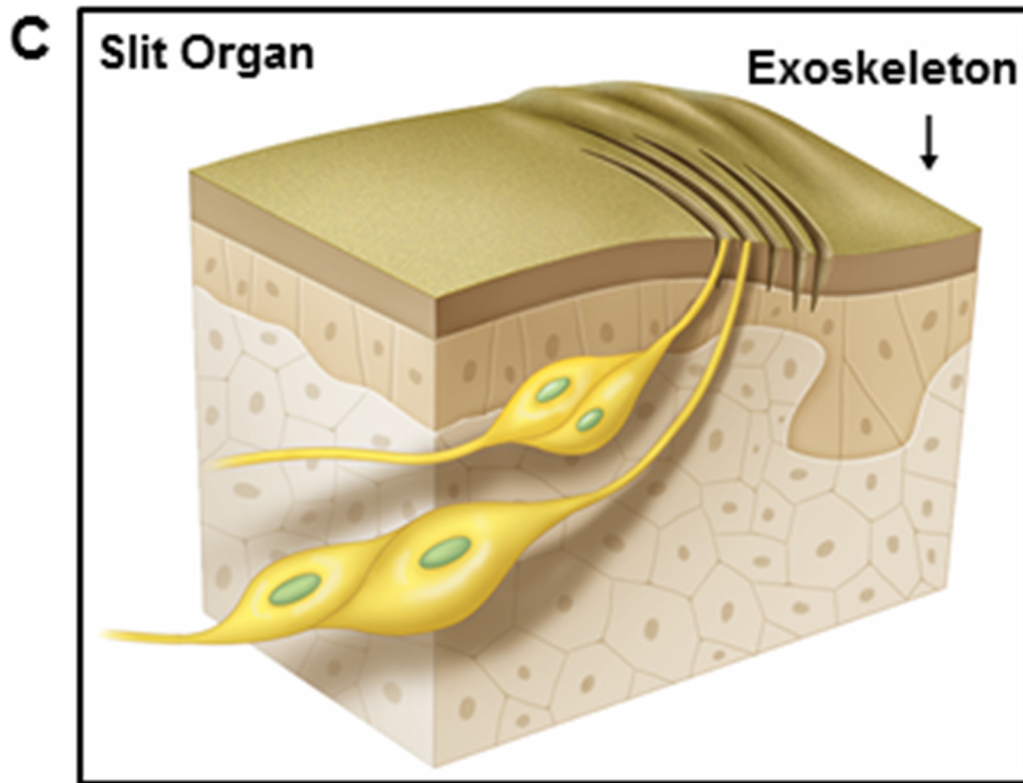


Figure 3-1. (C) The slits are connected to the nerve system to monitor vibrations. The slits are embedded in the highly stiff exoskeleton (surface) and a viscoelastic pad (inner).

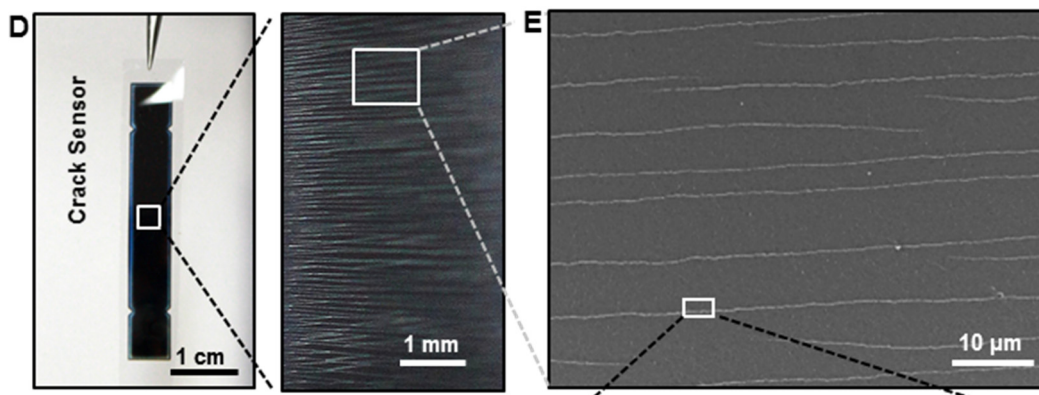


Figure 3-1. (D) (Left) Image of the spider-inspired sensor with a cracked 20-nm-thick Pt layer formed by bending with a 1-mm radius of curvature. The sensor has lateral dimensions of $5 \times 10 \text{ mm}^2$ on 10- μm -thick PUA. (Right) Enlarged image of the cracks from the surface of (D). (E) SEM image of the left image of (D).

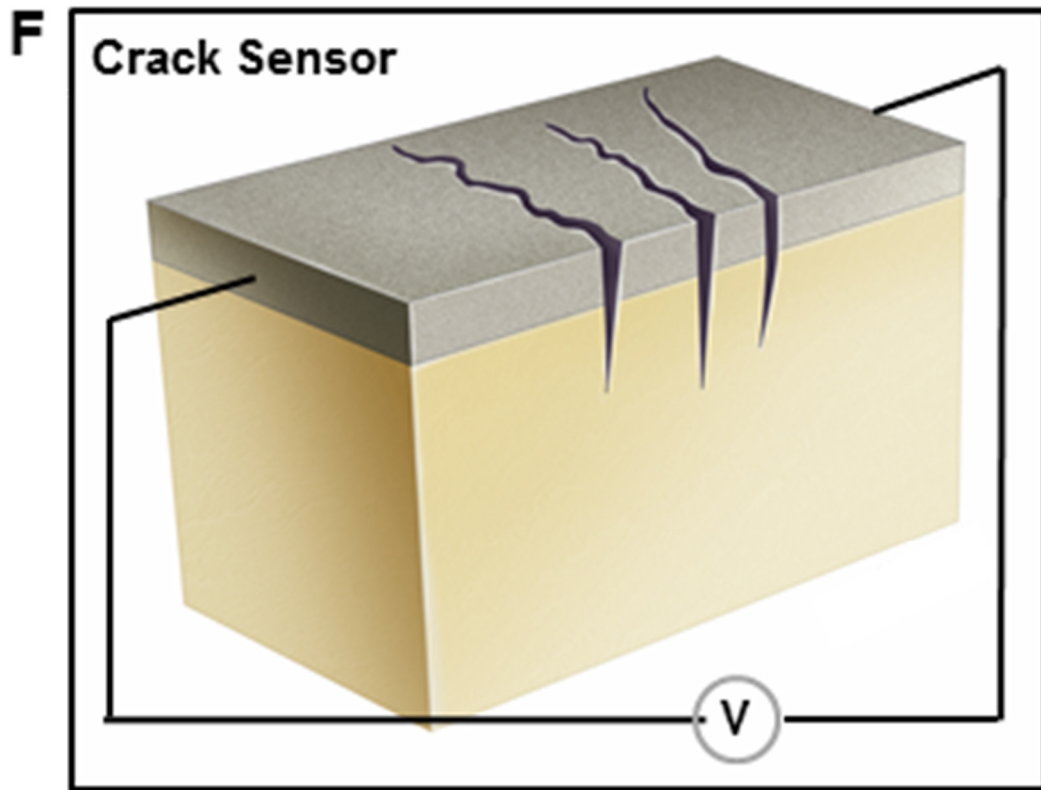


Figure 3-1. (F) Illustration of the crack-based sensor and its measurement scheme.

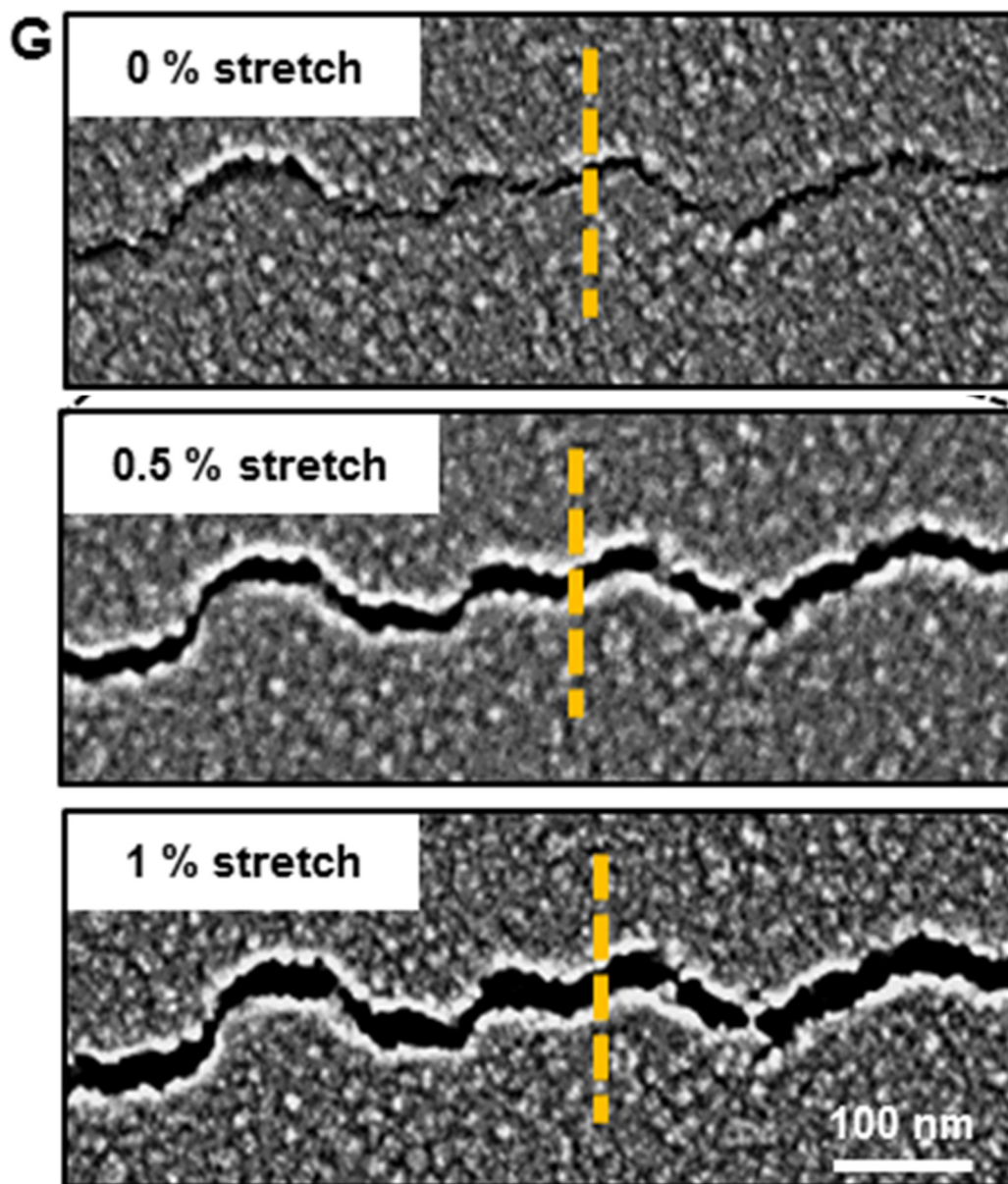


Figure 3-1. (G) SEM images for the zipper-like crack junctions for different applied strains: 0% (left), 0.5% (middle), and 1% (right).

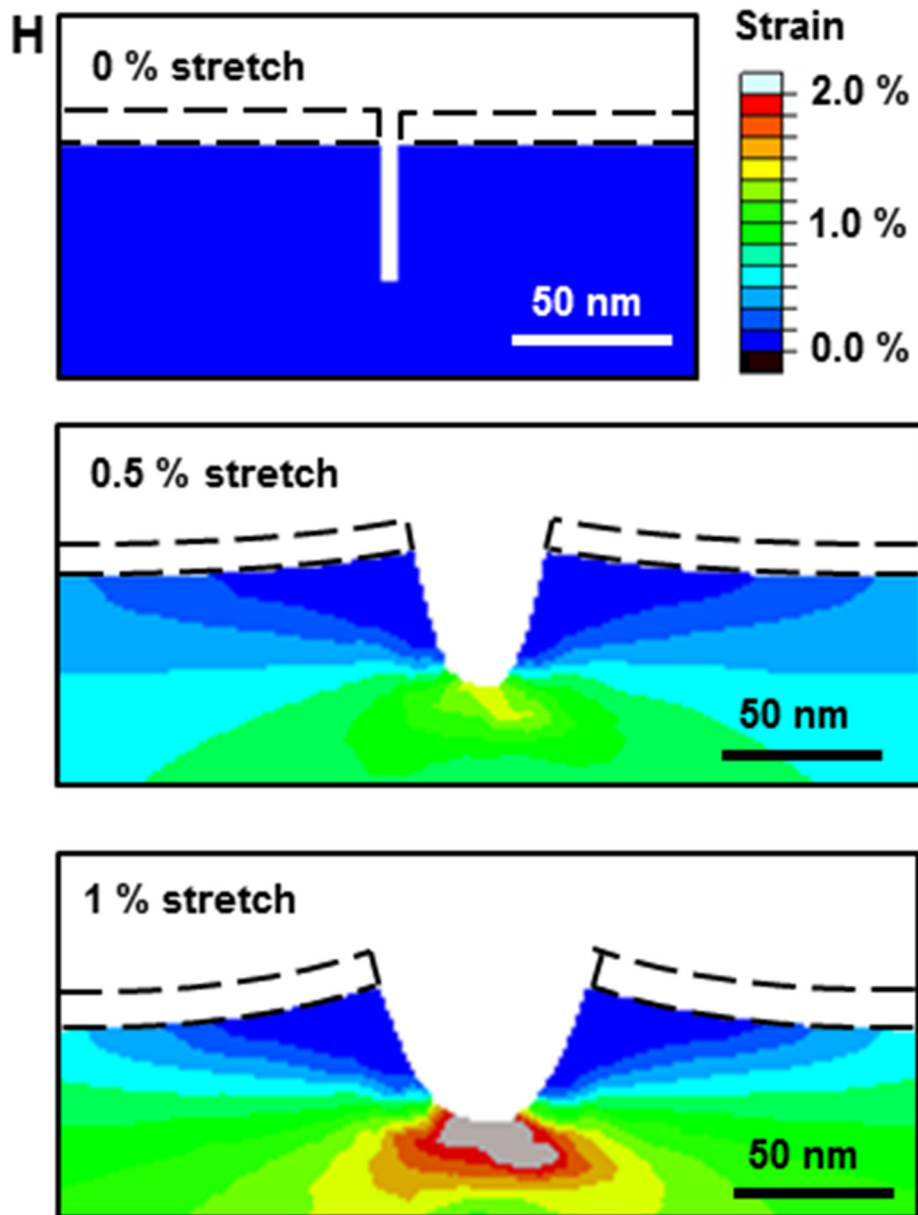


Figure 3-1. (H) FEM modeling results of crack interfacial deformation by 0% (left), 0.5% (middle), and 1% (right) strain. The white regions surrounded by black dashes represent the 20-nm-thick Pt.

3-3. Results and theoretical analysis

Large variations in resistance are obtained with high repeatability for the cracked sample with a curvature bending of 1 mm while loading the sensor up to 2% strain and unloading back to 0% strain at a sweeping speed of 1 mm/min (see Figure. 3-2A). Figure 3-2B shows such cyclic variations of resistance with different peak strains selected in sharp contrast to the nearly flat bare Pt film case with no crack (yellow curve). The current-voltage (I-V) curves for the crack sample and bare film case without a crack are presented in Figure 3-9 for various strains. The same cyclic measurements performed at a slower sweeping speed of 0.1 mm/min in Figure 3-2C clearly show that loading and unloading are nearly reversible. When compared with the case of the bare Pt film with no crack (see the inset of Figure. 3-2C), the crack sample exhibits a 450 fold higher resistance variation (ΔR) at 0.5% strain. At 2% strain, the gauge factor exceeds 2,000, which, to our knowledge, is the highest gauge factor achieved by a multifunctional sensor to date. We obtained reproducible results from five samples, as shown in Figure 3-10. The sensor performance remains unchanged after 1,000 loading and unloading cycles under 0.5% strain (see Figure. 3-11 for the durability test). As noted earlier, controlled crack formation using different curvature bending resulted in different crack spacings, as shown in Figure 3-7, and affected the sensor performance in a controllable manner (see Figure. 3-12).

The inverse of R/R_0 , which is the normalized conductance, $S = R_0/R$, is plotted in Figure 3-13, revealing an intriguing fluctuating behavior, particularly at lower strains (see the inset of Figure. 3-13). Further insight into the elementary acts of the connection/disconnection of cracks during the loading strain can be obtained by considering the derivative $-dS/d\varepsilon$. The derivative of the normalized conductance S over strain, $-dS/d\varepsilon$, displays large fluctuations, with negative and positive values, particularly at strains less than 1%, as shown in Figure 3-2D. These fluctuations are well beyond the noise level observed from the bare film case without a crack (see the inset of Figure. 3-2D). We attribute these intriguing fluctuations to the disconnection/reconnection events of the crack lips. A positive $-dS/d\varepsilon$ value represents a disconnection event, whereas a negative value represents the reconnection. A cracked film over an elastic substrate with a positive Poisson's ratio could be compressed in the transverse direction while being extended in the axial direction. This phenomenon indicates that the axial extension could disconnect the crack lips and the lateral compression could reconnect the crack lips (but to different mating surfaces). In Figure 3-2D, there are two distinct strain regions, with the larger strain region being characterized by only positive fluctuations. This fact clearly confirms that larger steps of the crack lips preferably disconnect in a loading mode. At lower strain, the fluctuations are both positive and negative, indicating disconnections/reconnections for numerous tiny steps at the crack lips. The averaging of positive and negative spikes ($\langle -dS/d\varepsilon \rangle$) (red curve

in Figure. 3-2D) yields a positive value in all areas, indicating that the net effect of disconnection/reconnection is to reduce conductance as the extension proceeds. A further detailed description regarding the disconnection/reconnection process is provided in Figure 3-14. This overall behavior of $\langle -dS/d\varepsilon \rangle$ is related to the crack gap asperity distribution because the disconnection/reconnection events should be dependent on the crack asperity size distribution (as will be discussed later). Dynamic sweeping motion results in sweeping-rate-dependent resistance variations, although the curves are nearly reversible, as observed in Figure 3-15, which is attributed to the rate-dependent nature of the crack disconnection/reconnection process (see Figure. 3-15 for further details).

For uniaxial strain, the elastic strip becomes compressed transversally and small steps persist contacting until the strain completely disconnects them. This process occurs when the gap distance overcomes the crack asperity height (in the simplified schematic of Figure 3-2F and G, the total height of two blue piles is defined as the crack asperity height, with each pile representing a small step). The SEM images illustrate that the gap distance is proportional to the strain (Figure. 3-16): $d = k \cdot \varepsilon$, where $k \approx 70 \text{ nm}$ and ε is in %. A central component of the conduction mechanism through a crack is a simplified expression for normalized S that accounts for the sudden termination of a contact when the gap $k\varepsilon$ overcomes the crack asperity height $h_i = k \cdot \varepsilon_i$ (for the definition, see Figure. 3-16). All of the crack surfaces do not touch each other on the opposing side; however, only a small

number of contacts seemingly exist from the magnified images in Figure 3-16. However, considering the width (approximately 5 mm) and density (approximately 1,000 /cm) of cracks, there are many contacted crack surfaces (an order of 10^5) per sensor, and only such crack surfaces lead to variations in the conductance.

Considering the above process, the simplified form of the normalized conductance can be written as

$$S = \frac{\sum N_i \theta(\varepsilon_i - \varepsilon)}{\sum N_i}, \quad (1)$$

where $\theta(\varepsilon_i - \varepsilon)$ is the Heaviside step-function and N_i is the number of crack asperities in height $k\varepsilon_i$. With a normalized probability distribution function of the crack asperity size $p(\varepsilon)$, we rewrite Eq. (1) as

$$S = \int_{\varepsilon}^{\infty} p(y) dy. \quad (2)$$

We find an equation for $p(y)$ using the argument that the small variations in the crack asperity due to grain shifts are distributed in the same manner as the large variations due to grain piling, which is conventional for the renormalization group [58] with the only a “size” parameter – the strain ε_0 that corresponds to the grain size ($d_0 = k \cdot \varepsilon_0$):

$$p(y) dy = \left(\frac{p(\frac{1}{y})}{y^2} \right) dy, \quad (3)$$

where $y = \varepsilon/\varepsilon_0$. The general solution satisfying Eq. (3) is

$$p(y) = \frac{f(\ln(y))}{y}, \quad (4)$$

where $f(x)$ is an even function of its arguments. The well-known *log-normal*

distribution function belonging to the class of a so-called skew distribution with long tails

$$p(\varepsilon) = \exp\left(-\left(\ln\left(\frac{\varepsilon}{\varepsilon_0}\right)\right)^2 / \mu^2\right) / (\varepsilon\mu\sqrt{\pi}) \quad (5)$$

satisfies Eq. (4). Previously, crack asperity heights were approximated by a *log-normal* distribution [59]. Combined with Eq. (5), Eq. (2) yields

$$S = \left(1 - \operatorname{erf}\left(\frac{\ln\left(\frac{\varepsilon}{\varepsilon_0}\right)}{\mu}\right)\right) / 2, \quad (6)$$

where $\operatorname{erf}(x)$ is the error function. Eq. (6) is the resistance $R = 1/S$, which fits the experimental data shown in Figure 3-2C well. The averaging of experimental $-dS/d\varepsilon$, with a different number of data points is shown in Figure 3-2E with the theoretical $-dS/d\varepsilon$ obtained from Eq. (6), indicating good agreement. The size distribution of the crack asperity heights ($p(\varepsilon)$) was measured from 50 SEM images and is presented in Figure 3-2E for comparison with the log-normal distribution (Eq. (5)) and the experimental average $\langle -dS/d\varepsilon \rangle$ because $p(\varepsilon)$ should be equal to $-dS/d\varepsilon$ in our theoretical modeling. The distribution of the crack asperity heights also exhibits a long-tailed skewed distribution and is consistent with Eq. (5) and $\langle -dS/d\varepsilon \rangle$ for large strains. A large discrepancy at small strains is attributed to the fact that an initial gap of 5-10 nm exists even at 0% strain (see Figure. 3-1G, Figure. 3-16), and therefore, many small crack asperities less than the initial gap did not cause variations in the electrical conductance. A different Pt film thickness was also

studied to illustrate that the hysteresis loops are clearly pronounced for a 100-nm-thick Pt film with cracks (see Figure. 3-17 for an explanation of the hysteresis of thick films). A 20-nm-thick gold film was also studied (see Table 3-1 for a comparison of the gauge factors).

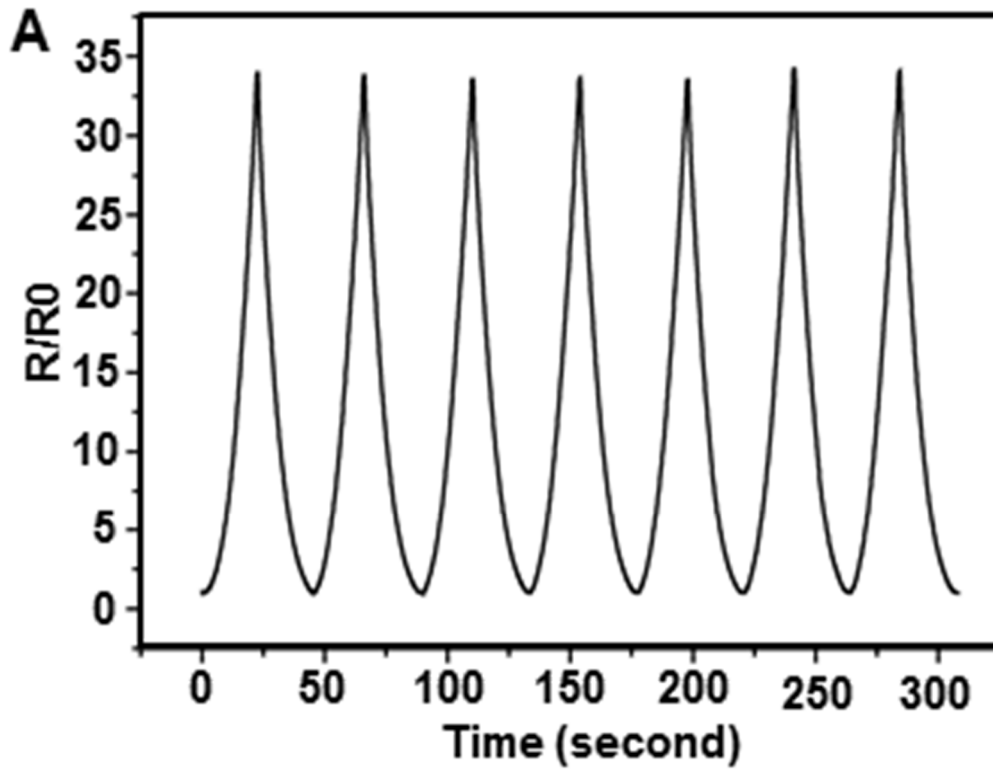


Figure 3-2. Theoretical analysis of the crack sensor. (A) The normalized resistance measured at a strain sweep rate of 1 mm/min.

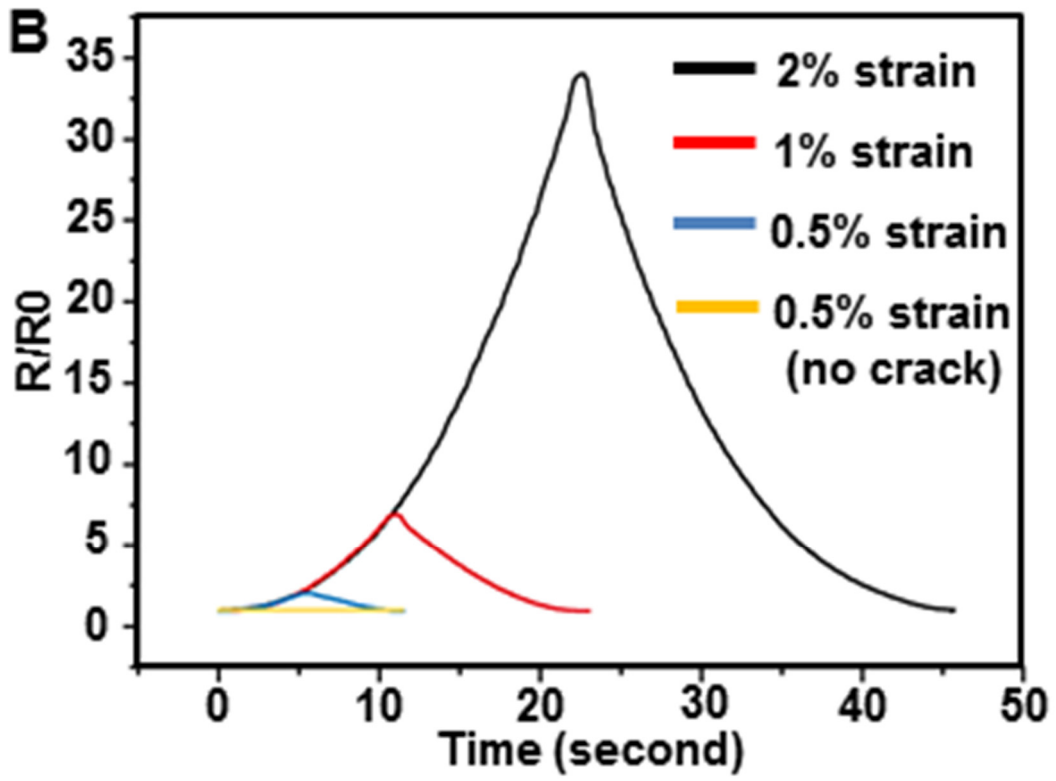


Figure 3-2. (B) Reversible loading/unloading behavior at various final strains.

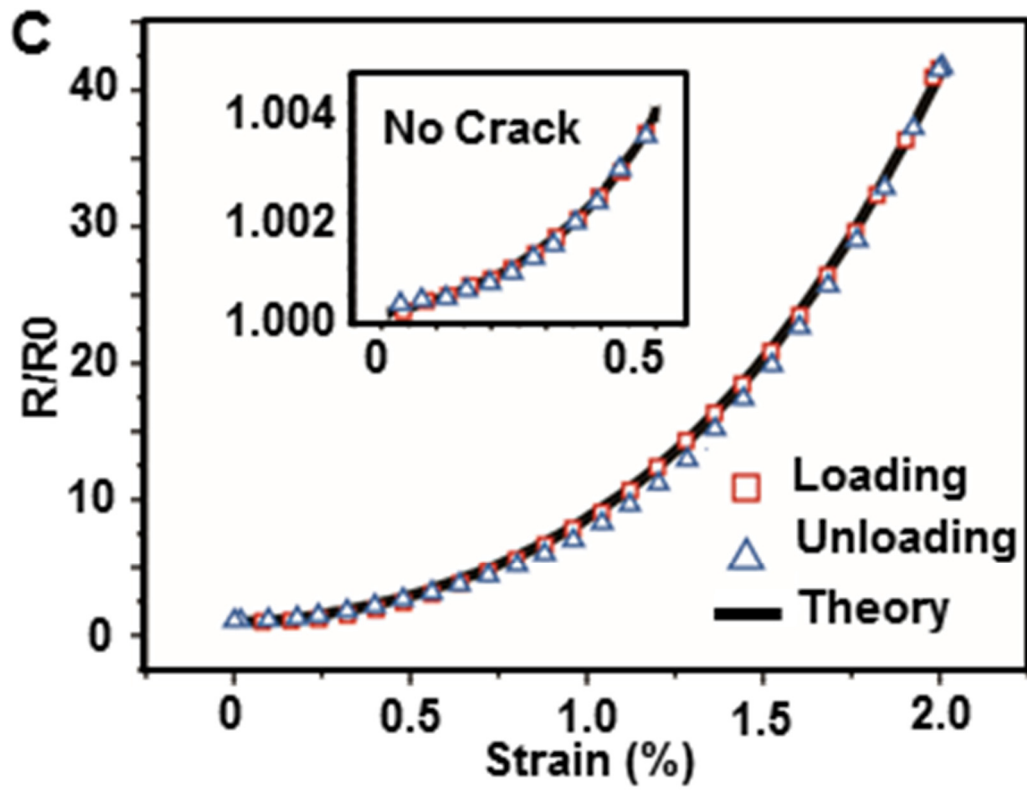


Figure 3-2. (C) Resistance at the slowest loading/unloading rate of 0.1 mm/min compared with the theoretical curve fit. The inset shows the no-crack case.

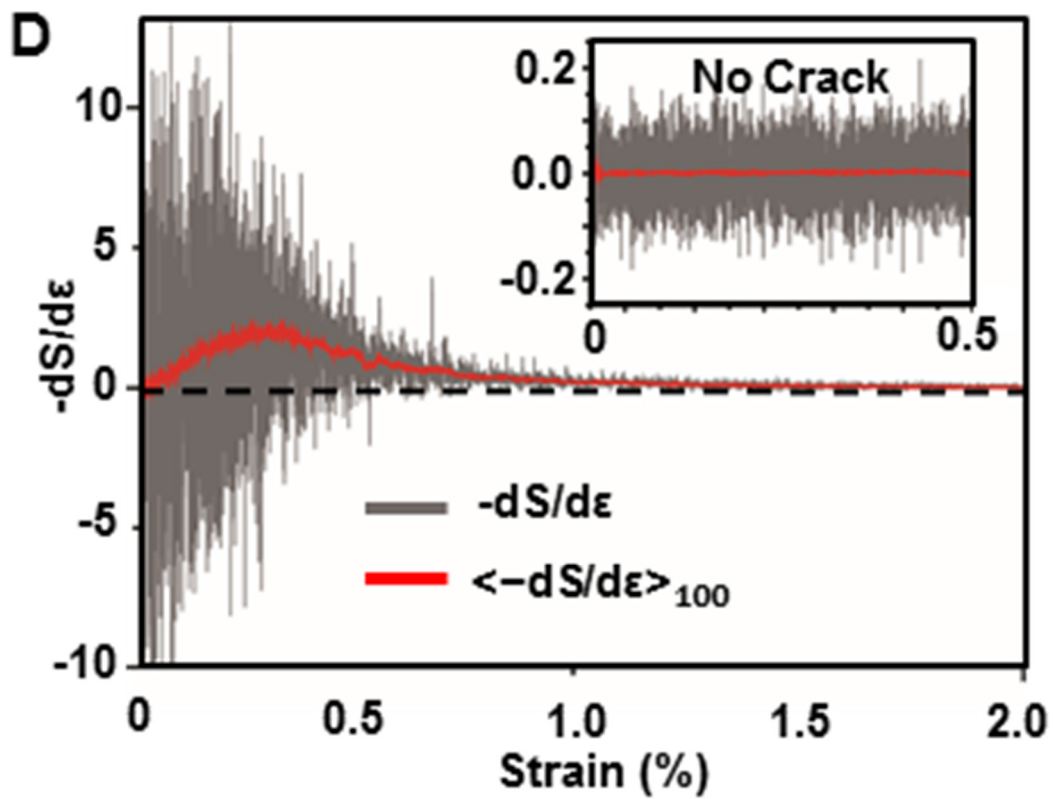


Figure 3-2. (D) The derivative of the conductance with the opposite sign (grey) and its average (red). The inset is the no-crack case.

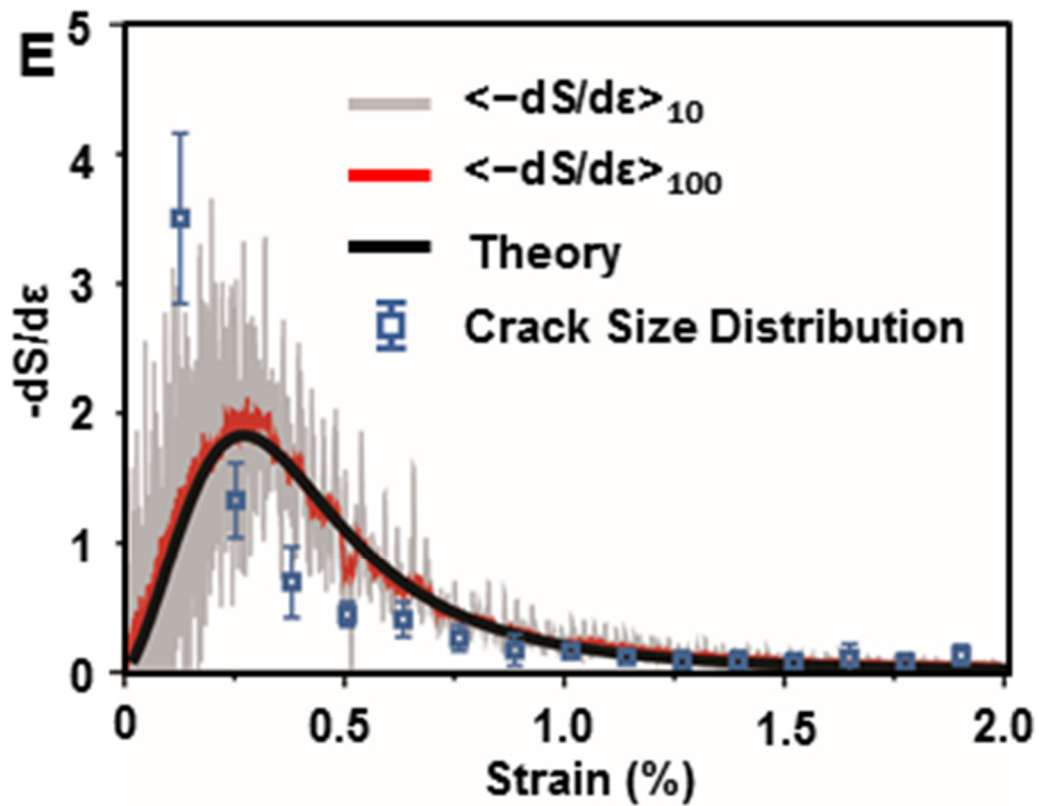


Figure 3-2. (E) The average of the conductance derivative with the opposite sign $\langle -dS/d\varepsilon \rangle$ and comparison of the theoretical fit from Eq. (5) with parameters $\varepsilon_0 = 0.4$ and $\mu = 0.98$ against the average derivative from (D). $\langle -dS/d\varepsilon \rangle_{10}$ and $\langle -dS/d\varepsilon \rangle_{100}$ are the average for 10 and 100 data points, respectively. The maximum at approximately 0.3 corresponds to $k \times 0.3 = 21$ nm, which is close to the constituent primary particle size. The bars show the size distribution of the crack asperity heights derived from SEM imaging of the crack lips.

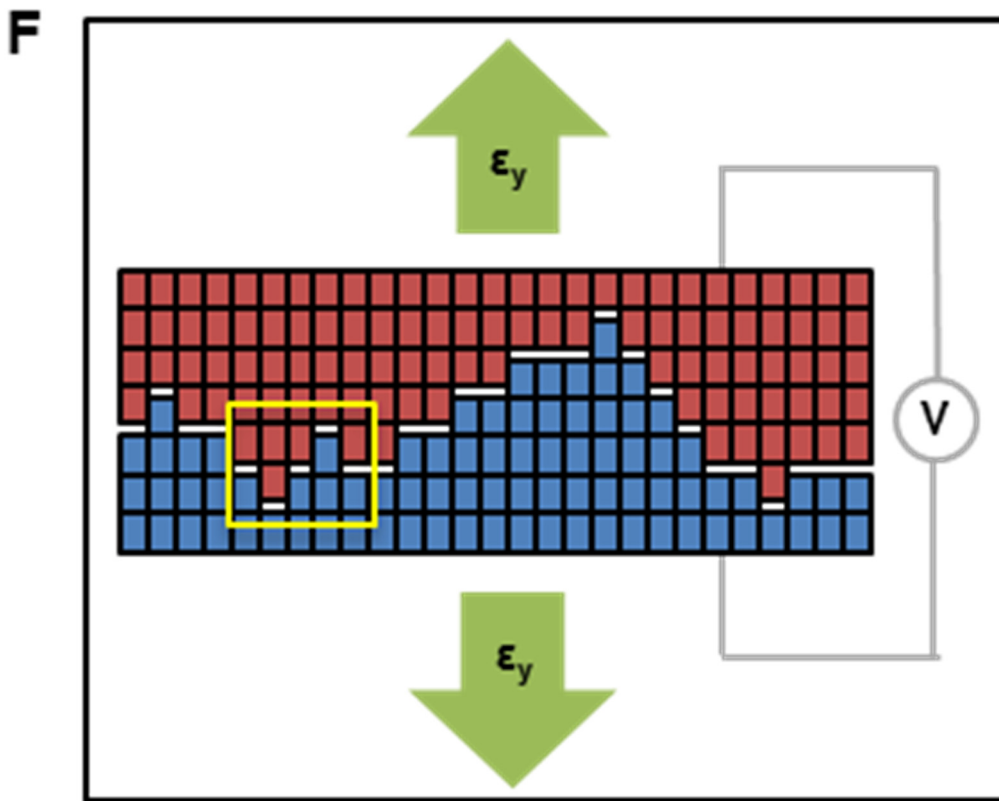


Figure 3-2. (F) Illustration of the matching crack lips.

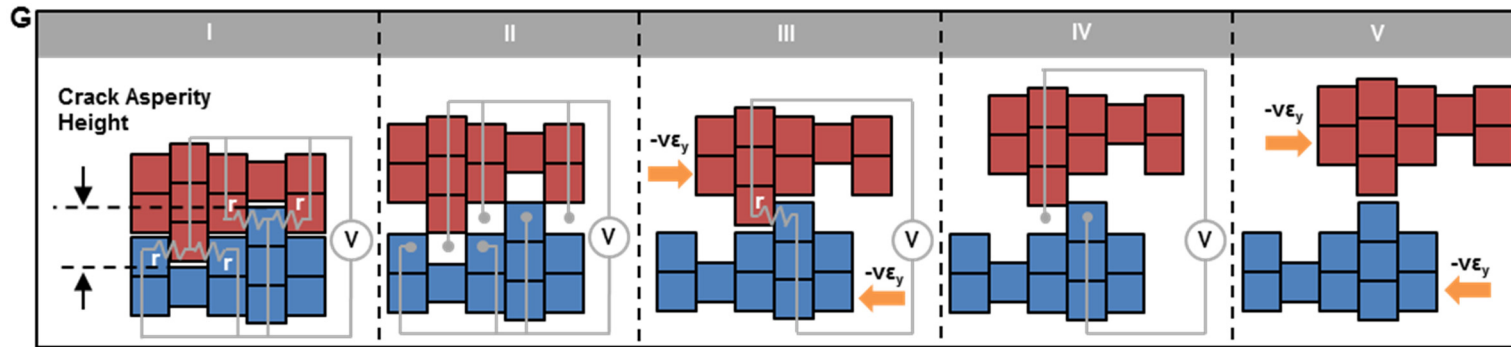


Figure 3-2. (G) Schematic of a crack with the “magnified” crack asperity made of square grains from the yellow box in (F) while performing disconnection/reconnection stages along the step in the vertical loading strain and horizontal compression (orange arrows) with a Poisson’s ratio of $\nu \approx 0.3$.

3-4. Multi-pixel array of the crack sensor

To demonstrate the device's scalability and ability for detecting mechanical vibrations and pressure, a sensing network of 64 pixels (8×8 pixel array) with an area of 5×5 cm² is presented in Figure 3-3. The image and schematic view of the multilayered system are shown in Figure 3-3A-E and Figures 3-18 and 3-19. Each pixel (2×2 mm² islands) composed of 10- μ m-thick PUA/20-nm-thick Pt patterns on PET is formed by conventional photolithography and sputter deposition using a shadow mask, followed by bending with a 1 mm radius of curvature to generate cracks. The electrical connection between the cracked Pt and analyzer (NI instrument) is formed by evaporated gold (Au, 50 nm thick) lines on deposited dielectrics (200-nm-thick SiO₂ by a thermal evaporator; Selcos Inc.). The flexible format of a multi-pixel array (Figure. 3-3D) enables the simultaneous measurement of two different stimuli (pressure and vibration) using a simple analyzer scheme (Figure. 3-3E). The results for static pressure with a PDMS piece (5 Pa in Figure. 3-3B) and a dynamic flapping ladybug (5 Pa pressure and 200 Hz vibration with 14 μ m amplitude in Figure. 3-20) are shown in Figures 3-3F, H (with a PDMS piece) and Figure 3-3G, I (with a vibrator simulating ladybug flapping), respectively. A piece of PDMS is placed on the red marked region in Figure 3-3A, B as a static pressure input, and a piezoelectric vibrator as a vibration source similar to a ladybug's flapping is placed onto the blue marked region in Figure 3-3A, C. The

applied pressure and their distributions from both stimuli can be detected at both spots (Figure. 3-3F). However, the vibration signal is selectively detected only at the spot where the vibration input is applied (Figure. 3-3G). Figures 3-3H and I illustrate the dramatic changes in the in situ signals of these pixels placed at both locations. The applied 200-Hz frequency vibration could be obtained by Fourier transform, as shown in the inset of Figure 3-3I.

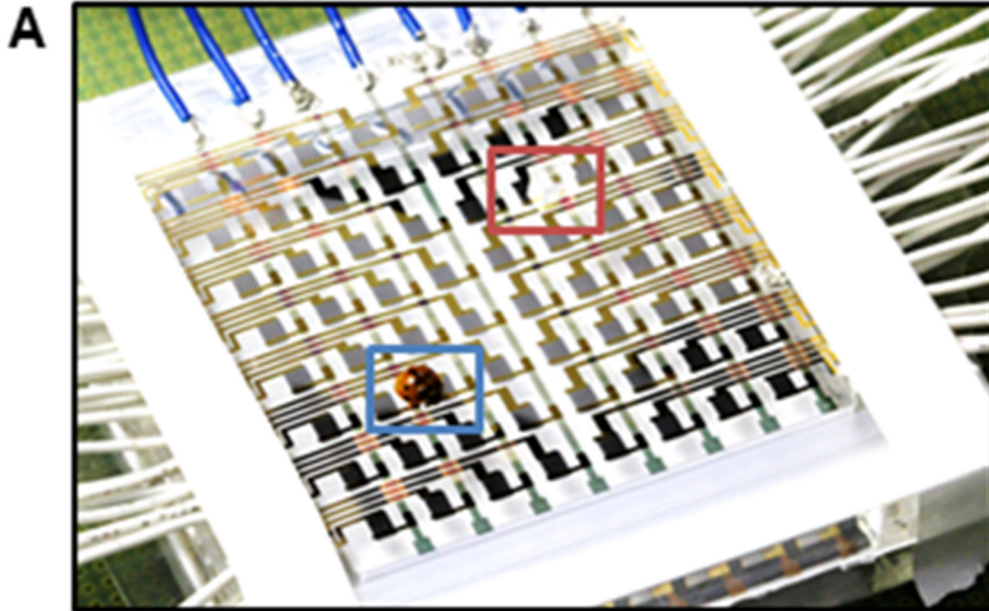


Figure 3-3. Multi-pixel array of the crack sensor. (A) The 8×8 array of the crack sensor applying pressure with a piece of PDMS (red) and vibration and pressure with a flapping ladybug (blue). The overall dimensions of the device are $5 \times 5 \text{ cm}^2$, and the pixel is $2 \times 2 \text{ mm}^2$.

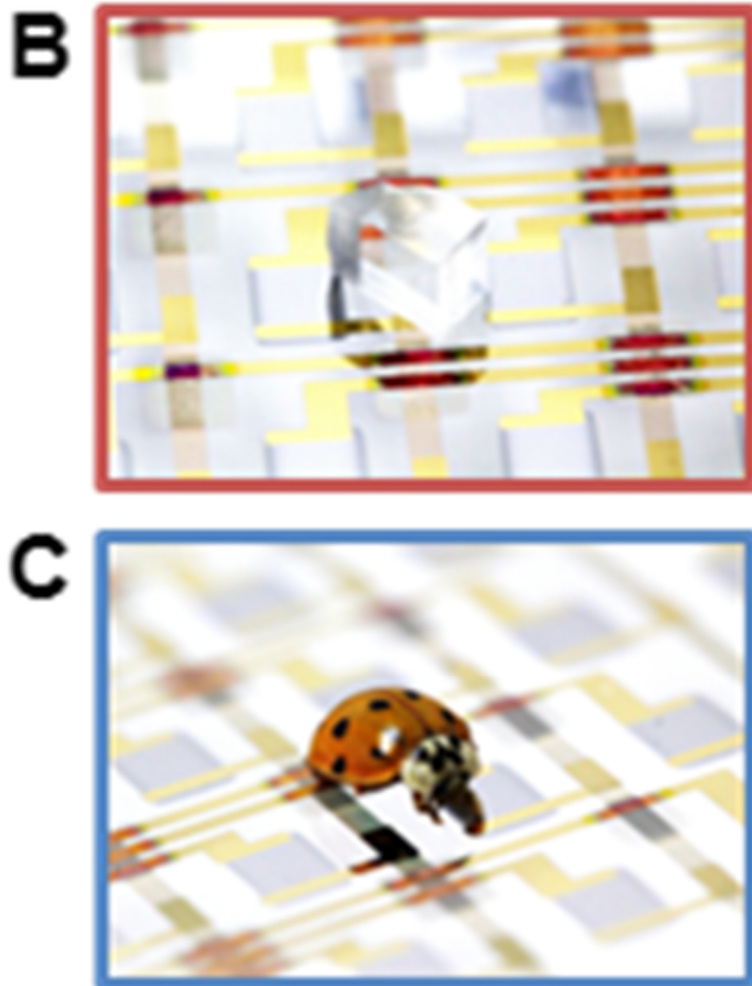


Figure 3-3. (B) A region of the PDMS image for applying pressure. (C) A ladybug image for applying pressure and 0.2 kHz of vibration.

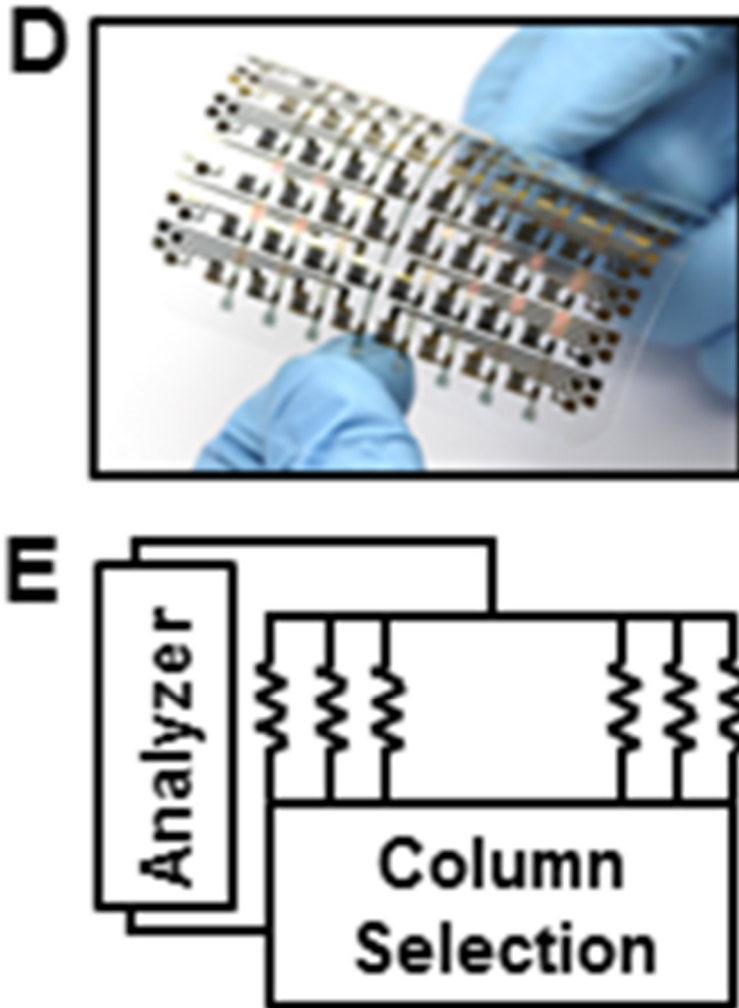


Figure 3-3. (D) Representative image of the crack-based sensor's flexibility. (E) Simple circuit scheme of (A) for multiplexing.

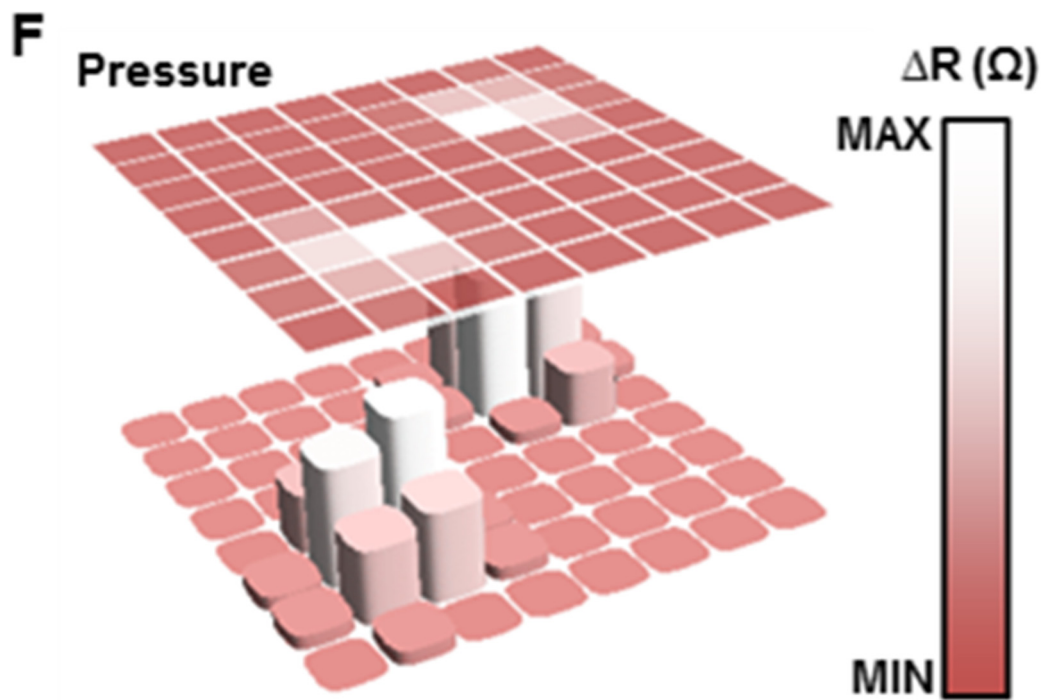


Figure 3-3. (F) Pressure distribution with a piece of PDMS and a non-flapping ladybug.

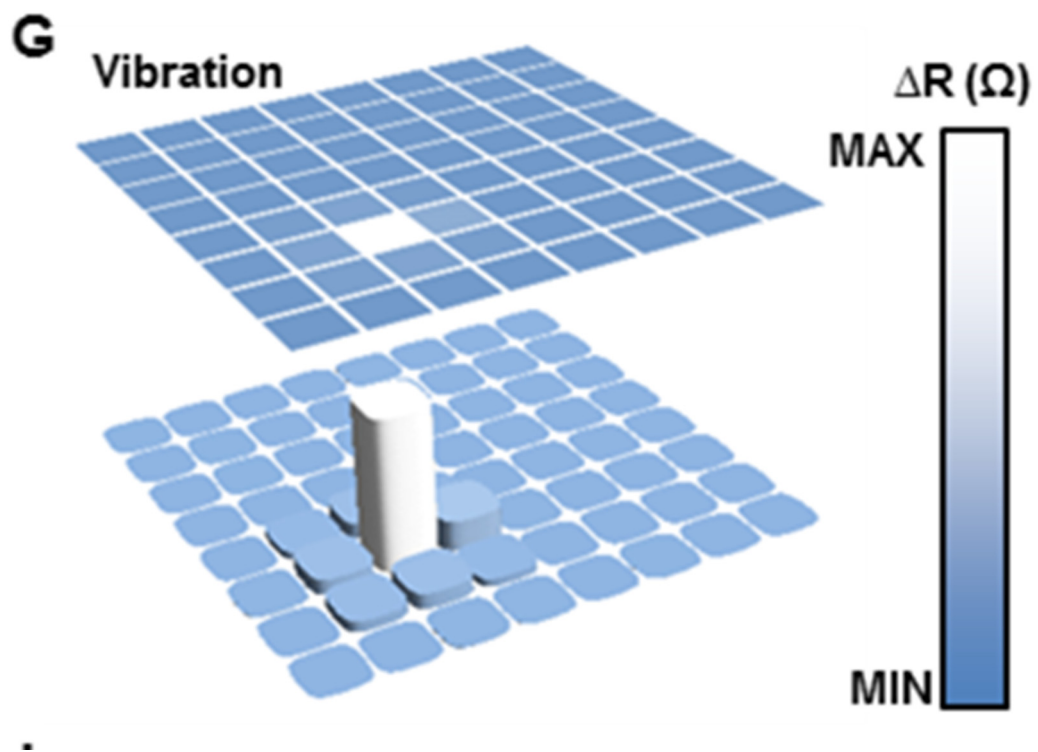


Figure 3-3. (G) Vibration distribution with a piece of PDMS and a flapping ladybug.

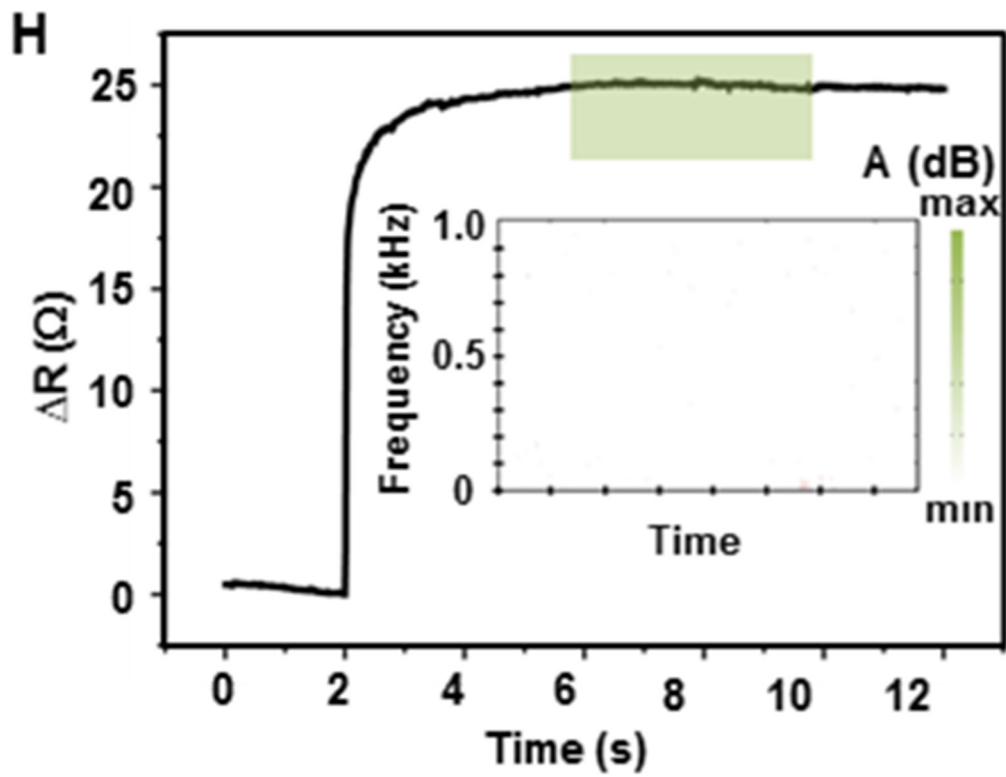


Figure 3-3. (H) Dynamic pressure change of (F). The inset illustrates the lack of vibration frequency obtained from (F).

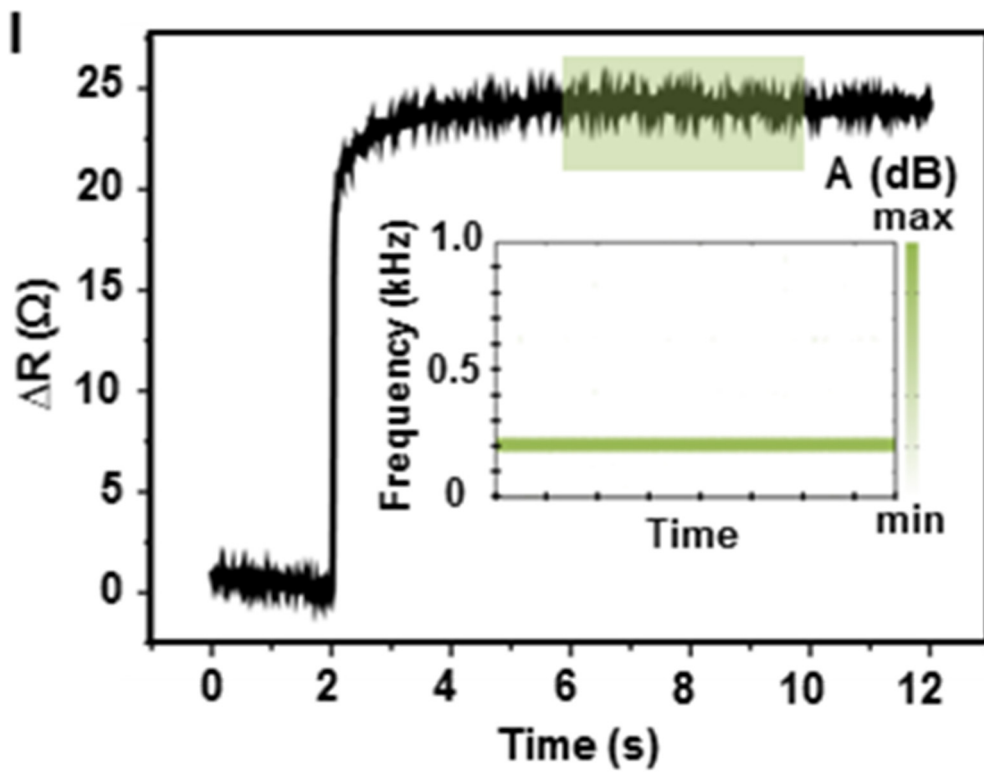


Figure 3-3. (I) Dynamic pressure change with 0.2 kHz vibrations. The inset shows the frequency of 0.2 kHz obtained from (I).

3-5. Versatile applications of the crack sensor

The ultra-mechanosensitive nanoscale crack-based sensor is able to monitor minute sound waves. To demonstrate its performance as a sound monitor, the nanoscale crack-based sensor is attached to the surface of a violin (Figure. 3-4A) and on a neck (Figure. 3-4D). The sensor measures the strings' vibration on the right side of the instrument above the F-hole that transmits the resonance of air to the outside. The measured G-D-A-E string sounds reveal peak signals at different frequencies that correspond with the known frequencies, as shown in Figure 3-4B. Based on the results, 'Salut d'Amour' and 'Scientist' measured by our sensor attached on the violin and speaker, respectively, could be converted as computational codes (Supplementary video file; 'Salut d'Amour'), and the same music was successfully re-played (Supplementary audio file; 'Scientist'). The measured resistance change and real-time peak spectrogram of the signals are shown in the bottom image of Figure 3-4C. The harmonic tone of each note is recorded correctly and well matched. The flexible sensor attached to a human neck can further be utilized as a speech pattern recognition system. The current microphone-based system inevitably hampers the accuracy of speech pattern recognition when the ambient condition is not quiet or multiple sounds are mixed. The system cannot sufficiently filter unnecessary information, in contrast to the human auditory system (known as the 'cocktail party effect'). (see Figure. 3-23) [60] We overcome this cocktail party

problem and successfully filter speech pattern in a noisy environment. Here, 10 speakers are asked to repeat four different words (“go,” “jump,” “shoot,” and “stop”) more than ten times with a microphone and the vibration sensor attached to the subjects’ necks (shown in Figure. 3-4D). The acoustic waveforms and auditory spectrograms of the speakers are analyzed by real-time fast Fourier transform. In silence, the acoustic waveforms (the top part of Figure. 3-4E) and their spectrograms (bottom) with both tools, the crack-based sensor (blue) and the microphone (red), are rather stable and not noisy (Figure. 3-4E). However, in a noisy environment of approximately 92 dB (measured by Type 2250, B&K Inc.; a fire alarm yields approximately 100 dB of noise), the accuracy of the microphone decreases by as much as 28.2%, whereas the crack sensor maintains its accuracy of approximately 97.5% (Figure. 3-4F). Figure 3-4G compares the use of the microphone and crack sensor with (right) and without (left) noise. Furthermore, the accuracy of speech pattern recognition remains over 90% for 10 different people speaking the same set of words with 10 repeats of each word. Details are shown in Figure 3-21, 3-22, and 3-23. To ensure the capability of the speech pattern recognition system as an example of a human-machine interface (HMI), a video game (Super Mario Bros., Nintendo) is played using the same set of words. The character in the game is perfectly controlled by speech commands with a fast response time (< 0.5 s) and high accuracy ($> 95\%$) (Figure. 3-4H). As another example, the crack-based sensor attached on a wrist can also measure a human

sphygmogram (Figure. 3-4I). Figure 3-4J presents heartbeats under two different conditions: normal (approximately 60 beats per min with 100 Pa) and post-running exercise (approximately 100 beats per min at 300-400 Pa) [61]. The signals are successfully monitored in situ and provide crucial heart physiology information, such as the diastolic and systolic movement of the heart (Figure. 3-4K, enlarged image from the gray part in J). For another application, the crack-based sensor is integrated into a microfluidic system to measure the input flow rate. An image and scheme of the sensor embedded into a micro-fluidic system are presented in Figures 3-4L and M. The pressure inside the micro-fluidic channel is higher than that outside, and it varies depending on the flow rate, which can induce a spacer (500- μm -thick PDMS between the channel and device) sagging down and touching the sensor such that the resistance can be varied with the flow rate (Figures. 3-4N and O). The results for the sensing of a sinusoidal/step function force and a 5 μL water droplet are shown in Figure 3-24.



Figure 3-4. Spider-inspired crack-based sensor applications for sound and speech pattern recognition, human physiology monitoring and flow rate indicators. (A) Image of a crack-based sensor attached to a violin for sound wave recognition. The device is placed on the right string above the F-hole of the violin using commercial tape.

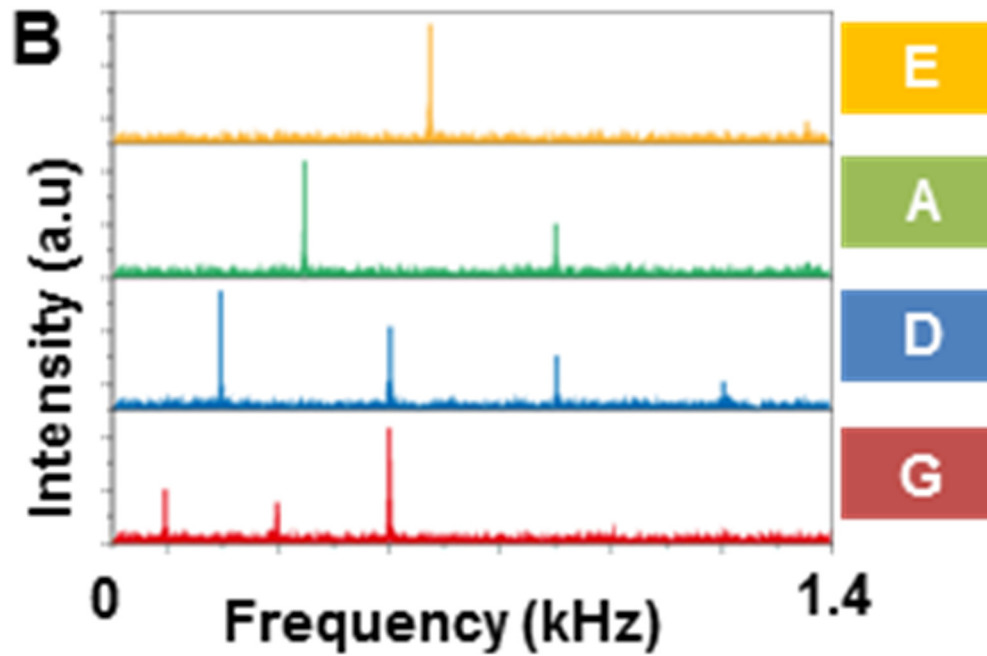


Figure 3-4. (B) E-(yellow), A-(green), D-(blue), and G-(red) open string (that is, a string played without any finger stopping it) sounds produce different wave functions that we collected using the crack sensor. The E-, A-, D-, and G-open strings have fundamental frequencies of 659, 440, 294 and 196 Hz, respectively, as measured by the sensor.

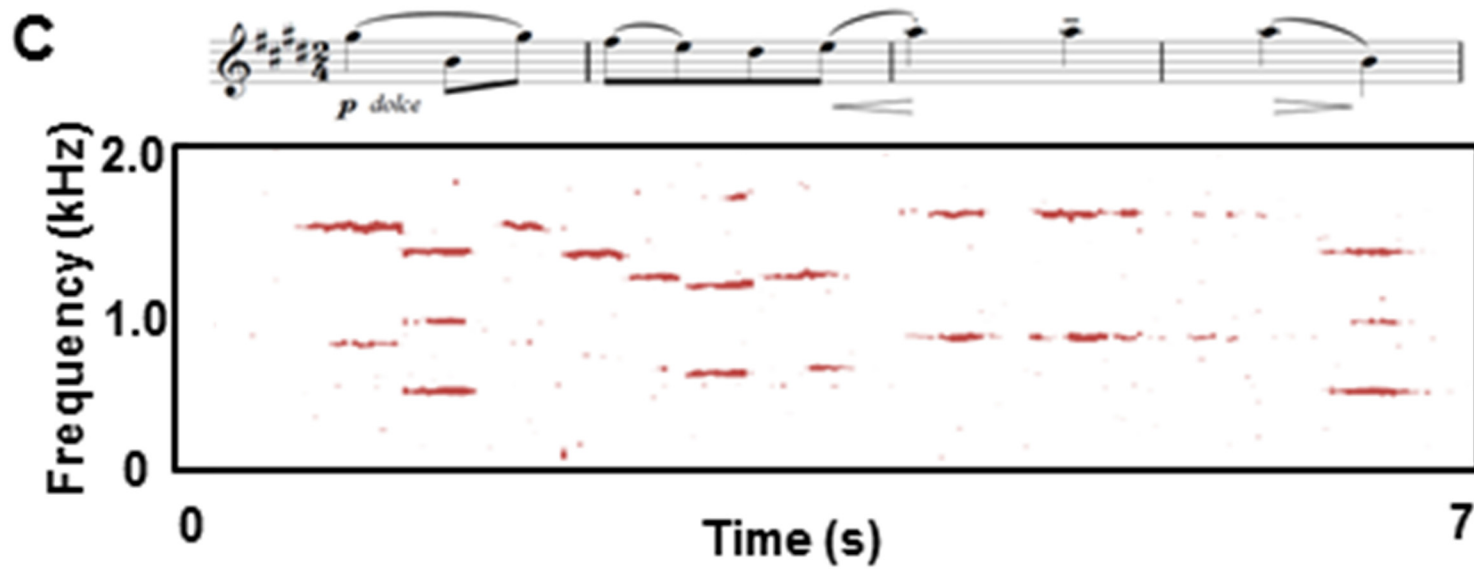


Figure 3-4. (C) The measured sound waves of music playing (Salut d'Amour). The replayed music by electrical recording and computational converting is presented in the Supplementary video file.



Figure 3-4. (D) An image of the sensor attached on a neck for human speech recording.

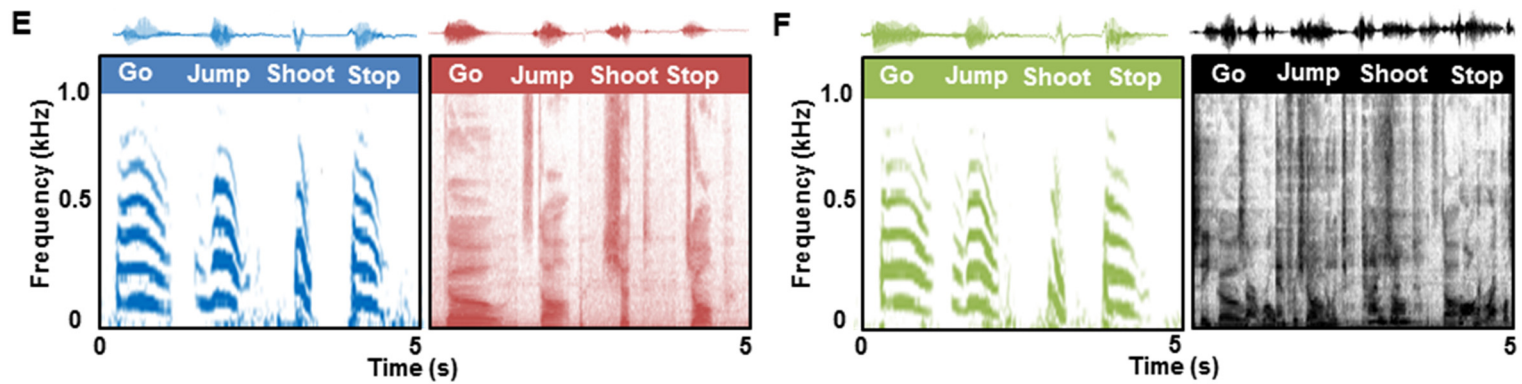


Figure 3-4. (E, F) Comparisons of the acoustic waveform and auditory spectrogram changes measured by electrical resistance using the crack sensor (left image of (E) and (F)) and microphone (right images) in quiet (E) and noisy (F) environments (approximately 92 dB is applied in the noisy environment). All of the signals are measured when a speaker pronounces “go,” “jump,” “shoot,” and “stop.” The signals from both the crack sensor and microphone are recorded clearly without noise (E). The signal from the microphone is not clear with the approximately 92 dB of noise (right image of (F)), whereas our crack sensor maintains its high level of accuracy under the same noise level (left image of (F)).

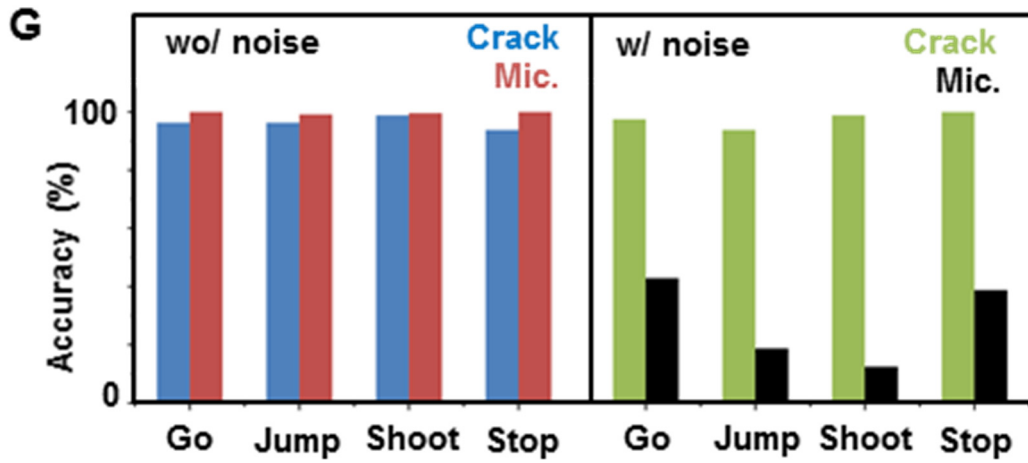


Figure 3-4. (G) The sensing accuracy comparisons (over 400 speeches with one person) between the speech pattern recognition results with a crack-based sensor and microphone are shown. An accuracy of 97.5% is obtained from the crack sensor even with noise.

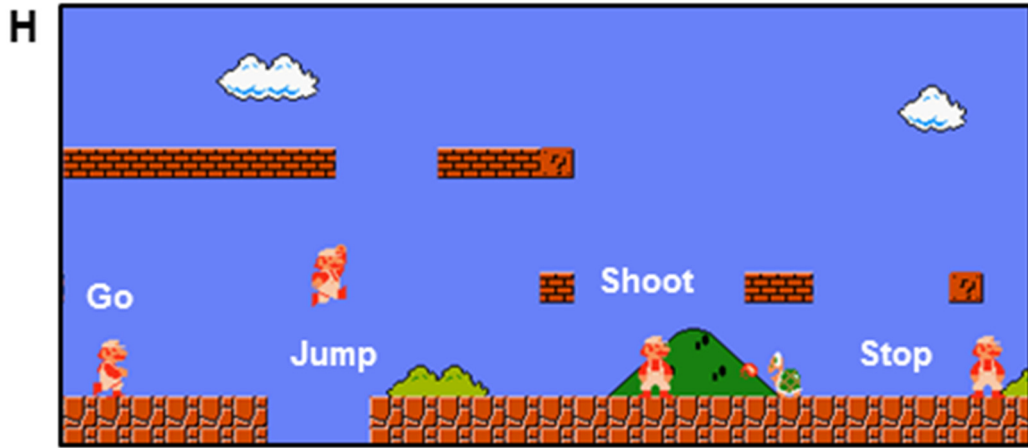


Figure 3-4. (H) Video game (Super Mario Bros., Nintendo) demonstration using four different speech recognitions.

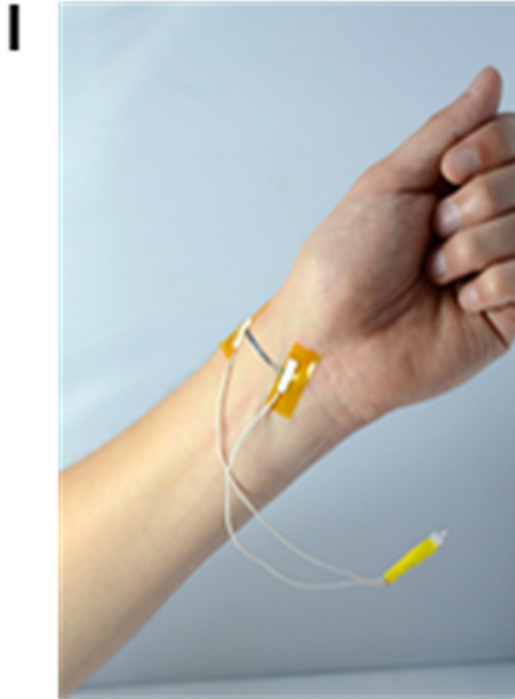


Figure 3-4. (I) Image of the crack sensor attached on a wrist for sphygmography.

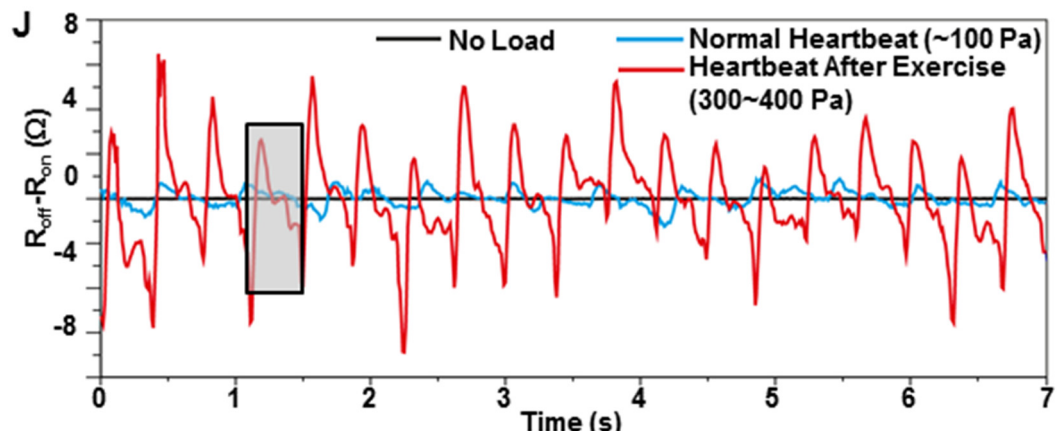


Figure 3-4. (J) Measured characteristics of the resistance difference with the crack-based sensor attached on a wrist. The detailed variations of the pulses for the reference (no load; black), normal heart beating (approximately 100 Pa; sky blue), and heart beating after running (300-400 Pa; red) are clearly observed.

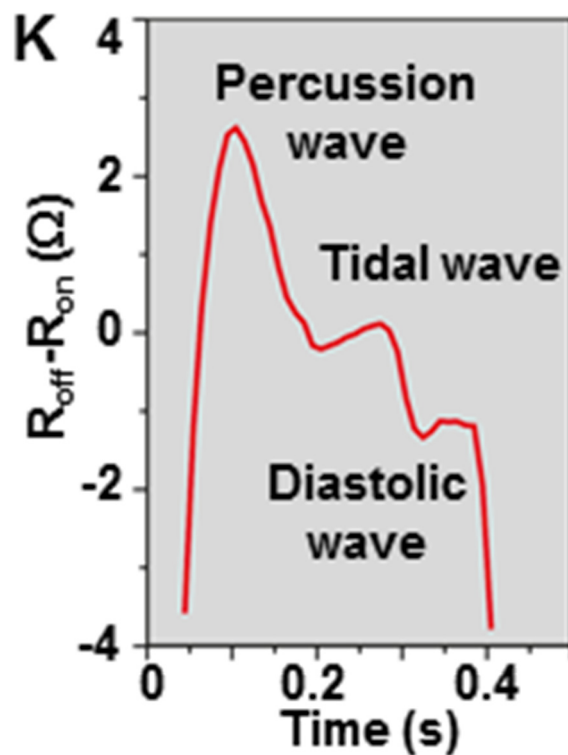


Figure 3-4. (K) Representative characteristic of the gray region from (J) showing the typical characteristics of the wrist pulse including percussion, tidal, and diastolic waves, which can monitor human's systolic/diastolic blood pressure, heart rate, and ventricular blood pressure.

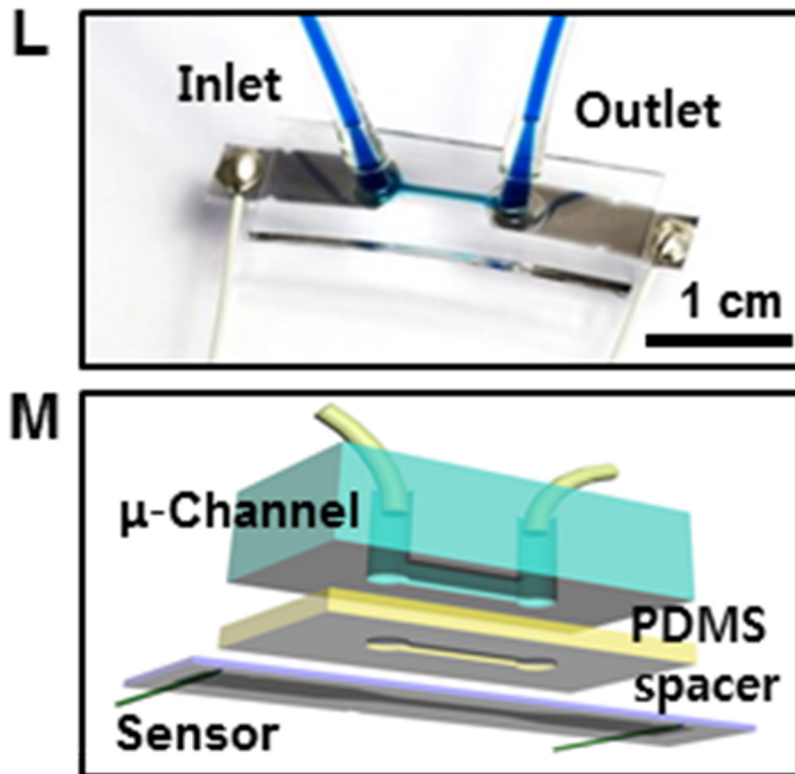


Figure 3-4. (L) Liquid flow rate measurement with the crack sensor in a microfluidic channel. (M) Schematic of stack information in the sensing system. Inlet and outlet flow with various flow rates (flow rate of 5-9 ml/min in the microfluidic channel with a width of 100 μm , height of 100 μm , and length of 10 mm) on a 100- μm -thick spacer (PDMS) to prevent electrical failure.

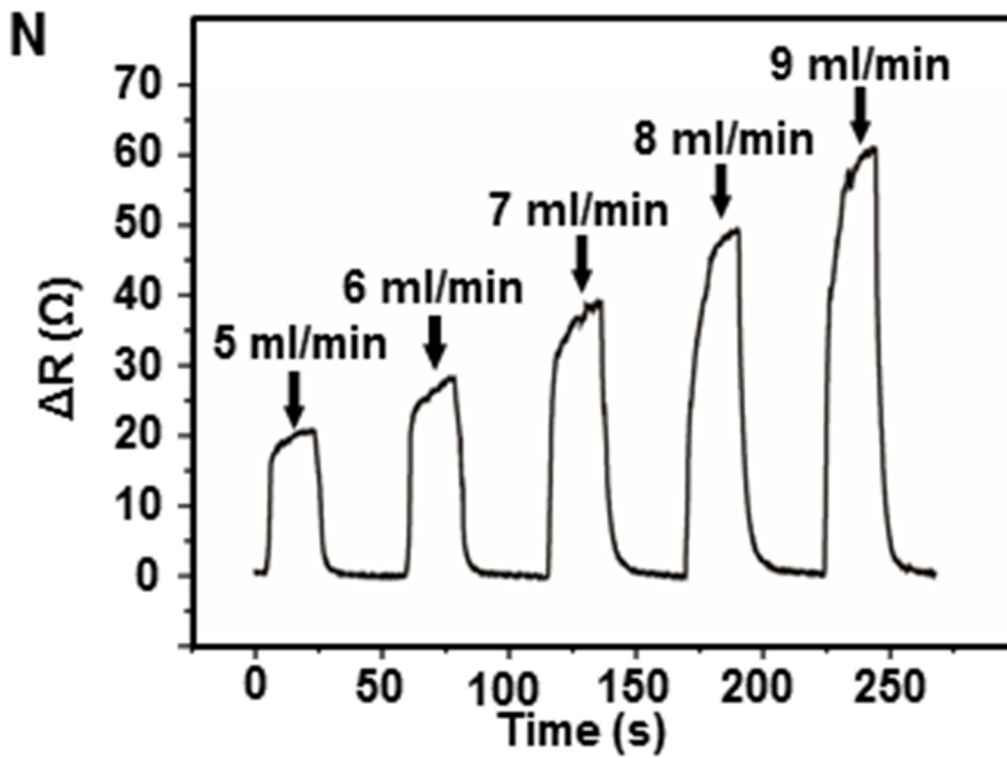


Figure 3-4. (N) Resistance changes at various flow rates as a function of time measured using the crack sensor encapsulated by a PDMS spacer in a microchannel.

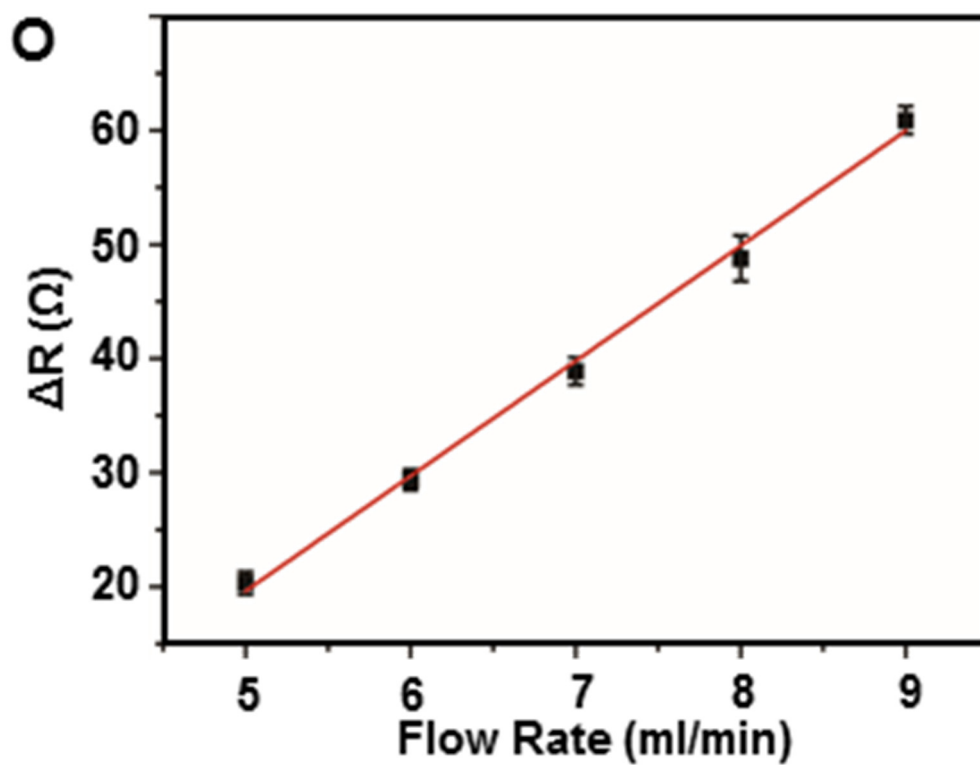


Figure 3-4. (O) Linear change in resistance as a function of flow rate.

3-6. Summary

In conclusion, we mimicked the highly sensitive and complicated slit organ of a spider's strain detector to design a novel, simplified, ultra-mechanosensitive nanoscale crack-based sensor. We demonstrated that our spider-inspired sensor exhibits the highest gauge factor of a sensor achieved to date and can be applied as a multifunctional sensor for highly selective speech pattern recognition, human physiology monitoring and external force and vibration detection. We studied the underlying physical mechanism and observed intriguing the disconnection/reconnection processes of the crack junctions, which enabled the ultra-high sensitivity of the device. We developed a theory describing electrical conductance through crack junctions when strain is applied, which is consistent with the experiments. Moreover, the reproducibility, flexibility and large area coverage with multiplexing permit the integration of the device on curvilinear human skin with more advanced tools.

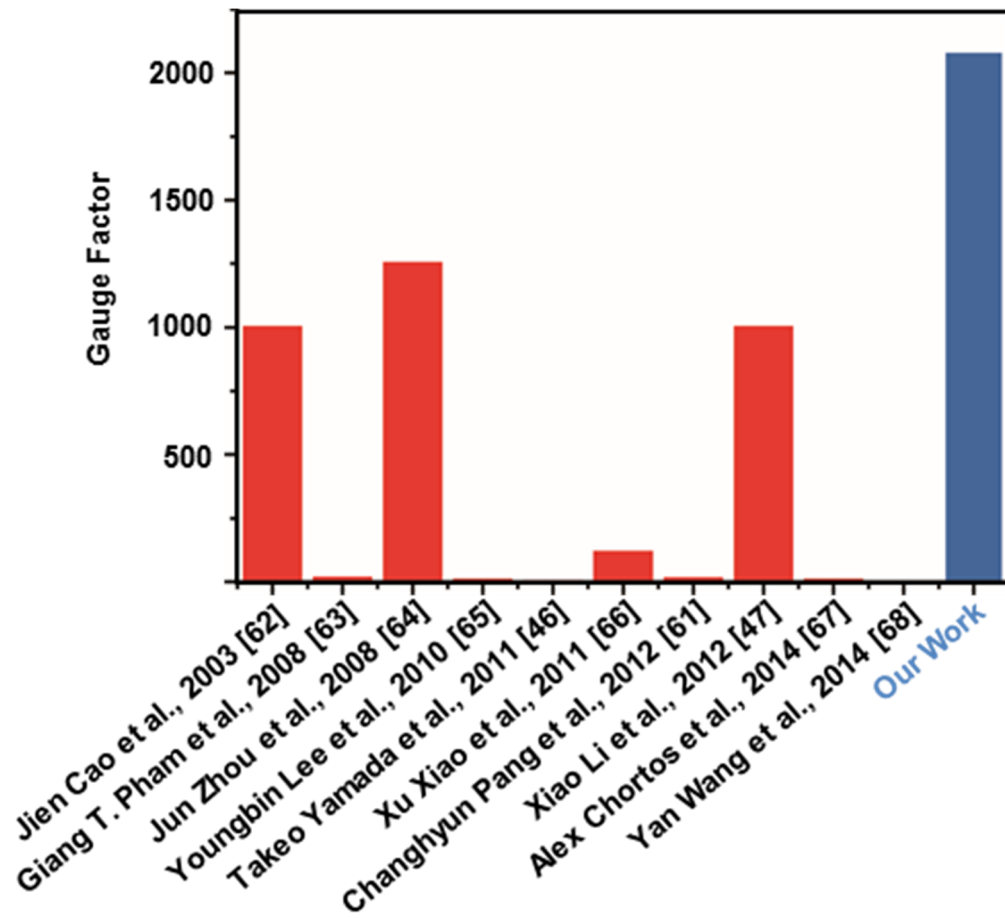


Figure 3-5. Comparison of the present sensor gauge factor with previous studies. Gauge factors of sensors reported at 2 % applied strain are shown (red). The gauge factor of the present spider-inspired crack sensor is 2079 (blue).

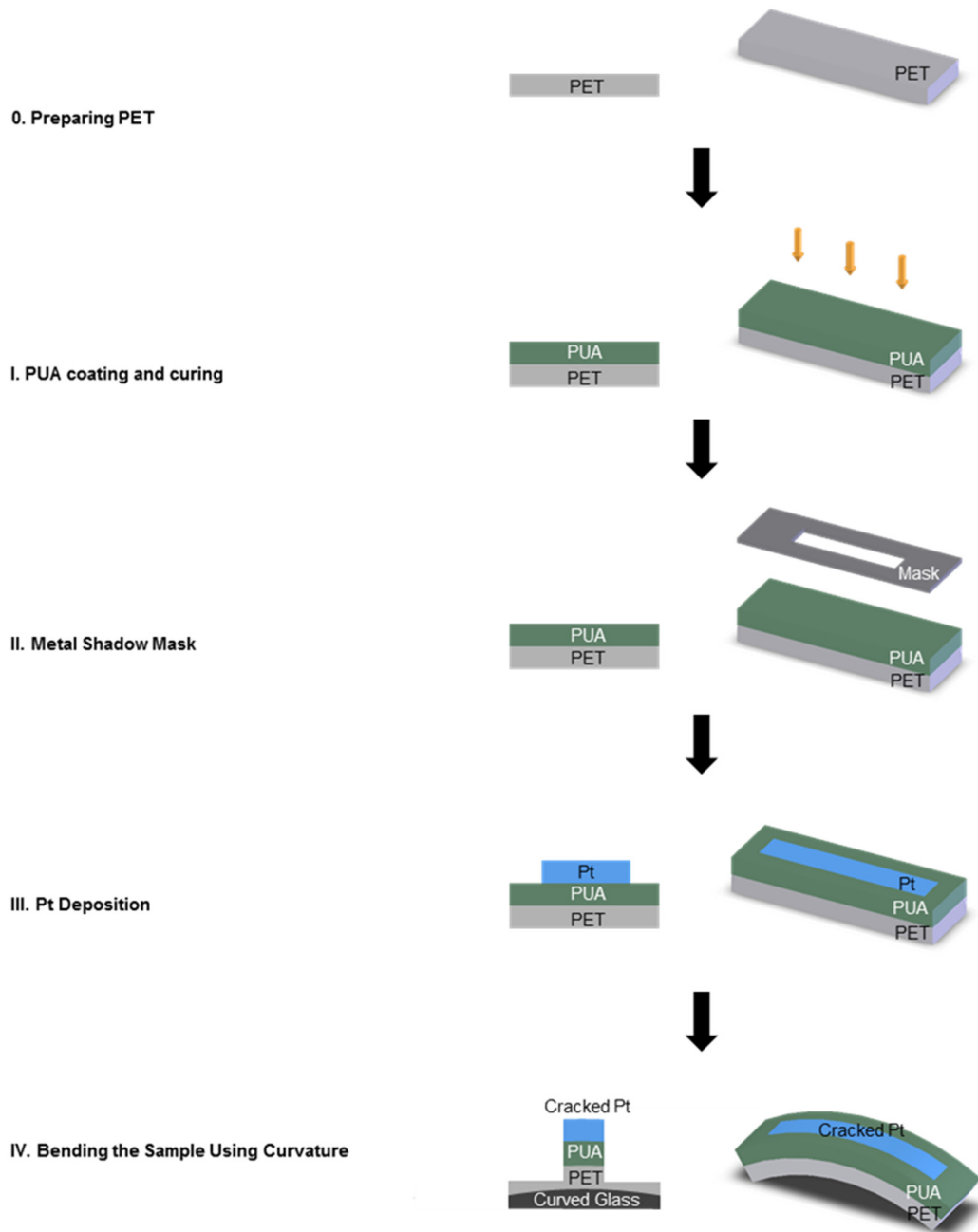


Figure 3-6. Overall fabrication procedure for crack based sensor.

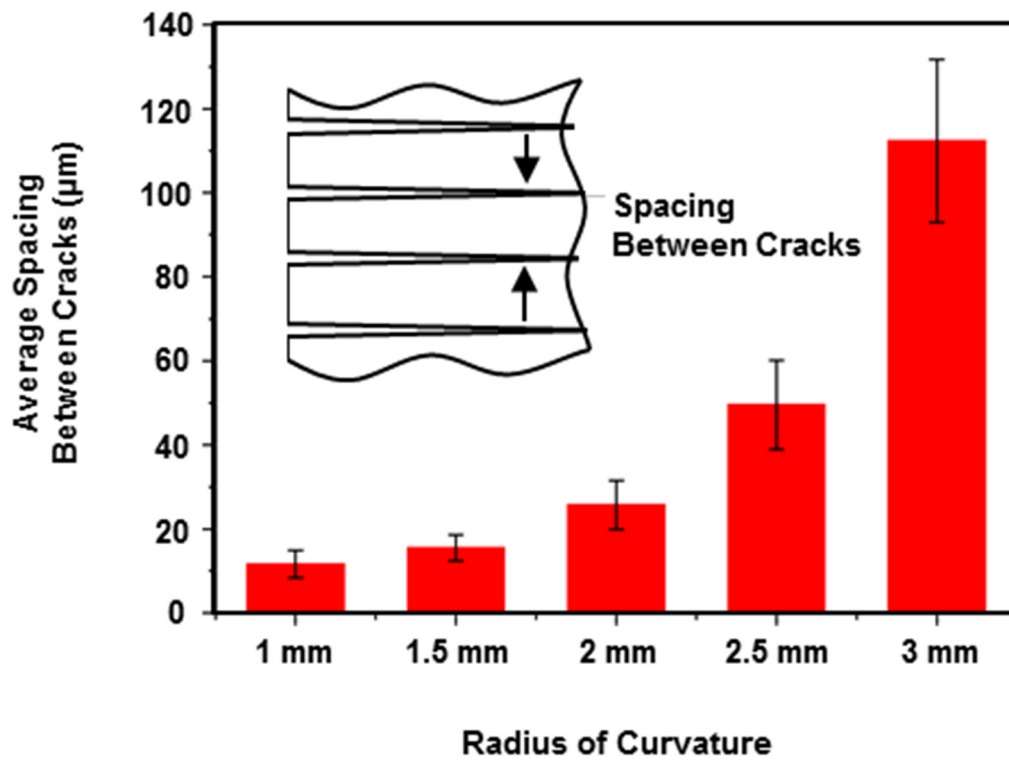


Figure 3-7. Average spacing between two adjacent cracks fabricated by different bending radius of curvatures, ranging from 1 mm to 3 mm. Average spacing between two adjacent cracks are shown to be controlled by using different radius of curvature bending.

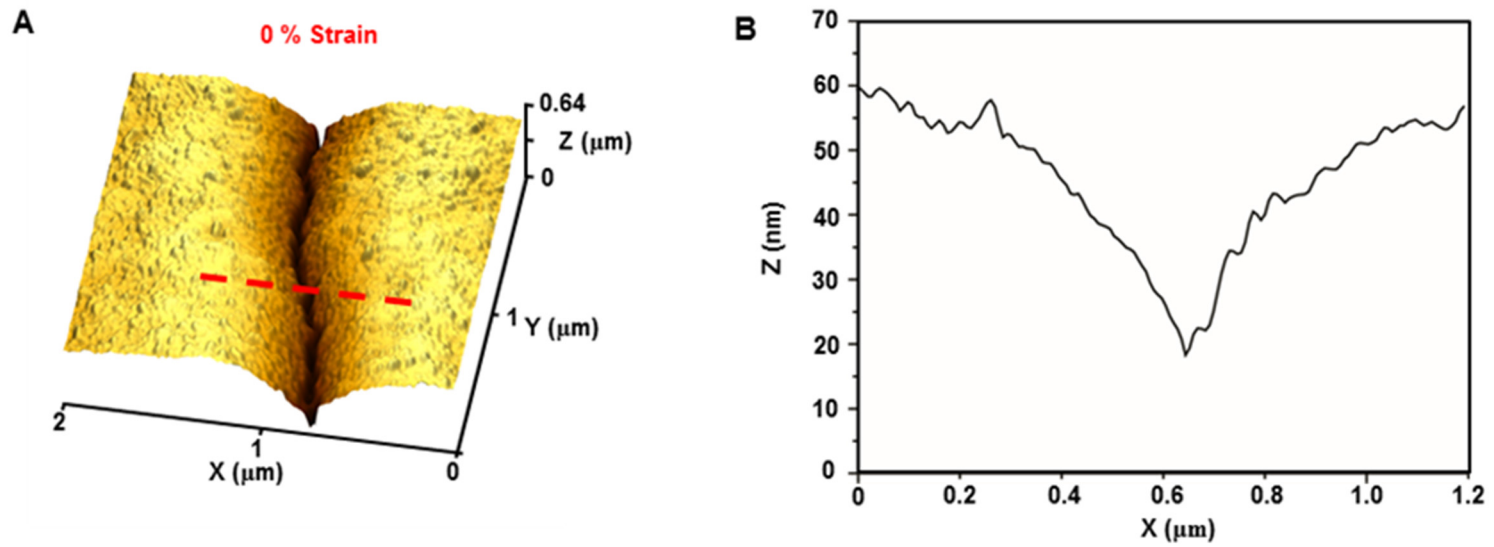


Figure 3-8. Atomic force microscopy (AFM) results on crack surface with applied various strains. (A) 3D image of crack within 0 % strain. (B) Profile of red dashed line in (A).

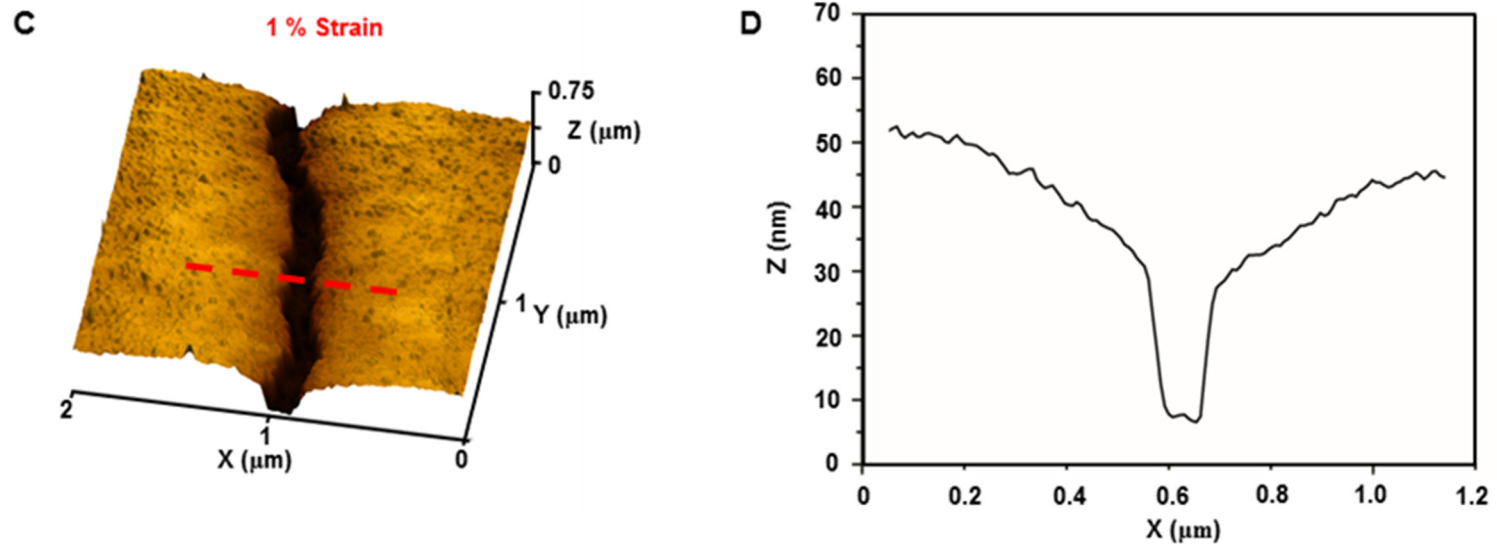


Figure 3-8. (C) 3D image of crack within 1 % strain. (D) Profile of red dashed line of (C) indicating the crack depth to be about 40-50 nm.

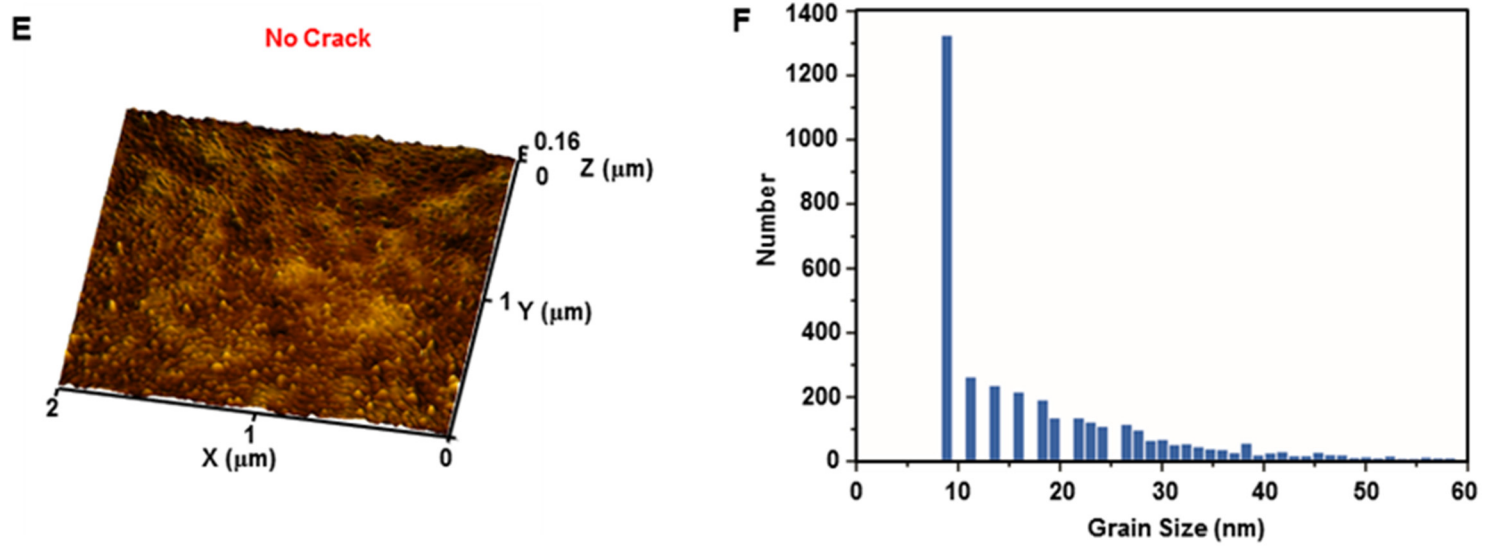


Figure 3-8. (E) 3D image of non-crack surface. (F) Metal grain size distribution obtained from (E)

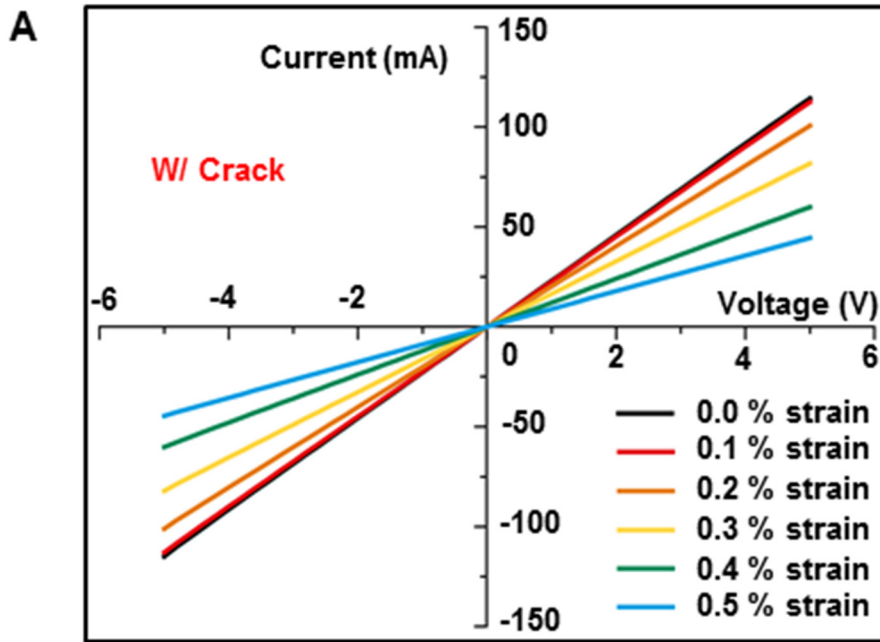


Figure 3-9. Current (I)-voltage (V) characteristic comparison between samples with cracks (fabricated by 1 mm bending) (A) and without crack (B). (A) I-V results applied various strains on crack based sensor. Large variations of electrical resistance against applied strains are found.

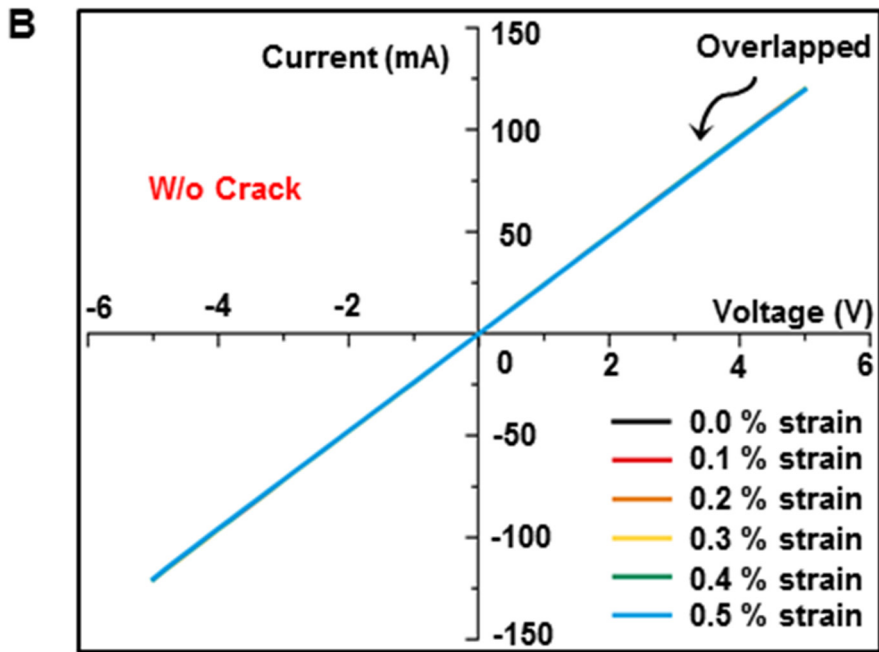


Figure 3-9. (B) I-V results applied various strains on non-cracked metal film. Minor variations of electrical resistance (all graphs are overlapped.) against applied strains are found. Less than 0.5 % applied stains cannot induce electrical resistance change for this non-crack bare Pt film case.

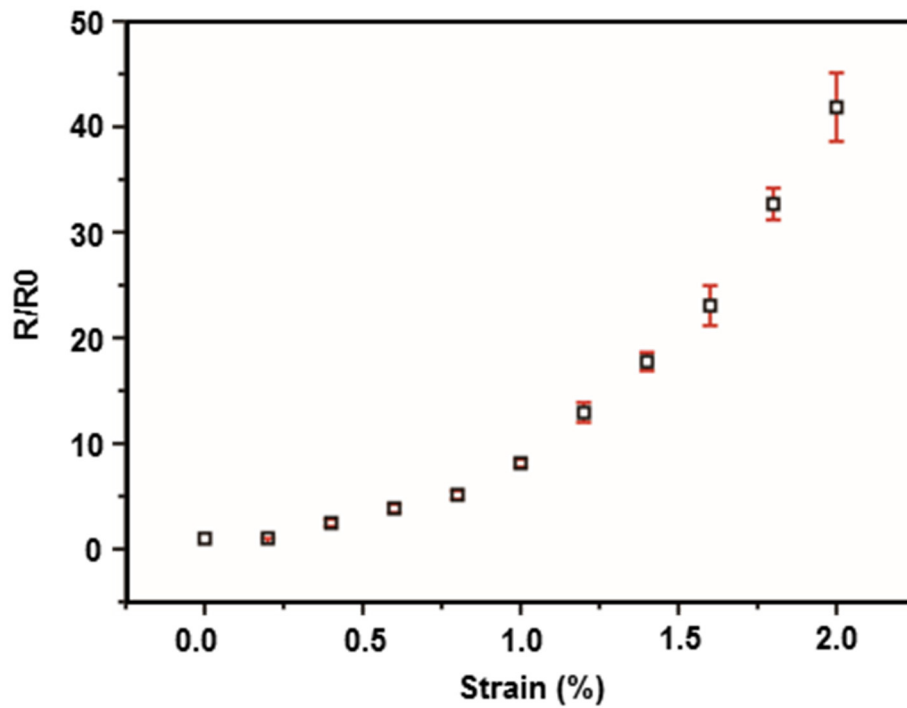


Figure 3-10. Reproducible results obtained from five crack based sensors fabricated by 1 mm curvature bending.

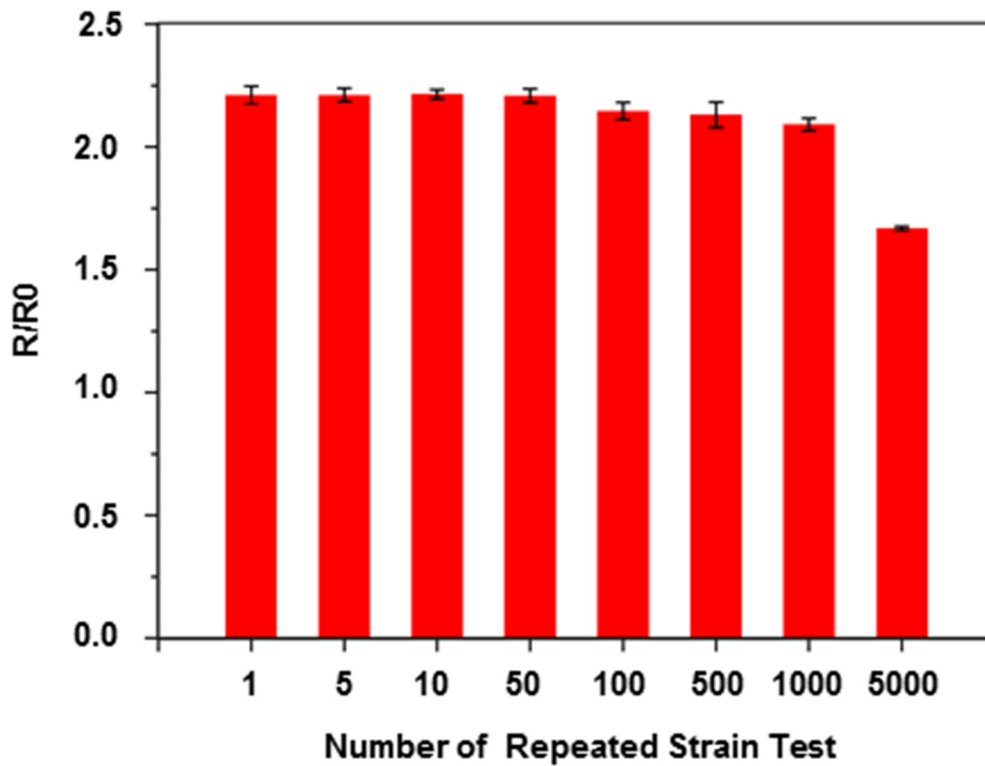


Figure 3-11. Multiple-cycle tests (<5,000 cycles) with repeated loading–unloading of strain in the range of 0 – 0.5 % using 1 mm radius of curvature crack based sensor. The crack based sensor is shown to be reliable under a few thousand times strain loading.

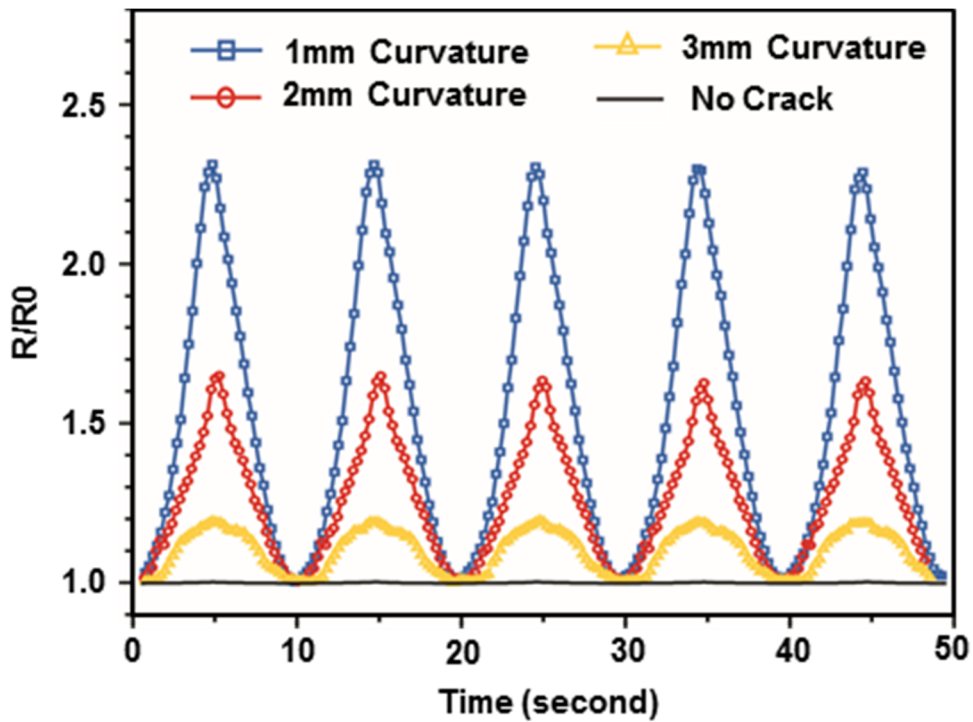


Figure 3-12. Sensitivity (resistance changes) comparison at applied 0.5 % strain using sensors made with difference curvature bending. Sensitivity (resistance changes) is shown to be controllable by changing crack density made by bending with different curvature. Sensitivities of samples made by using different curvature bending (blue – 1mm; red – 2mm; yellow – 3mm) are remarkably higher than the one without crack (black curve).

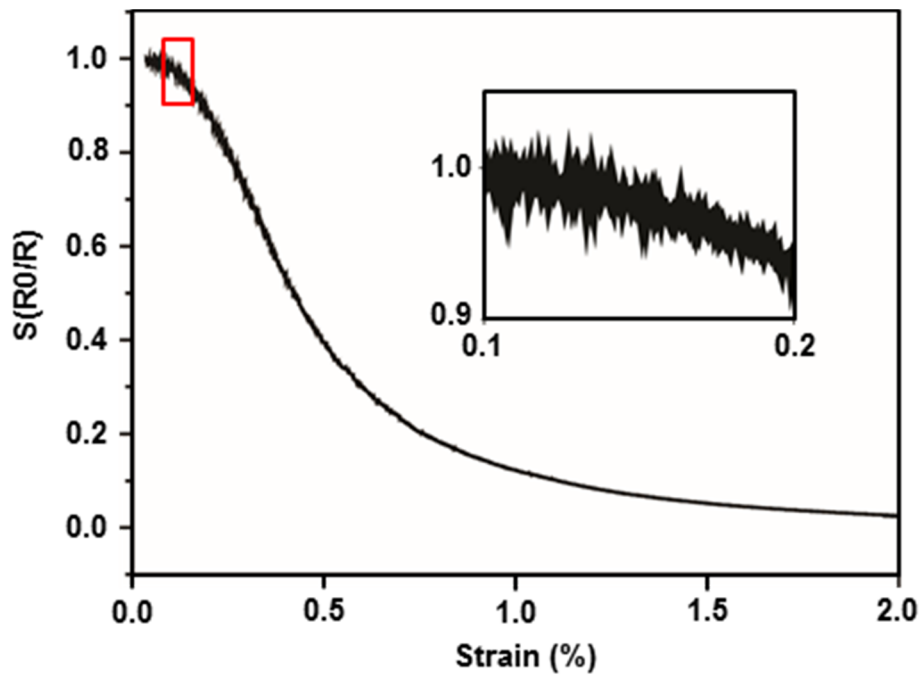


Figure 3-13. S (conductance) curve revealing fluctuations. The variation of $S=R_0/R$ for crack based sensor fabricated by 1 mm radius of curvature is shown as strain is applied. Inset shows the enlarged view in red square revealing a large fluctuation of S.

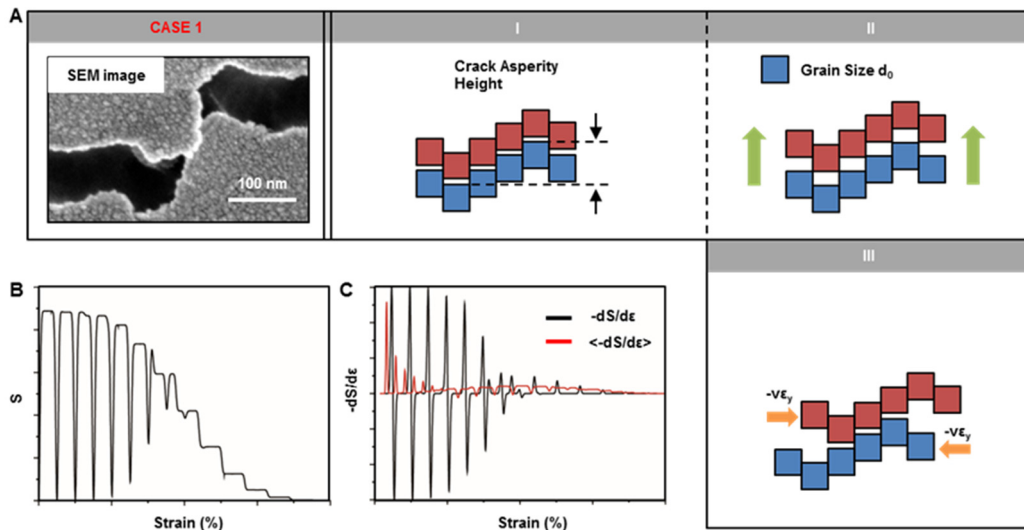


Figure 3-14. An illustrative model conductance with disconnection/reconnection spikes at lower strain that closely simulates the experimental derivative and averaged derivative curves in Figure. 3-2D and E. (A) The real crack image is on the left. The schematic of creeping motion of the crack lips given in the following boxes illustrates the corresponding disconnection/reconnection events with spikes down and up in the model conductance curve, shown in (B). (C) The negative derivative of the model curve from (B) (black) together with the averaged one (red). All model curves in (C) closely mimic experimental Figure. 3-2D and E from the main text, respectively.

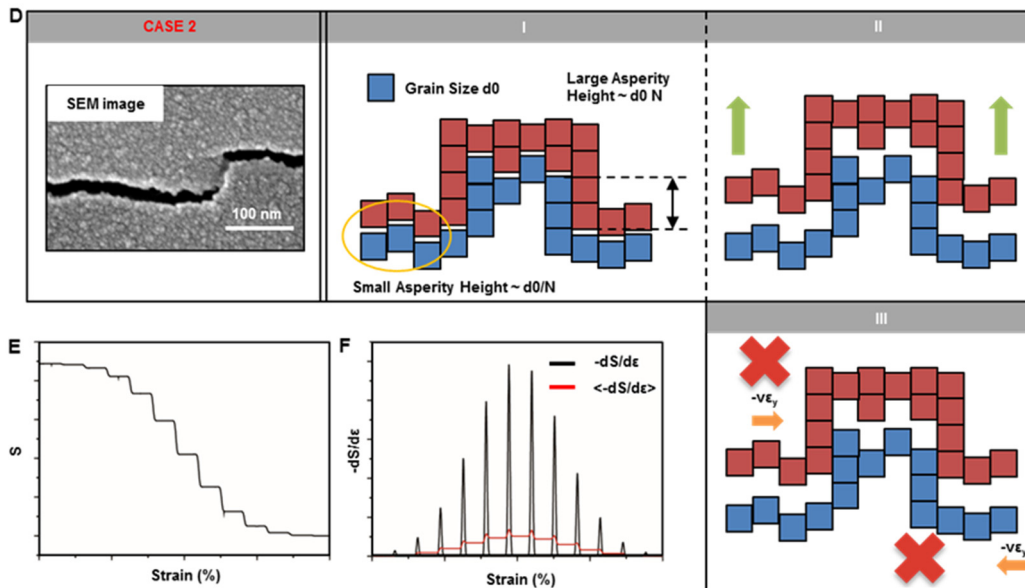


Figure 3-14. (D) The real crack image at larger strains is on the left. A maximum simplified schematic of crack lips ignoring the creeping motion and reconnection events is given in the following boxes. The model grasps the essence of the conductance stepwise reduction with the increase of strain due to disconnection of the contacts. The orange ellipse encompasses the small asperity “staircase” which is statistically scale invariant to the large scale “staircase” on the right. **(E)** A simplified model conductance ignoring the spikes of reconnection. **(F)** The negative derivative of (E) (black) together with the averaged one (red).

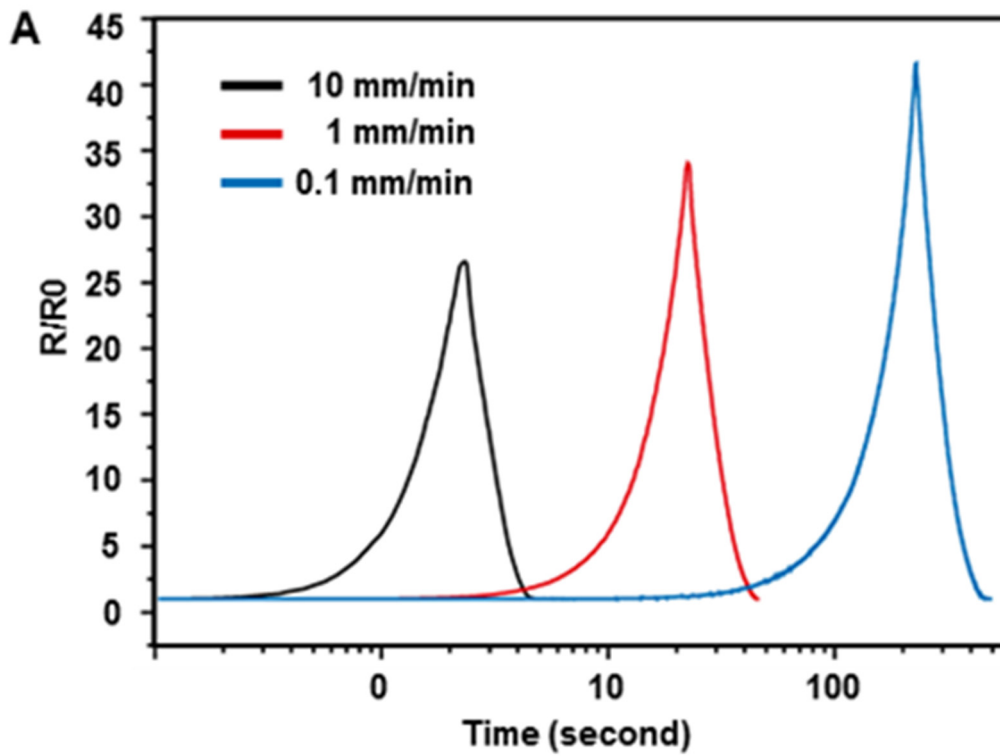


Figure 3-15. Dynamic motion test with the crack based sensor fabricated by 1 mm radius of bending curvature. (A) Sensitivity change of crack sensor by increasing the sweep rate.

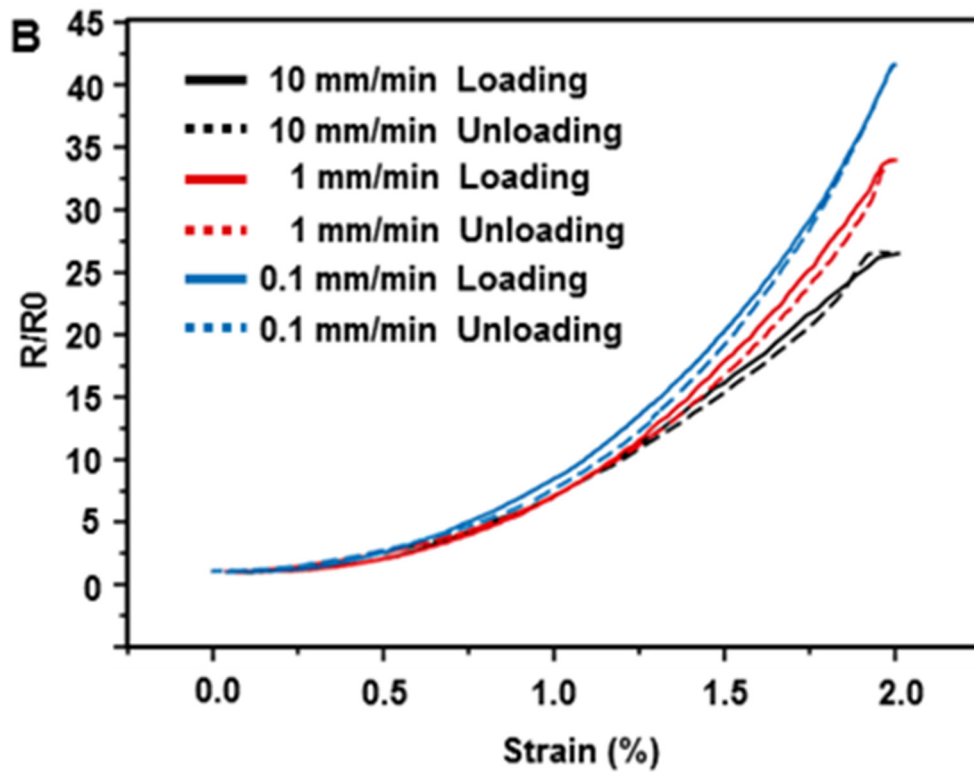


Figure 3-15. (B) Hysteresis test about loading and unloading (solid line - loading; dashed line - unloading).

Although the hysteresis remains negligible for very different sweep rates, the resistance curves, normalized to the initial resistance grow somewhat lower at higher sweep rates. This behavior is due to the stress relaxation time that should pass before the initial resistance diminishes to its minimal value at the slowest sweep rate of 0.1 mm/min, therefore, being the resistance divided by this minimal value, the normalized resistance for 0.1 mm/min becomes the highest.

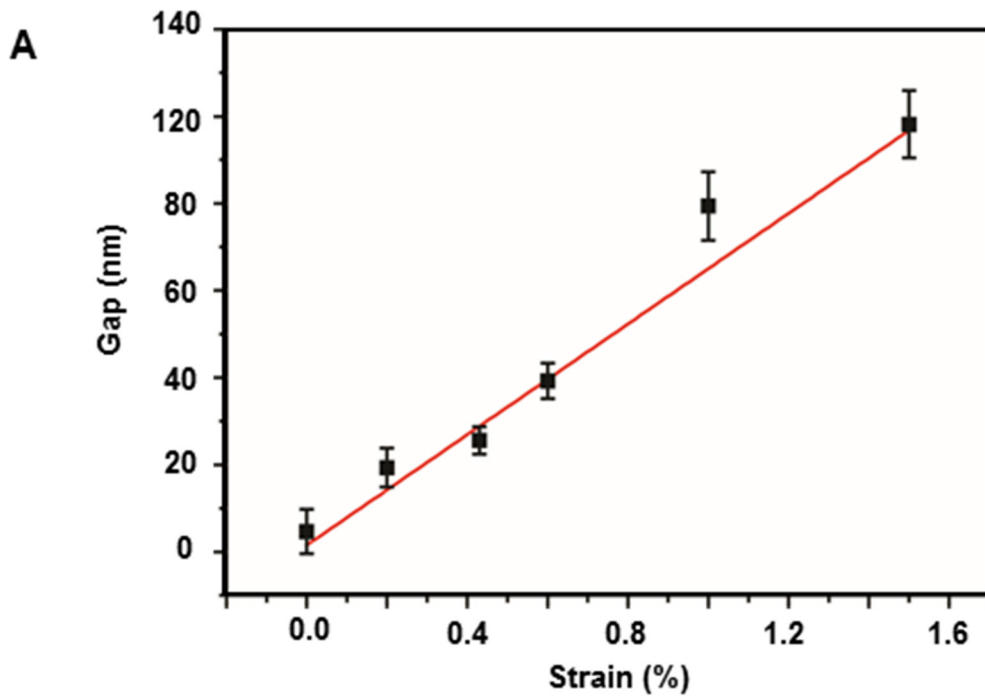


Figure 3-16. Crack gap analysis in several applied strains via SEM results (with 30 samples). (A) Crack gap width variation vs. strain (black squares) and the fitting straight line (red). Gap analysis is performed by imaging processing software, “Image J”.

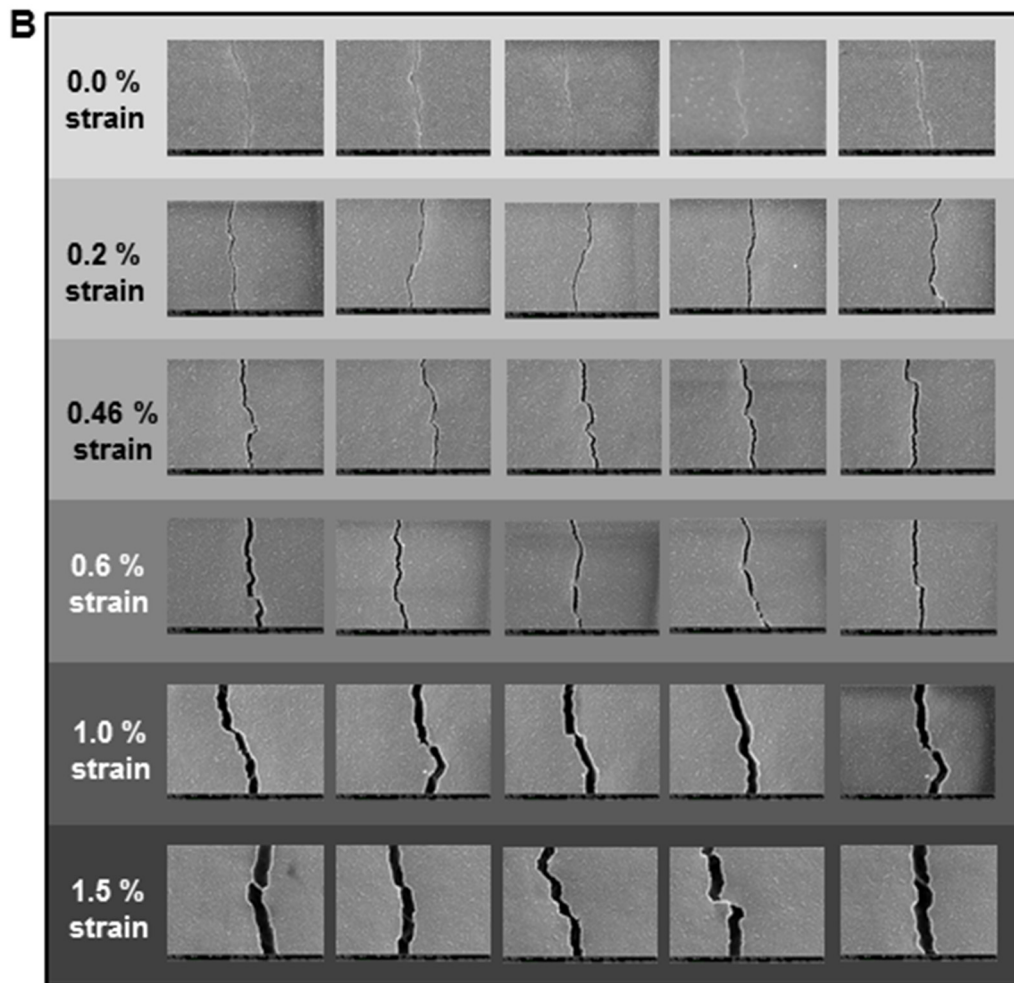


Figure 3-16. (B) Representative SEM images used for the crack gap width determination.

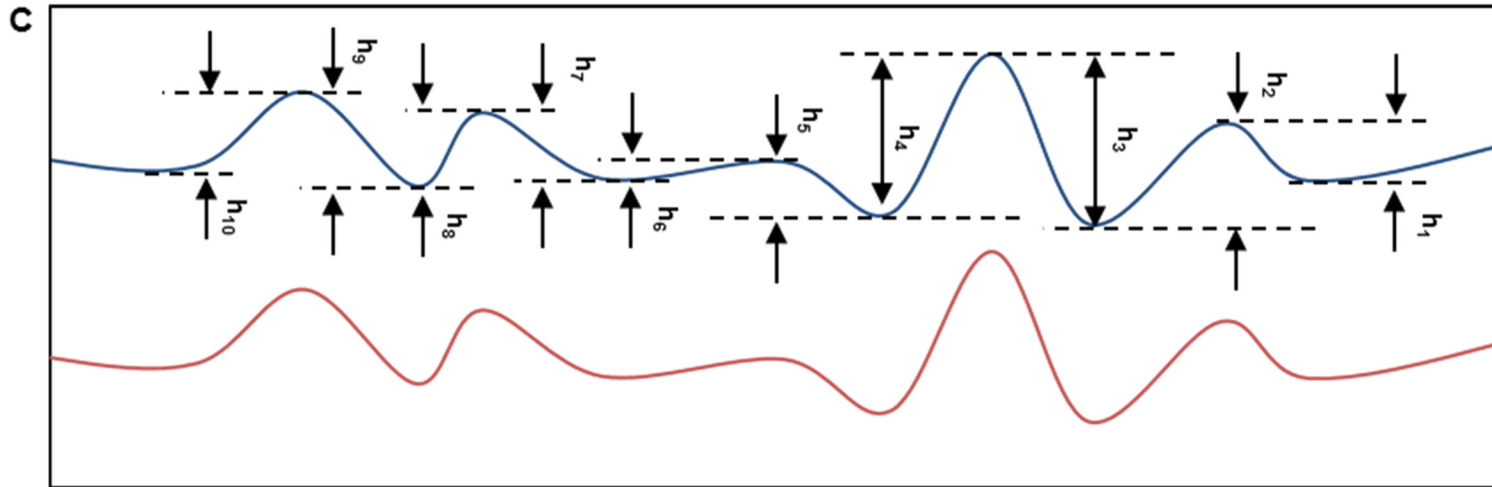


Figure 3-16. (C) The schematic of the crack lip asperity for acquiring the statistics of the contact step heights. The heights are defined as the distance between the nearest and extreme in the strain direction.

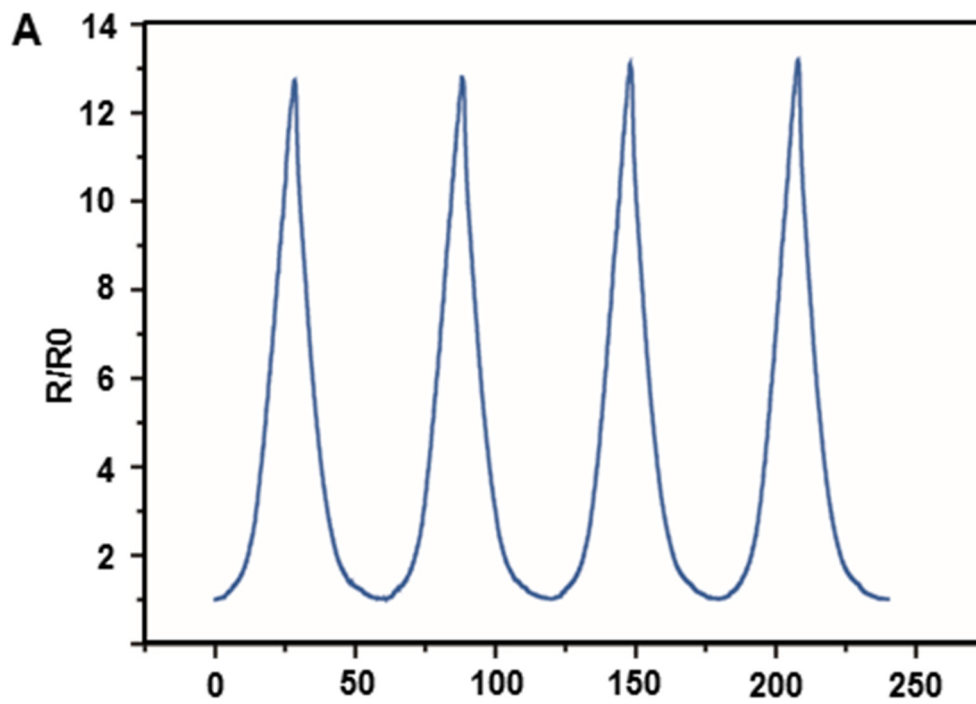


Figure 3-17. Additional tensile test of the crack sensor with 100 nm thickness Pt film. (A) 2 % cyclic tensile test at 0.1 mm/min.

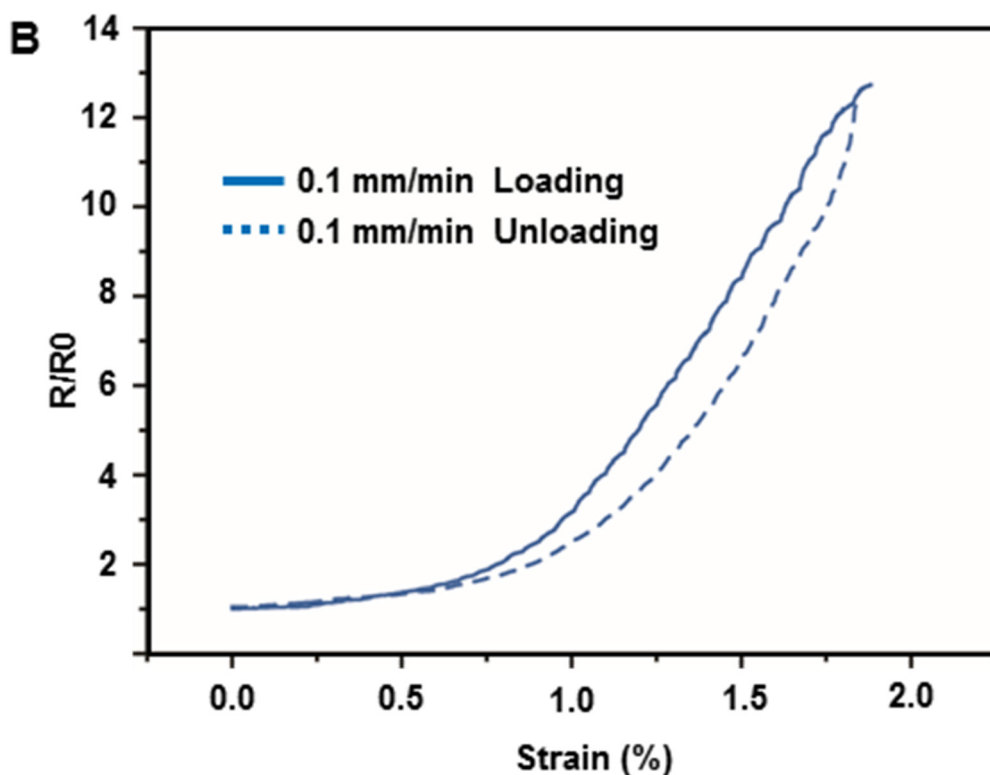


Figure 3-17. (B) Hysteresis test about loading and unloading (solid line - loading; dashed line - unloading).

Even at the slowest sweep rate of 0.1 mm/min the hysteresis persists because of participation of mode 2 (in fracture mechanics mode 2 is characterized by a shear stress acting parallel to the plane of the crack and perpendicular to the crack front) [59] in sliding crack configuration distortion that supports (via stronger mechanical stress for the thicker film) earlier snapping of the contact (larger resistance) and sooner contact recovery (lower resistance) during unloading. Therefore, for this film of 100 nm hysteresis loops are clockwise.

C

Pt thickness	Gauge factor (2% strain)	Ultimate tensile strength (MPa)
20 nm	2079.23	125-165
100 nm	602.80	

Figure 3-17. (C) Gauge factor comparison with different Pt film thickness.

Note that the magnitude of the normalized resistance at 2% strain is nearly four times lower than for a 20 nm Pt film.

This fact indicates keeping a better contact between the thicker lips of the crack in a 100 nm thickness Pt film as would be expected for stronger pressing forces in the thicker film.

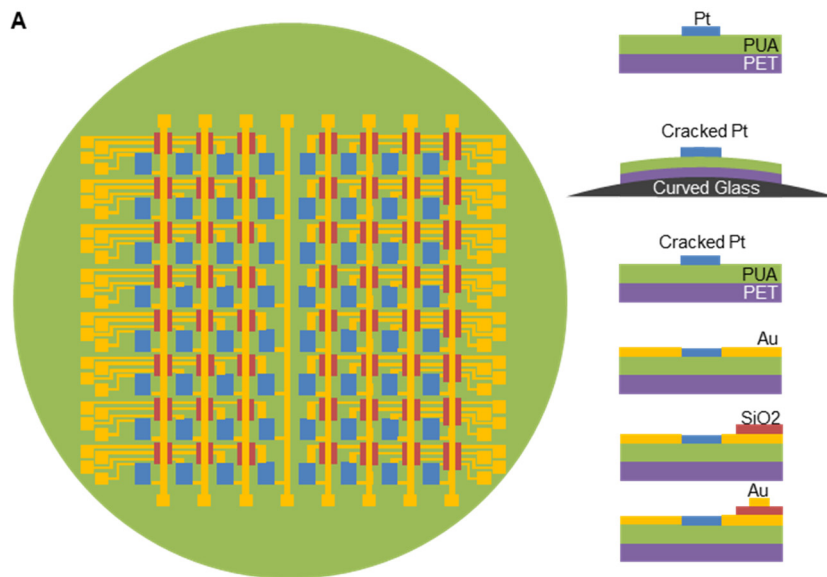


Figure 3-18. Fabrication procedure and image for multiplexing array sensor.

(A) Illustration images of each processing steps.

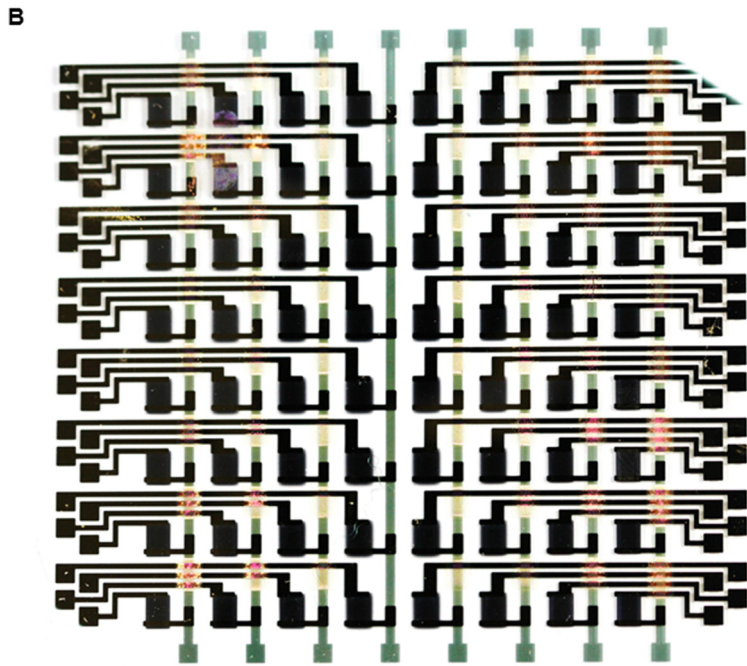


Figure 3-18. (B) Photograph image of the 8×8 multiplex sensor.

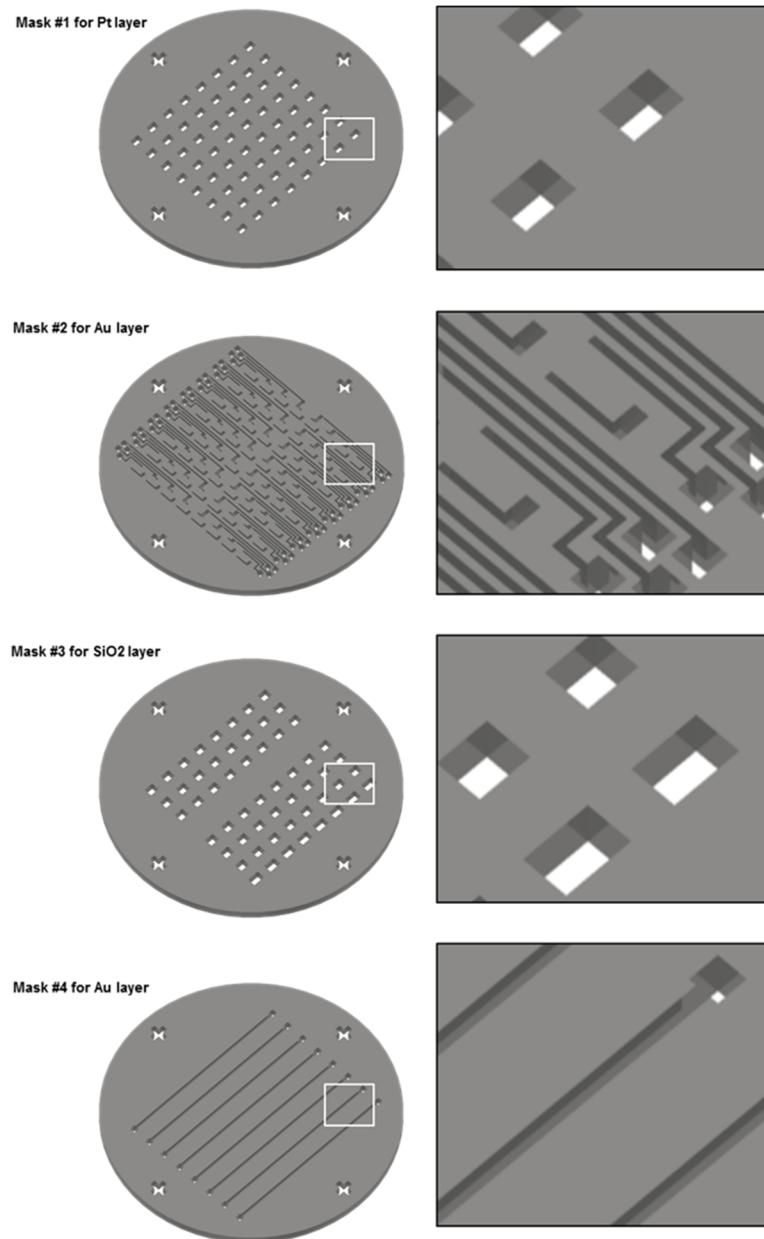


Figure 3-19. Shadow metal mask designs used for fabrication of multiplex sensor (S14).

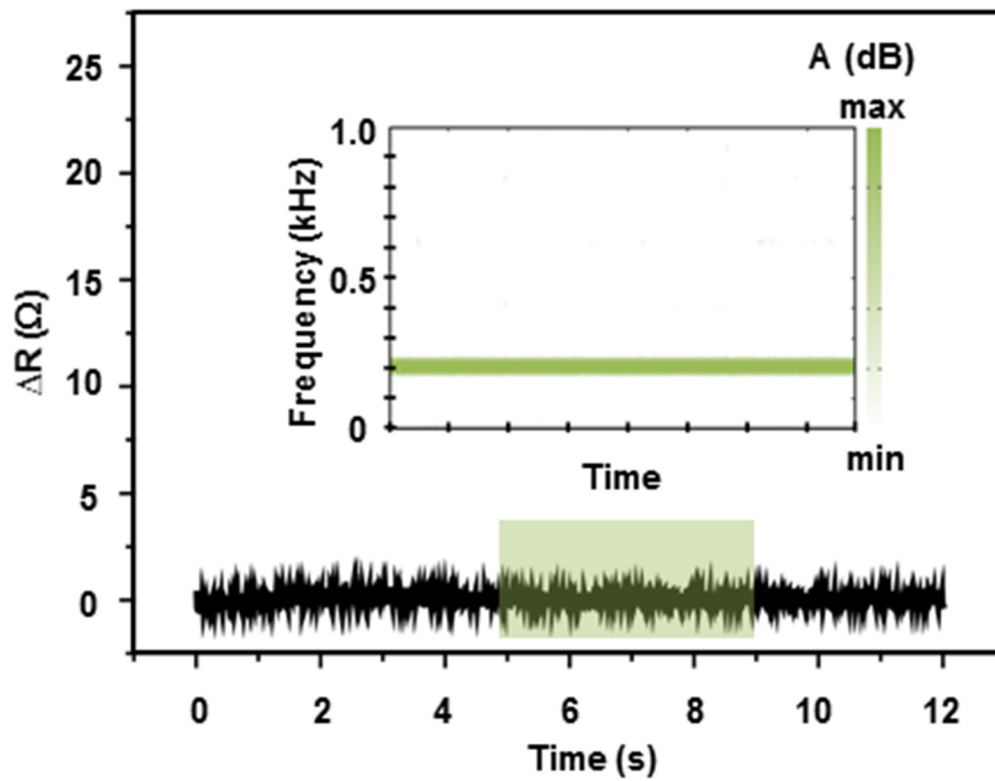


Figure 3-20. Resistance change with applied vibration and static pressure. Inset shows the frequency, 200 Hz, obtained by Fourier transform with vibration result.

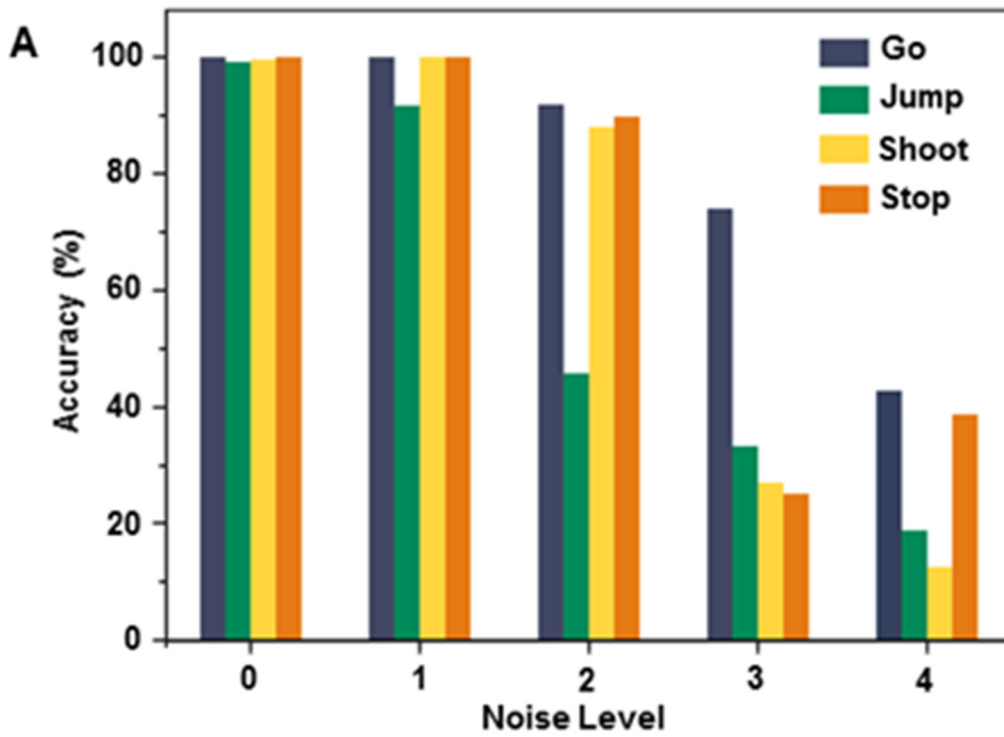


Figure 3-21. Speech recognition accuracy using microphone (with over 700 speeches; one person). (A) Accuracy as a function of noise level (~92 dB).

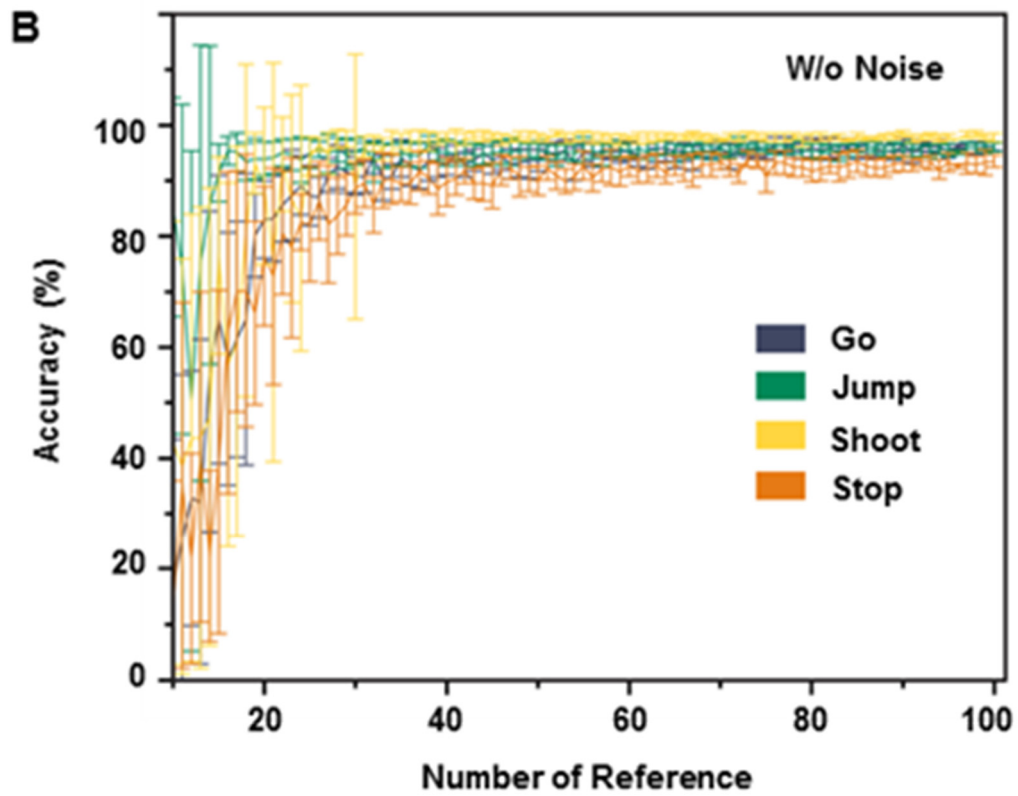


Figure 3-21. (B) Accuracy as a function of number of reference without noise condition.

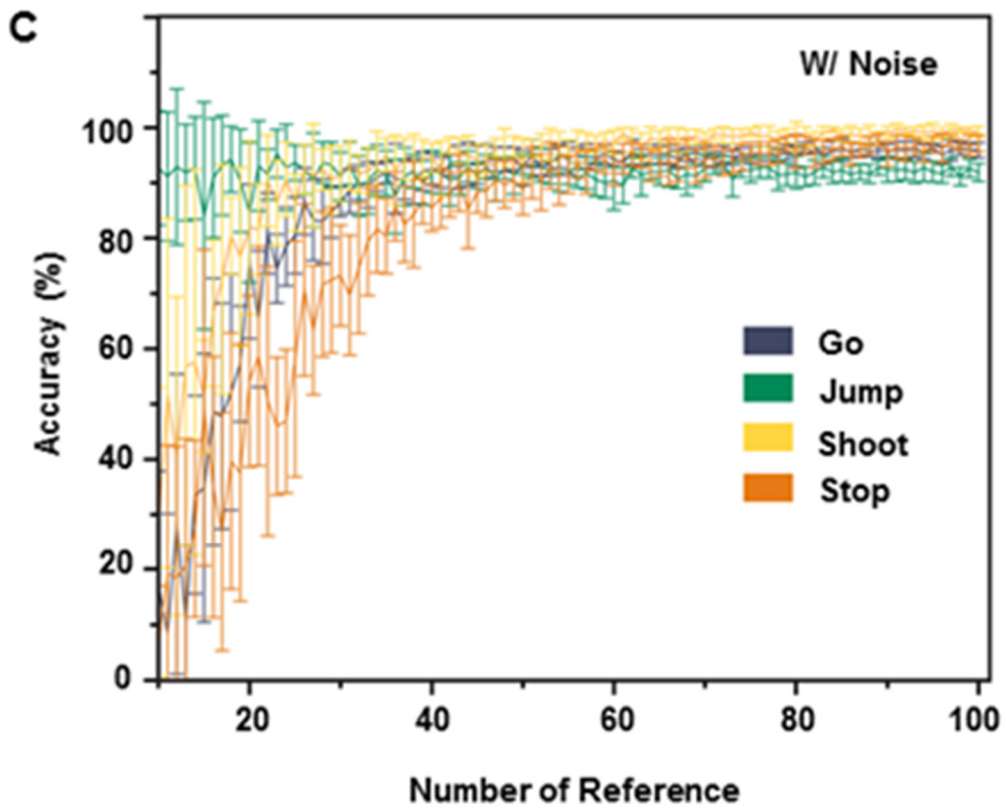


Figure 3-21. (C) Accuracy as a function of number of reference with noise condition (~92 dB).

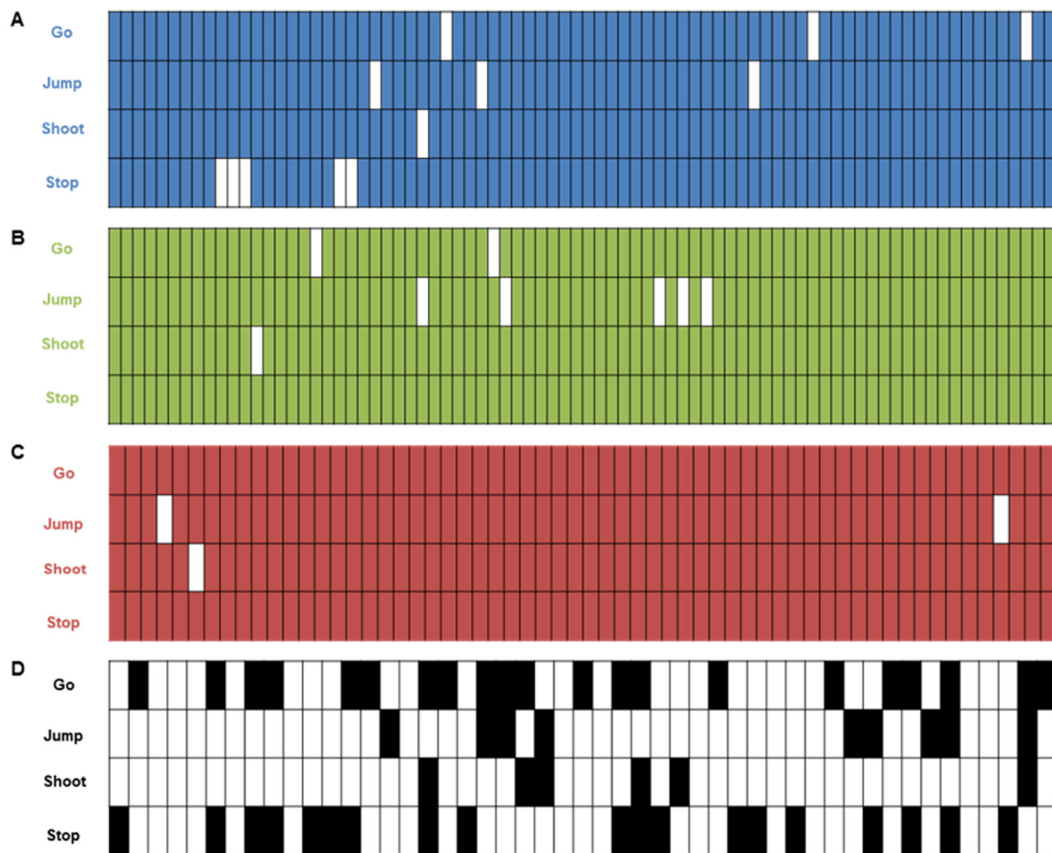


Figure 3-22. Speech recognition accuracy comparison with microphone and crack sensor (one person). (A) Accuracy using crack based sensor without noise. (B) Accuracy using microphone without noise. (C) Accuracy using crack based sensor with noise. (D) Accuracy using microphone with noise. White pixels show recognition failure case.

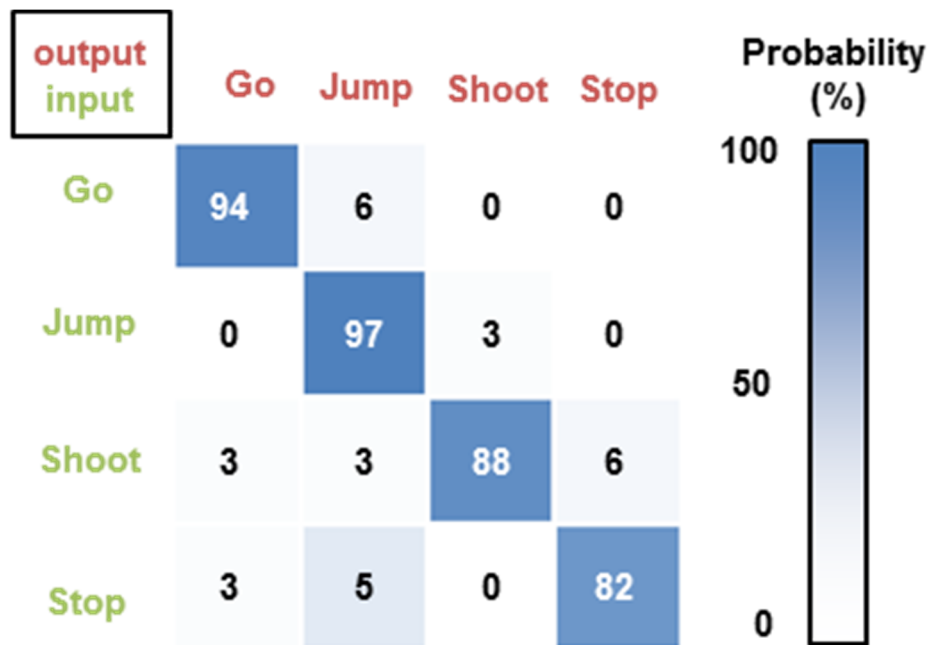


Figure 3-23. Speech recognition accuracies using crack based sensor (100 times test with 10 persons).

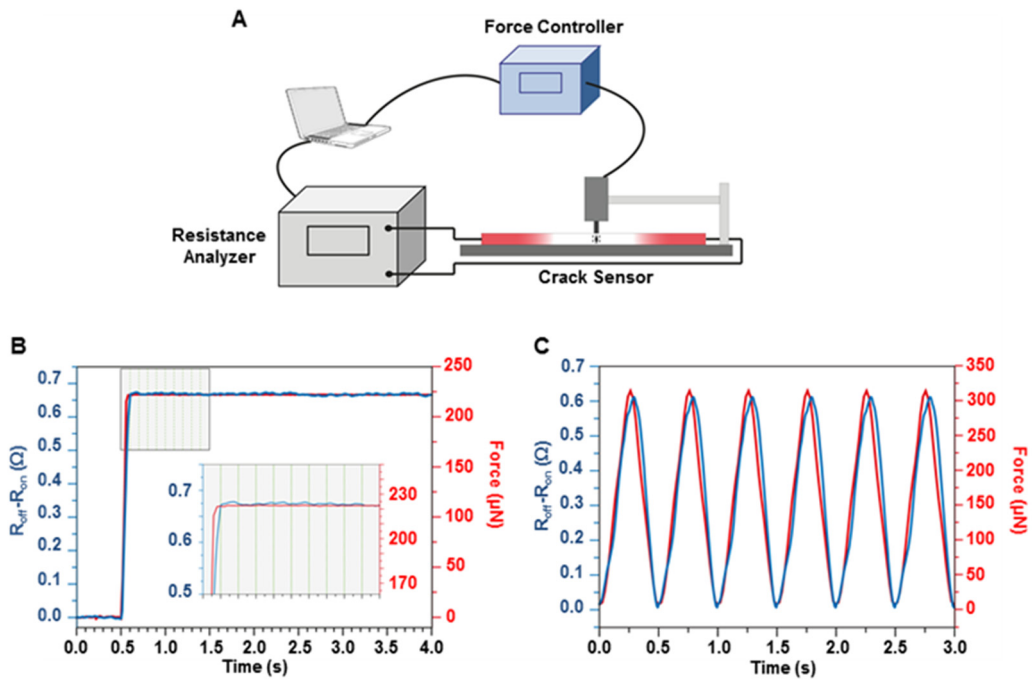


Figure 3-24. Pressure tests with force sensor and water droplet. (A) Scheme about force sensor experiment. **(B)** Resistance distribution of crack sensor in step functional pressure. We can know that the sensor response within 100 ms. **(C)** Resistance distribution of crack sensor in sinusoidal functional pressure.

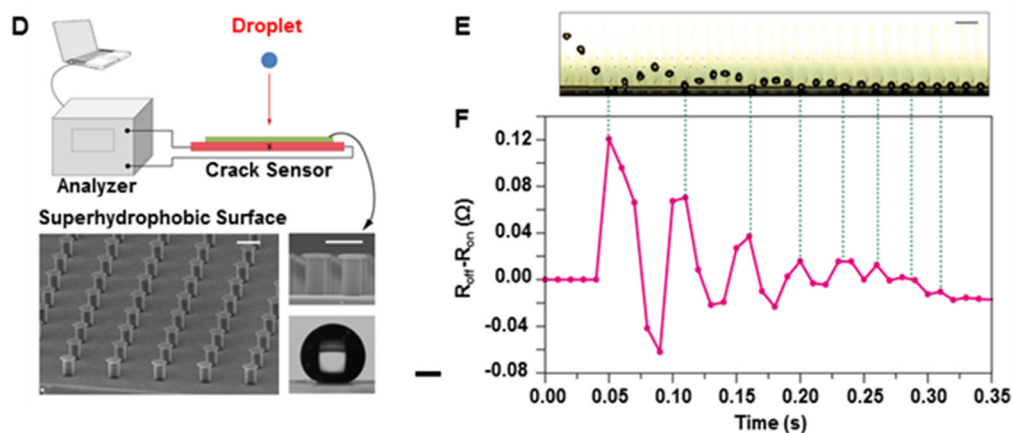


Figure 3-24. (D) Scheme about water droplet experiment. We used superhydrophobic surface (scale bar is 10 μm , contact angle is about 150 degree) and 5 μl droplet. ; Images reproduced with permission from ref. 69, © 2012 ACS. **(E)** The corresponding snapshots from a high-speed camera are shown. **(F)** The difference in the electrical resistance ($R_{off} - R_{on}$) for the duration of ~ 0.35 s. Each dotted line relates the collision of a droplet to the peak position.

Material (t = 20nm)	Gauge factor (2% strain)	Ultimate tensile strength (MPa)
Gold (Au)	9.47 (no crack)	120
Platinum (Pt)	2079.23	125-165

Table 3-1. Gauge factor comparison of sensors made of gold and platinum.

20nm gold film case does not show crack formation at 1 mm curvature bending due to ductility.

References

- [1] Aizenberg, J., Tkachenko, A., Weiner, S., Addadi, L. & Hendler, G. Calcitic microlenses as part of the photoreceptor system in brittlestars. *Nature* **412**, 819-822 (2001).
- [2] Lee, L. P. & Szema, R. Inspirations from biological optics for advanced photonic systems. *Science* **310**, 1148-1150 (2005).
- [3] Yang, S., Ullal, C. K., Thomas, E. L., Chen, G. & Aizenberg, J. Microlens arrays with integrated pores as a multipattern photomask. *Applied Physics Letters* **86**, 201121 (2005).
- [4] Yang, S. et al. Functional biomimetic microlens arrays with integrated pores. *Advanced Materials* **17**, 435-438 (2005).
- [5] Jeong, K.-H., Kim, J. & Lee, L. P. Biologically inspired artificial compound eyes. *Science* **312**, 557-561 (2006).
- [6] H. K. Wu, T. W. Odom, G. M. Whitesides, *J Am Chem Soc* **2002**, *124*, 7288.
- [7] E. K. Abbe, *Journal of the Royal Microscopical Society* **1883**, *3*, 790.
- [8] Smolyaninov, I. I., Hung, Y.-J. & Davis, C. C. Magnifying superlens in the visible frequency range. *Science* **315**, 1699-1701 (2007).
- [9] Liu, Z., Lee, H., Xiong, Y., Sun, C. & Zhang, X. Far-field optical hyperlens magnifying sub-diffraction-limited objects. *science* **315**, 1686-1686 (2007).

- [10] Fang, N., Lee, H., Sun, C. & Zhang, X. Sub-diffraction-limited optical imaging with a silver superlens. *Science* **308**, 534-537 (2005).
- [11] Rho, J. et al. Spherical hyperlens for two-dimensional sub-diffractive imaging at visible frequencies. *Nature communications* **1**, 143 (2010).
- [12] Hell, S. W. Far-field optical nanoscopy. *science* **316**, 1153-1158 (2007).
- [13] Huang, B., Babcock, H. & Zhuang, X. Breaking the diffraction barrier: super-resolution imaging of cells. *Cell* **143**, 1047-1058 (2010).
- [14] Lee, J. Y. et al. Near-field focusing and magnification through self-assembled nanoscale spherical lenses. *Nature* **460**, 498-501 (2009).
- [15] Mason, D. R., Jouravlev, M. V. & Kim, K. S. Enhanced resolution beyond the Abbe diffraction limit with wavelength-scale solid immersion lenses. *Optics letters* **35**, 2007-2009 (2010).
- [16] Verma, A. & Sharma, A. Enhanced Self-Organized Dewetting of Ultrathin Polymer Films Under Water-Organic Solutions: Fabrication of Sub-micrometer Spherical Lens Arrays. *Advanced Materials* **22**, 5306-5309 (2010).
- [17] Kim, M.-S., Scharf, T., Haq, M. T., Nakagawa, W. & Herzig, H. P. Subwavelength-size solid immersion lens. *Optics letters* **36**, 3930-3932 (2011).
- [18] Wang, Z. et al. Optical virtual imaging at 50 nm lateral resolution with a white-light nanoscope. *Nature communications* **2**, 218 (2011).
- [19] Tien, C.-H., Hung, C.-H. & Yu, T.-H. Microlens arrays by direct-writing inkjet print for LCD backlighting applications. *Display Technology, Journal of* **5**,

147-151 (2009).

[20] Kim, P., Kwak, R., Lee, S. H. & Suh, K. Y. Solvent-Assisted Decal Transfer Lithography by Oxygen-Plasma Bonding and Anisotropic Swelling. *Advanced Materials* **22**, 2426-2429 (2010).

[21] Kwak, R., Jeong, H. E. & Suh, K. Y. Fabrication of Monolithic Bridge Structures by Vacuum-Assisted Capillary-Force Lithography. *Small* **5**, 790-794 (2009).

[22] Jeong, H. E., Lee, J.-K., Kim, H. N., Moon, S. H. & Suh, K. Y. A nontransferring dry adhesive with hierarchical polymer nanohairs. *Proceedings of the National Academy of Sciences* **106**, 5639-5644 (2009).

[23] Kwak, M. K., Kim, T. i., Kim, P., Lee, H. H. & Suh, K. Y. Large-Area Dual-Scale Metal Transfer by Adhesive Force. *Small* **5**, 928-932 (2009).

[24] Jeong, H. E, Suh, K. Y. On the role of oxygen in fabricating microfluidic channels with ultraviolet curable materials. *Lab on a Chip* **8**, 1787-1792 (2008).

[25] Jeong, H. E., Kwak, R., Kim, J. K. & Suh, K. Y. Generation and Self-Replication of Monolithic, Dual-Scale Polymer Structures by Two-Step Capillary-Force Lithography. *Small* **4**, 1913-1918 (2008).

[26] Dussan, E. On the spreading of liquids on solid surfaces: static and dynamic contact lines. *Annual Review of Fluid Mechanics* **11**, 371-400 (1979).

[27] Orr, F., Scriven, L. & Rivas, A. P. Pendular rings between solids: meniscus properties and capillary force. *Journal of Fluid Mechanics* **67**, 723-742 (1975).

- [28] Choi, S.-J., Kim, H. N., Bae, W. G. & Suh, K.-Y. Modulus-and surface energy-tunable ultraviolet-curable polyurethane acrylate: properties and applications. *Journal of Materials Chemistry* **21**, 14325-14335 (2011).
- [29] Park, J. et al. Conformable Solid-Index Phase Masks Composed of High-Aspect-Ratio Micropillar Arrays and Their Application to 3D Nanopatterning. *Advanced Materials* **23**, 860-864 (2011).
- [30] Oh, J. R. et al. Wafer-scale colloidal lithography based on self-assembly of polystyrene nanospheres and atomic layer deposition. *Journal of Materials Chemistry* **20**, 5025-5029 (2010).
- [31] Li, H., Low, J., Brown, K. S. & Wu, N. Large-area well-ordered nanodot array pattern fabricated with self-assembled nanosphere template. *Sensors Journal, IEEE* **8**, 880-884 (2008).
- [32] Haynes, C. L. & Van Duyne, R. P. Nanosphere lithography: a versatile nanofabrication tool for studies of size-dependent nanoparticle optics. *The Journal of Physical Chemistry B* **105**, 5599-5611 (2001).
- [33] Fratzl, P. & Barth, F. G. Biomaterial systems for mechanosensing and actuation. *Nature* **462**, 442-448 (2009).
- [34] Song, Y. M. et al. Digital cameras with designs inspired by the arthropod eye. *Nature* **497**, 95-99 (2013).
- [35] Jeong, K.-H., Kim, J. & Lee, L. P. Biologically inspired artificial compound eyes. *Science* **312**, 557-561 (2006).

- [36] Zheng, Y. et al. Directional water collection on wetted spider silk. *Nature* **463**, 640-643 (2010).
- [37] Geim, A. et al. Microfabricated adhesive mimicking gecko foot-hair. *Nature materials* **2**, 461-463 (2003).
- [38] Pang, C. et al. Bioinspired Reversible Interlocker Using Regularly Arrayed High Aspect-Ratio Polymer Fibers. *Advanced Materials* **24**, 475-479 (2012).
- [39] Höbl, B., Böhm, H., Rammerstorfer, F., Müllan, R. & Barth, F. Studying the deformation of arachnid slit sensilla by a fracture mechanical approach. *Journal of biomechanics* **39**, 1761-1768 (2006).
- [40] Kim, D.-H. et al. Epidermal electronics. *Science* **333**, 838-843 (2011).
- [41] Takei, K. et al. Nanowire active-matrix circuitry for low-voltage macroscale artificial skin. *Nature materials* **9**, 821-826 (2010).
- [42] Kim, D.-H., Lu, N., Huang, Y. & Rogers, J. A. Materials for stretchable electronics in bioinspired and biointegrated devices. *MRS bulletin* **37**, 226-235 (2012).
- [43] Kaltenbrunner, M. et al. An ultra-lightweight design for imperceptible plastic electronics. *Nature* **499**, 458-463 (2013).
- [44] Schwartz, G. et al. Flexible polymer transistors with high pressure sensitivity for application in electronic skin and health monitoring. *Nature communications* **4**, 1859 (2013).
- [45] Someya, T. et al. A large-area, flexible pressure sensor matrix with organic

- field-effect transistors for artificial skin applications. *Proceedings of the National Academy of Sciences of the United States of America* **101**, 9966-9970 (2004).
- [46] Yamada, T. et al. A stretchable carbon nanotube strain sensor for human-motion detection. *Nature nanotechnology* **6**, 296-301 (2011).
- [47] Li, X. et al. Stretchable and highly sensitive graphene-on-polymer strain sensors. *Scientific reports* **2** (2012).
- [48] Mannsfeld, S. C. et al. Highly sensitive flexible pressure sensors with microstructured rubber dielectric layers. *Nature materials* **9**, 859-864 (2010).
- [49] Wang, Z. L. Self-Powered Nanosensors and Nanosystems. *Advanced Materials* **24**, 280-285 (2012).
- [50] Wu, W., Wen, X. & Wang, Z. L. Taxel-addressable matrix of vertical-nanowire piezotronic transistors for active and adaptive tactile imaging. *Science* **340**, 952-957, doi:10.1126/science.1234855 (2013).
- [51] Livne, A., Bouchbinder, E., Svetlizky, I. & Fineberg, J. The near-tip fields of fast cracks. *Science* **327**, 1359-1363 (2010).
- [52] Nam, K. H., Park, I. H. & Ko, S. H. Patterning by controlled cracking. *Nature* **485**, 221-224 (2012).
- [53] Kim, B. C. et al. Guided fracture of films on soft substrates to create micro/nano-feature arrays with controlled periodicity. *Scientific reports* **3** (2013).
- [54] Vandeparre, H., Liu, Q., Mineev, I. R., Suo, Z. & Lacour, S. P. Localization of Folds and Cracks in Thin Metal Films Coated on Flexible Elastomer Foams.

Advanced Materials **25**, 3117-3121 (2013).

[55] Choi, S.-J., Yoo, P. J., Baek, S. J., Kim, T. W. & Lee, H. H. An ultraviolet-curable mold for sub-100-nm lithography. *Journal of the American Chemical Society* **126**, 7744-7745 (2004).

[56] Yoo, P. J. et al. Unconventional patterning with a modulus-tunable mold: from imprinting to microcontact printing. *Chemistry of materials* **16**, 5000-5005 (2004).

[57] Thouless, M., Li, Z., Douville, N. & Takayama, S. Periodic cracking of films supported on compliant substrates. *Journal of the Mechanics and Physics of Solids* **59**, 1927-1937 (2011).

[58] Gell-Mann, M. & Low, F. Quantum electrodynamics at small distances. *Physical Review* **95**, 1300 (1954).

[59] Drury, W., Gokhale, A. M. & Antolovich, S. Effect of crack surface geometry on fatigue crack closure. *Metallurgical and Materials Transactions A* **26**, 2651-2663 (1995).

[60] Pollack, I. & Pickett, J. Cocktail party effect. *The Journal of the Acoustical Society of America* **29**, 1262-1262 (2005).

[61] Pang, C. et al. A flexible and highly sensitive strain-gauge sensor using reversible interlocking of nanofibres. *Nature materials* **11**, 795-801 (2012).

[62] Cao, J., Wang, Q. & Dai, H. Electromechanical properties of metallic, quasimetallic, and semiconducting carbon nanotubes under stretching. *Physical*

review letters **90**, 157601 (2003).

[63] Pham, G. T., Park, Y.-B., Liang, Z., Zhang, C. & Wang, B. Processing and modeling of conductive thermoplastic/carbon nanotube films for strain sensing. *Composites Part B: Engineering* **39**, 209-216 (2008).

[64] Zhou, J. *et al.* Flexible piezotronic strain sensor. *Nano letters* **8**, 3035-3040 (2008).

[65] Lee, Y. *et al.* Wafer-scale synthesis and transfer of graphene films. *Nano letters* **10**, 490-493 (2010).

[66] Xiao, X. *et al.* High-Strain Sensors Based on ZnO Nanowire/Polystyrene Hybridized Flexible Films. *Advanced Materials* **23**, 5440-5444 (2011).

[67] Chortos, A. *et al.* Highly Stretchable Transistors Using a Microcracked Organic Semiconductor. *Advanced Materials* (2014).

[68] Wang, Y. *et al.* Wearable and Highly Sensitive Graphene Strain Sensors for Human Motion Monitoring. *Advanced Functional Materials* (2014).

[69] Kang, S. M. *et al.* Robust superomniphobic surfaces with mushroom-like micropillar arrays. *Soft Matter* **8**, 8563 (2012).

국문초록

본 논문은 자연의 생명체에 존재하는 감각기관들을 관찰하고 이를 활용한 새로운 개념의 고감도 인지시스템을 제시한다. 즉 거미불가사리 표피에 있는 마이크로 돌기의 광집속(Light Focusing) 현상을 관찰하여 원리를 이해하고 나아가 이를 활용하여 기존의 광학현미경으로 관찰할 수 없었던 150 nm 구조물을 분해하는 초고감도 마이크로렌즈를 제작하였으며, 거미의 다리에 존재하는 진동 감각기관(Slit Organ)의 원리를 이해 및 모사하여 ~10 nm 수준의 진동을 인식하는 고감도 크랙센서를 구현하였다. 특히 크랙센서의 경우 2 % 이내의 인장에서 2000 이 넘는 Gauge Factor 를 보여주었는데, 이는 지금까지 보고된 어떤 GF 보다 높은 값이다. 나아가 이러한 결과를 통해 본 연구가 정밀 기계적인 응용과 생체 신호를 관찰하는 의공학 분야 및 음성을 인식하는 인공 피부 기술로서의 응용에 사용될 수 있음을 보여주었다.

주요어: 생체모사, 마이크로렌즈, 마이크로 컨택 프린팅, 디웨팅, 회절 한계, 슬릿기관, 진동인식, 스트레인 게이지, 나노크랙, 음성인식

학번: 2009-20647